Winter 2014

Analysis of heat transfer in spray cooling systems using numerical simulations

Masoumeh Jafari
University of Windsor

ANALYSIS OF HEAT TRANSFER IN SPRAY COOLING SYSTEMS USING NUMERICAL SIMULATIONS

by

Masoumeh Jafari

A Thesis

Submitted to the Faculty of Graduate Studies

through Mechanical, Automotive and Materials Engineering

in Partial Fulfillment of the Requirements for

the Degree of Master of Applied Science at the

University of Windsor

Windsor, Ontario, Canada

2013

ANALYSIS OF HEAT TRANSFER IN SPRAY COOLING STYSTEMS
USING NUMERICAL SIMULATION

by

Masoumeh Jafari

APPROVED BY:

_____

Dr. R. Carriveau
Department of Civil and Environmental Engineering

_____

Dr. D. Ting
Department of Mechanical, Automotive and Materials Engineering

_____

Dr. R. Barron, Co-Advisor
Department of Mathematics and Statistics, Department of Mechanical,
Automotive and Materials Engineering

_____

Dr. R. Balachandar, Co-Advisor
Department of Civil and Environmental Engineering, Department of Mechanical,
Automotive and Materials Engineering

_____

October 17th, 2013

Declaration of Co-Authorship

Co-Authorship Declaration

I hereby declare that this thesis incorporates the outcome of a joint research undertaken in collaboration under the co-supervision of Dr. Barron and Dr. Balachandar. The collaboration is covered in Chapter 2, 3, 4, 5, 6 and 7 of the thesis. In all cases, the key ideas, primary contributions, numerical simulation designs, data analysis and interpretation were performed by the author.

I am aware of the University of Windsor Senate Policy on Authorship and I certify that I have properly acknowledged the contribution of other researchers to my thesis and have obtained written permission from each of the co-authors to include the above materials in my thesis.

I certify that, with the above qualifications, this thesis, and the research to which it refers, is the product of my own work.

I declare that to the best of my knowledge, my thesis does not infringe upon anyone's copyright nor violate any proprietary rights and that any ideas, techniques, quotations, or any other material from the work of other people included in my thesis, published or otherwise, are fully acknowledged in accordance with the standard referencing practices. Furthermore, to the extent that I have included copyrighted material that surpasses the bounds of fair dealing within the meaning of the Canada Copyright Act, I certify that I have obtained a written permission from the copyright owners to include such material(s) in my thesis.

I declare that this is a true copy of my thesis, including any final revisions, as approved by my thesis committee and the Graduate Studies office, and that this thesis has not been submitted for a higher degree to any other University or Institution.

Abstract

The impingement of sprays onto dry and wet walls and the associated heat transfer occurs in many engineering applications. These applications include internal combustion engines, gas turbines, spray drying, spray coating and spray cooling. The fluid dynamics and heat transfer characteristics of liquid films created by spray impingement are very complex and determining the underlying physics requires fundamental studies.

In this study, an efficient and practical approach is devised for tackling many aspects of the spray cooling process. The computational fluid dynamics (CFD) methodology used here includes numerous droplets and it is designed to predict the spray-wall impact outcome based on reliable correlations. Even though it is not an exact representation of the interaction between the spray and the liquid layer due to computational considerations, it provides an acceptable picture of the transport phenomena. The STAR-CCM+ CFD code has been used to solve continuity, momentum, and energy equations coupled with a Lagrangian-Eulerian solver capable of simulating droplets as well as thin fluid film.

The model is validated against relevant experimental data available in the literature and good agreement is observed for heat transfer coefficient (HTC) values for cases involving spray impact and fluid film formation over a flat solid surface. The effect of mass flux and spray Reynolds number on the spray behaviour has been studied. The model is extended to predict the cooling performance of sealed cans containing hot liquids when the cans are cooled by the impingement of spray formed from a cold liquid. The CFD results are compared with field data obtained at Heinz Canada, Leamington, ON. The effect of the can rotational speed on the cool-down behaviour is investigated. The results show that there is an optimum rotational speed beyond which the heat transfer enhancement will not be as significant.

This research is the first study which solves the transport phenomena of fluid and heat outside, through and inside a sealed solid can containing a hot liquid while being cooled by the spray of a cold liquid.

Dedication

To my mother, my husband and my precious son, Parsa.

Acknowledgements

I would like to express my sincerest gratitude to my advisors, Dr. Barron and Dr. Balachandar, for their endless support and advice during the course of this research. Without their patience, understanding and help, I would not have been able to successfully complete this work.

I would like to thank my thesis committee members, Dr. D. Ting and Dr. R. Carriveau for their time and valuable input.

Financial support from the Natural Sciences and Engineering Research Council of Canada (NSERC) through the Engage program is gratefully acknowledged. Also, I would like to express my gratitude to Heinz Canada for giving access to their facilities in Leamington to collect data on their spray cooling operation.

I would also like to thank all my colleagues, Abbas Ghasemi, Mehrdad Shademan, Kohei Fukuda, Ghassan Nasif, Mohammadali Esmaeilzadeh and Han (John) Wang, for their time and knowledge that they shared during my study.

Table of Contents

List of Tables

List of Figures

List of Abbreviations, Symbols, Nomenclature

c_p	Specific Heat at Constant Pressure
$c_p{}^0$	Specific Heat at Constant Pressure and Temperature (293 K)
C_d	Drag Coefficient of the Droplet
ζ	Local Coordinate Normal to the Wall
d_0	Nozzle Orifice Diameter
d_p	Mass Median Droplet Diameter
D	Diameter of the Heated Target
ε	Dissipation Rate
δ	Film Thickness
E	Energy
f	Fluid Phase (subscript)
f_b	Body Force
g	Gravitational Acceleration/ Gas Phase (subscript)
G	Water Mass Flux
h	Enthalpy/Heat Transfer Coefficient
H^0	Formation Enthalpy of the Substance
H_T	Distance to the target
K	Turbulence Kinetic Energy/Specific Heat Ratio
La	Laplace Number
μ	Dynamic Viscosity
μm	Micron
Σ	Surface Tension
ν	Kinematic Viscosity
Nu	Nusselt Number
P	Pressure
∇p	Pressure Drop Across the Nozzle
Pr	Prandtl Number
q''	Heat Power Divided by Heat Surface Area
Q_t	Rate of Convective Heat Transfer

ρ	Density
r	Radius
Re	Reynolds Number
Re_p	Reynolds Number of Particle
sat	Saturation (subscript)
sub	Subcooling (subscript)
S_m	Momentum Source Corresponding to the Mass Source
S_h	Energy Sources
S_u	Energy Source/Sink Term per Unit Film Area
t	Time
t_1	Total Travel Time
T	Temperature
T_{bb}	Temperature Before Bath
T_{ab}	Temperature After Bath
T_1	Can Temperature
T_0	Can Temperature at the Entrance
T_w	Water Temperature
T_{inlet}	Fluid Temperature at the Entrance of the Nozzle
T_e	Environment Temperature
$T_{boiling}$	Boiling Temperature of the Working Fluid
τ	Shear Stress
U	Mean Velocity
U_d	Droplet Normal Component of Impinging Velocity
V_t	Tangential Component of the Droplet Velocity
V	Droplet Mean Velocity
ω	Specific Dissipation Rate/Angular Velocity
θ	Spray Cone Angle
We	Weber Number
Oh	Ohnesorge Number
CFD	Computational Fluid Dynamics
CHF	Critical Heat Flux

HTC	Heat Transfer Coefficient
I.L	Inner Left
I.R	Inner Right
O.L	Outer Left
O.R	Outer Right
NCL	Newton's Cooling Law
RANS	Reynolds Averaged Navier-Stokes
RPM	Revolutions Per Minute
SCZ	Slowest Cooling Zone
SHZ	Slowest Heating Zone
SMD (d_{32})	Sauter Mean Diameter
TAB	Taylor Analogy Breakup
URF	Under-relaxation Factor
USG	US Gallon

Chapter 1. Introduction

In this chapter, the process of spray cooling and its various applications are introduced. In addition, the motivation for the present research and its objectives are detailed. The thesis outline is presented as well.

1.1 Background

Spray impact on surfaces, involving multiphase flow of liquid droplets in a gas, occurs in many industrial applications. Examples include applications of spray cooling and fuel sprays in internal combustion engines and gas turbines and cooling of electronic devices (e.g. computer chips, sensors, lasers) used in space technology. Cooling applications are also found in the agricultural industry, food industry and medical applications.

In some of these applications, there is a need to dissipate heat fluxes well in excess of 1000 W/cm^2 (Yang et al., 1996). For these applications, the conventional air-cooled system is not sufficient for removing the heat fluxes, but the liquid-based approach (whether impinging jets or spray cooling) is more effective.

A comparison of the heat transfer coefficients for different cooling techniques is shown in Fig. 1.1. These techniques include free (natural) convection, forced convection, boiling convection, and jet and spray cooling using different working fluids. As can be seen in the figure, the highest values of heat transfer coefficients occur in spray cooling. The main advantage of spray cooling over jet cooling is that it more uniformly cools a large surface and removes larger amounts of heat, while in jet cooling the resulting surface temperature will be highly non-uniform (Mudawar, 2000).

Spray cooling occurs when liquid is forced through a small orifice, breaking or atomizing into many fine droplets that then impinge onto the heated surface as illustrated in Fig. 1.2. Figure 1.2(a) shows the evolving process of spray impingement on a surface. As seen, the primary phase of breakup happens at the tip of the nozzle. Essentially, the cavitation bubbles formed inside the nozzle cause primary breakup, which forces the liquid to disintegrate into ligaments and large droplets. The droplets travel away from the nozzle and, as a result of a velocity difference at the shear layer of the liquid jet, the gas-

liquid interface becomes unstable to the point that the viscous forces do not dampen the instabilities. Eventually, the instability dominates the surface tension forces and disintegrates the liquid. This is referred to as secondary breakup. Beyond this point, that is, the region where disintegration happens, the spray can be said to be fully developed. Until that stage, the spray is called a free spray. If the spray strikes a plate, the process is called an impinging spray. At the fully developed spray stage, smaller droplets with higher total surface contact area can be achieved. As a result, higher heat transfer rates can be achieved. For this reason, the distance of the nozzle to the impingement point plays an important role in the heat transfer process.

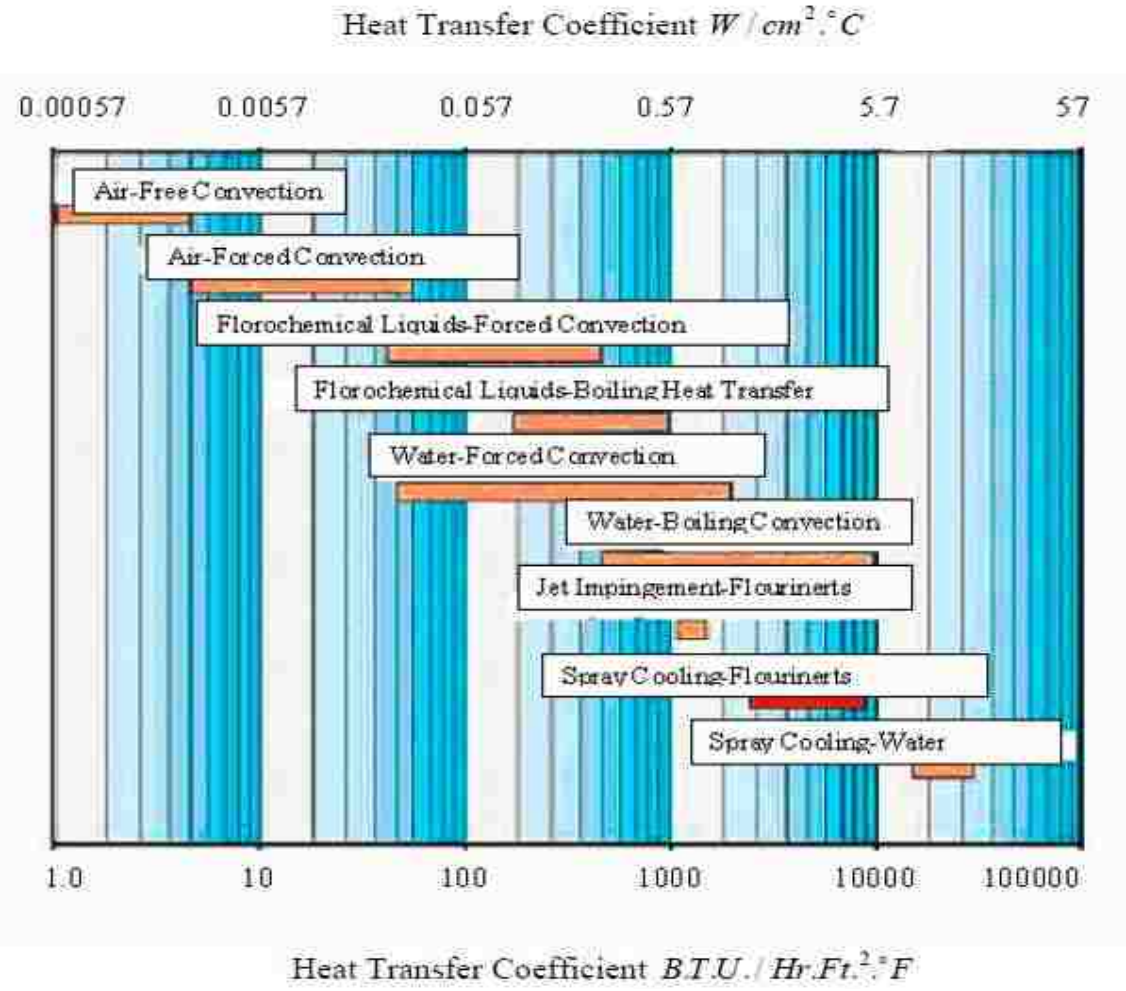

Figure 1.1 Comparison of heat transfer coefficient for different cooling techniques (Website: www.pitek.us)

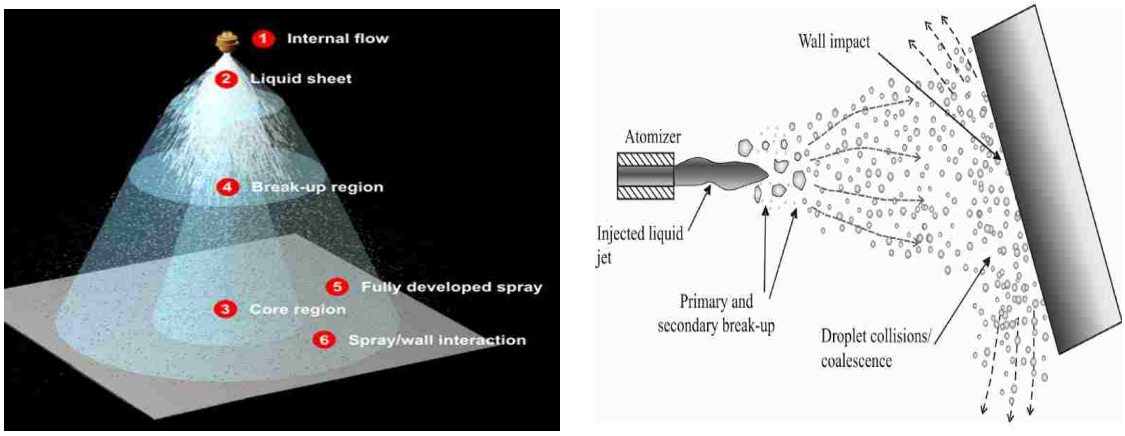

(a) (b)

Figure 1.2 Stages of spray formation and impact (a) spray formation and (b) spray breakup, impingement and film formation (Tropea, 2007)

By introducing a plate at the end of the spray, different mechanisms of droplet impingement come into play, characterized by the impact energy. The possible outcomes of impingement are stick, spread, splash and rebound. The droplets that stick or spread, if the spreading area is small enough, form a continuous thin liquid film that has an important role in the cooling process. Figure 1.3 shows spray impingement on a heated surface accompanied with a fluid film.

Figure 1.3 Spray impinging on a heated surface (Website: www.valcompanies.com)

In the case of flows involving phase change, the fluid evaporates near the plate. With time, bubbles nucleate on the surface inside the thin liquid film. Droplets

continually impinge and interact with the growing bubbles within the film, resulting in high heat removal through conduction, convection, and phase change. The spray cooling process is shown schematically in Fig. 1.4. Sprays can be either dilute or dense. A spray is considered dilute if the mass flux is less than 2 kg/m^{2}s and dense if it has a mass flux of at least 8 kg/m^{2}s (Deb and Yao, 1989).

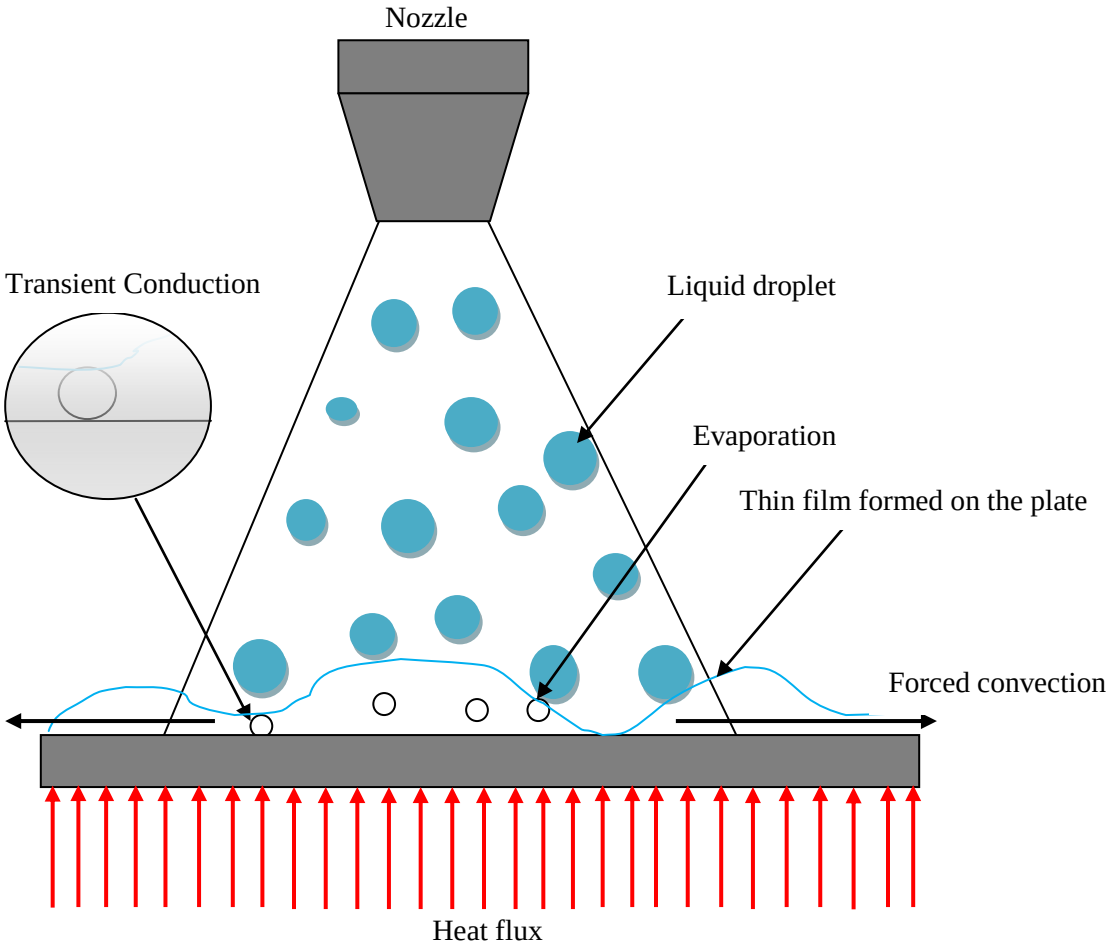

Figure 1.4 Schematic illustration of spray cooling

One important aspect of spray cooling is the basic boiling phenomenon that occurs. Boiling is an efficient means of heat transport in which liquid is vaporized when the temperature of the liquid exceeds the saturation vapour pressure. Typically, in boiling, a large amount of heat can be removed at relatively low temperature difference. It is useful to first consider the boiling processes in the absence of an incoming spray. Boiling

heat transfer is usually characterized by a boiling curve (Fig. 1.5) with various boiling regimes.

In the first regime (indicated as I in Fig. 1.5), free convection occurs when no vapour is generated because of low wall superheat and insufficient nucleation sites. This single-phase regime can be treated analytically or with correlations such as that provided by Churchill and Chu (1975). This regime ends when bubble generation begins. Even this simple regime is quite complicated in spray cooling because of the motion of the liquid film and the mixing caused by impinging droplets. The nucleate boiling regime (Regions II - III) begins once bubbles are generated, and is characterized by two sub-regimes. The first is the isolated bubble regime (Region II), where bubbles form at their own nucleation sites and depart without interacting with each other. Following this sub-regime, at higher wall superheat, the departure frequency is so large that the bubbles immediately begin to coalesce both horizontally and vertically. This is the regime of slugs and columns (Region III).

Following the nucleate boiling regime, the boiling curve continues to rise to the local maximum heat flux referred to as the critical heat flux (CHF) or the burnout heat flux. This occurs due to vapour generation that is so large that liquid can no longer come into contact with the heated surface. With insufficient supply of liquid to cool the surface, heat must be transported through the vapour. Heat transfer through the vapour is less efficient (due to its lower thermal conductivity) and results in a decrease in the heat flux. CHF represents a thermal design limit for many applications since at this point the heat flux declines as the temperature rises, which ultimately causes surface overheat. The transition boiling regime (Region IV) follows the CHF point and is characterized by increasing wall temperature and decreasing heat flux. This is due to an increase in the dry area covering the heated surface. This regime is of little practical interest because it is unstable and quickly results in the film-boiling regime (Region V). However, it is important to note that any constant heat flux experiment that drives the heater to CHF will inevitably drive the heater into the transition-boiling regime. The higher temperatures and exposure to dissolved gases may cause changes to the surface microstructure. Eventually, a local minimum in the boiling curve is reached, denoted as the Leidenfrost point. At this point, the surface enters the film-boiling regime (Region V).

In the film-boiling regime, heat must be conducted across a continuous vapour film before it can be transferred to the liquid. This inefficient process can result in large heat fluxes, but the temperatures required are very high. The film-boiling regime is therefore not practical as a mean of cooling many devices.

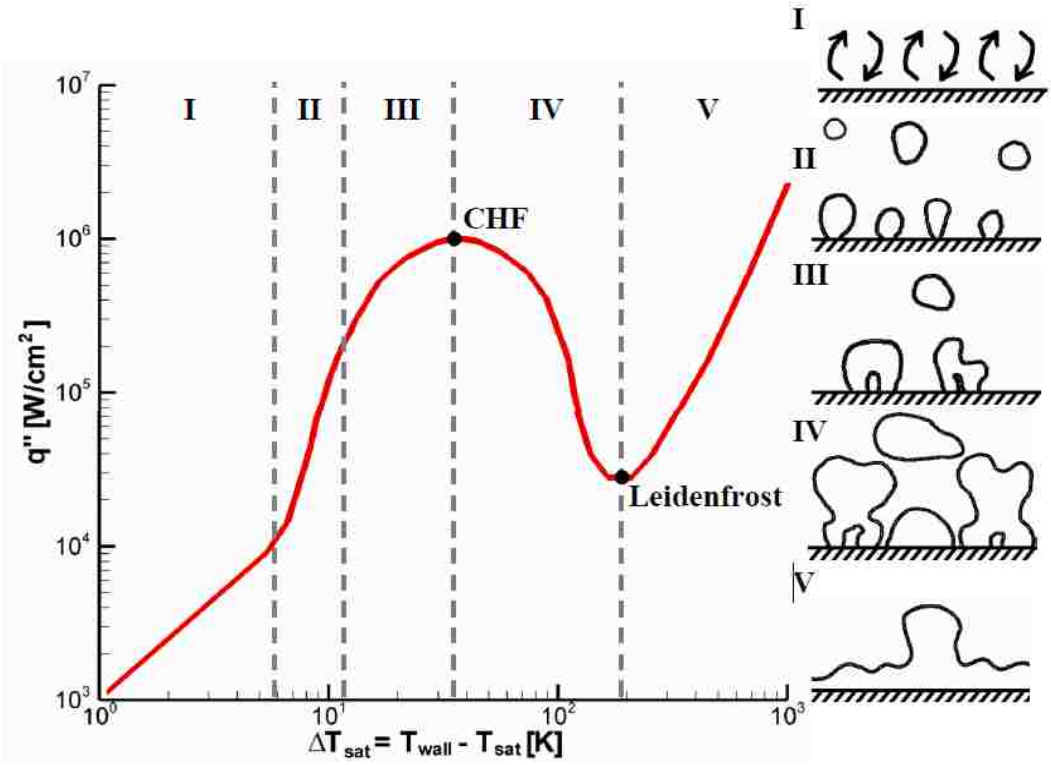

Figure 1.5 Typical boiling curve and associated boiling regimes (Coursey, 2007)

1.2 Motivation

Details of spray cooling heat transfer are not fully understood by the research community. The main reason is the complex physics involving simultaneous interaction of spray droplets, thin film surface and spray droplet evaporation, nucleation, convection and condensation. Another complication in understanding spray cooling heat transfer mechanisms is the small scales at which it occurs. This is the main reason that there are not many reliable models, which are able to describe the outcome of spray impact and the corresponding heat transfer with good accuracy for different regimes. Direct experimentation has been limited in its ability to provide much more than empirical heat transfer correlations. Hence, it is important to understand the accompanying physical phenomena and to identify the main influencing parameters.

Computational modeling can be an effective analysis and design tool for spray equipment manufacturers and process engineers. Depending on the application, modeling can also be very complex, requiring accurate physical models to represent the effects of droplet momentum, layer thickness, gravity, surface tension, surface characteristics and phase change. These phenomena must often be simulated over a very diverse range of length scales, for hundreds or thousands of droplets, with diameters that are typically orders of magnitude smaller than the object being impacted.

Computational Fluid Dynamics (CFD) results for a wide variety of droplet sizes, velocities, heat fluxes and wall surface temperatures can be used to provide physical insight into the best ways to achieve maximum spray cooling heat transfer coefficients and avoid surface flooding as well as dry spotting. The task of combining the individual complex phenomena mentioned above together to successfully model the spray cooling is a great challenge.

Recently, a few numerical studies on spray cooling have been conducted. Selvam et al. (2005) presented the computer modeling of multiphase flow using the level set method to identify the interface between vapour and liquid. Guechi et al. (2012) developed a numerical model to predict the heat transfer with phase change between a hot plate surface and a two-phase impinging spray using FLUENT software. Even though these models are not an exact representation of the interaction between the spray and the liquid layer, they provide a good indication of how to improve the heat transfer.

Based on this discussion, it can be concluded that numerical modeling could be a valuable tool through which several aspects can be studied quickly and at minimum cost. The results also can help shed some light on the current understanding of spray cooling. Continuous advances in computing power and CFD methodologies have led to a widespread use of numerical methods to directly simulate interface transport mechanisms of multiphase flows. However, despite some progress, a full simulation investigating detailed behaviour of every small droplet remains computationally very expensive.

1.3 Objectives

This research was primarily initiated to analyze the spray cooling process of tomato juice cans at the Heinz Canada plant in Leamington, Ontario. The overall

objective of this work is to develop a better understanding of the hydrodynamics and heat transfer associated with the spray impact onto a heated surface.

In order to simulate the spray impinging on heated flat and curved surfaces, a model is developed herein and simulated using the commercial software STAR-CCM+. Based on previous research, as the droplets impinge onto a heated surface, a thin fluid layer is formed, and the best way to investigate spray cooling is to specify the existence of this thin layer and study the interaction between the layer and the impinging spray droplets.

To gain confidence in the numerical results, it is important to validate the results with proper experimental results. To test the model validity for the non-boiling spray cooling regime, some case studies were selected and the simulations results were compared with available experimental data of Karwa et al. (2007). Since the main concern in any cooling method is the heat flux and surface temperature, the heat transfer coefficient and temperature distribution on the hot surface are used for validation.

Once the CFD model was validated, a model of the Heinz spray cooling process is developed in STAR-CCM+. Based on the field measurements done at the plant, a simple model is presented to predict the temperature of tomato juice at the end of the production line.

The specific goals of this work include:

- To develop a CFD model that can be used to study the heat transfer mechanism during spray cooling in the non-boiling regime.
- To validate the computed results with the experimental data (Karwa et al., 2007) in order to gain confidence on the fidelity of the numerical approach.
- To investigate the sensitivity of the CFD model for different mesh sizes and turbulence models.
- To apply the CFD model to the real-world application of spray cooling of tomato juice cans.

1.4 Thesis Outline

The thesis is laid out in seven chapters. Chapter 2 reviews spray cooling in non-boiling and boiling regimes. Also, different heat transfer mechanisms during the cooling

process and the way these mechanisms affect the heat transfer are discussed. Chapter 3 provides an overview of the governing equations for multiphase flows. A detailed description of the CFD code (STAR-CCM+) is provided and its strengths and limitations for studying spray cooling problems are highlighted. Chapter 4 provides details about the validation of the CFD simulation by making use of the relevant experimental data available in the literature. Chapter 5 involves field measurements of the cooling behaviour of hot surfaces and containers in an industrial setting. Chapter 6 covers simulation of a simplified model of the flow field at Heinz to estimate the average heat transfer coefficient and to investigate the effects of different can rotational speeds on the heat transfer characteristics. Chapter 7 presents the conclusions and provides recommendations for future work.

Chapter 2. Literature Review

In this chapter, a review of the most relevant previous studies in the field of spray cooling is presented. Overall, there are a number of major spray parameters such as spray mass flux, spray volume flux, droplet number, droplet velocity and cone angle, which have the most significant effect on the cooling performance. In most cases, a liquid film is created as a result of droplet impingement. The liquid film behaviour is also an important factor in cooling efficiency. The spray cooling performance is usually gauged by the non-dimensional Nusselt (Nu) number which is directly proportional to the heat transfer coefficient.

An ideal cooling system should provide high heat removal rates uniformly over a large surface area with a high critical heat flux (CHF). Critical heat flux describes the thermal limit of a phenomenon where a phase change occurs during heating which suddenly decreases the efficiency of heat transfer, thus causing localized overheating of the heating surface.

Toda (1972) found that subcooling had a minor effect on single-phase and nucleate boiling heat transfer and did not have a dominant effect on CHF. Monde (1980) observed that the nucleate boiling gradient in spray cooling is nearly half that of pool boiling. Toda (1972) and Monde (1980) both found that the cooling performance is enhanced in every cooling regime by increasing the spray volume flux. Mudawar and Valentine (1989) also showed that the volume flux had the most dominant effect on the CHF compared to other hydrodynamic properties of the spray.

Pautsch (2004) suggested that spray cooling has often been misrepresented by the term “spray evaporative cooling”. He points out that some spray cooling system designs rely very little on the evaporation of fluid to remove heat. Furthermore, he suggested that spray cooling designs with higher values of CHF have less evaporation than the designs with lower values of CHF. As a result, in order to show the difference between them, he proposed a new name if there is phase change, namely “spray cooling with phase change”.

A set of experiments were performed by Estes and Mudawar (1996) to understand the nucleate boiling and CHF for full cone sprays. They investigated the effect of spray nozzle, volume flux, subcooling and properties of the working fluids. They reported that

the CHF increases with increasing flow rate and increasing subcooling. They also found that the CHF is greater for smaller drops due to greater surface tension. For full cone sprays, Sauter mean diameter (d_{32}), the diameter of a drop that has the same volume per unit surface area as the entire spray, is dependent upon orifice diameter and the Weber and Reynolds numbers based on the orifice flow conditions before the liquid breakup.

The effect of spray characteristics for non-critical heat flux in subcooled water spray cooling was experimentally investigated by Chen et al. (2002). They defined three independent spray parameters: mean droplet velocity (V), mean spray droplet flux (N), and Sauter mean droplet diameter (d_{32}). The effect of these parameters on the CHF was determined, utilizing extensive experimental data. They suggested that CHF varies proportional to $V^{1/4}$ and $N^{1/6}$, and is relatively independent of d_{32}. The CHF and the heat transfer coefficient showed an increase when V increased. Increasing N also resulted in an increase in CHF and heat transfer coefficient when other parameters were kept in narrow ranges. According to their results, in order to increase the CHF for a given N, a dilute spray with large droplet velocity is more effective than a dense spray with low velocities.

Toda (1972), using water as a working fluid, found that the CHF increased approximately 50% as the mean droplet diameter increased from 88 to 120 microns. However, Pais et al. (1992) and Estes and Mudawar (1996) suggested that CHF could be increased by decreasing the droplet diameter. Sehmbey et al. (1995) argued that the smaller droplets can produce the same values of CHF at smaller flow rates as larger droplets at larger flow rates. According to research by Bostanci (2010), increasing flow rate beyond a certain level (the medium flow rate in their case) has a minimal effect on CHF.

Peterson (1970) found that heat fluxes as high as 15 MW/m^2 could be removed from a spray cooled surface. At surface temperature of 130^o C, heat fluxes in the order of 2.2 MW/m^2 were removed by sprays used by Bonacina et al. (1979). Bonacina et al. (1975) found that if the wall is fully wetted, the heat transfer rate is higher. According to Kim et al. (1997), larger film thickness produces lower heat transfer.

Yang et al. (1996) observed that heat fluxes as high as 10 MW/m^2 can be obtained in gas-assisted spray cooling with water in the presence of phase change from a low wall

superheat. Using FC-72 as the working fluid, a 1 MW/m^2 heat flux was obtained by Estes and Mudawar (1996).

Pautsch and Shedd (2006) found that the most important and the least studied parameter of spray cooling is the thickness of the liquid film layer which exists on the heated surface. The values of the film thickness were 0 to 75 microns. They also explained that once the droplets hit the surface, they are swept off by the flow of subsequent droplets, the surface is continually wetted, and a thin liquid film forms. They explained different mechanisms of heat transfer in this film: conduction, convection, bubble nucleation, and gas bubbles entrained by impacting droplets. They concluded that each of these components contributes to the total heat removal process although their exact portion of contribution is unknown and almost all affect the film thickness.

Pais et al. (1992) point out that the heat is conducted from the surface through the thin liquid layer. They reported that a thinner film results in higher heat transfer due to the increased thermal gradient across the layer.

Toda (1972) explained how the liquid droplets impinge on the heated surface and spread over the surface, becoming fully wetted by a thin liquid film. Under the effect of the momentum added by the incoming droplets, the film moves and evolves along the surface. The new droplets arrive at a temperature lower than the film temperature near the surface. The droplets which impact the surface of the film become part of the film and their kinetic energy maintains the flow.

Spray cooling heat transfer was surveyed by Kim (2007). He reported that the heat removal mechanisms are poorly understood due to their dependency on many parameters including the unique droplet size distribution, droplet number density and droplet velocity. Other parameters which also affect spray cooling heat transfer are impact angle, surface roughness, gas content, film thickness, number of nozzles and the heated surface orientation. Kim (2007) reported that after the droplets impact a heated surface, they spread on the surface and evaporate or form a thin liquid film, removing large amounts of energy. He also argued that significant disturbances occur due to the droplet impact onto the liquid film, increasing the amount of heat transferred. He found that the heat transfer increases with increasing flow rate which is due to the increase of the liquid velocity over the surface and the thinner thermal boundary layer. It was also

reported that the mechanisms by which the critical heat flux is triggered during spray cooling are currently unknown. Two mechanisms were suggested; homogenous nucleation within the film and lift-off of the thin liquid layer due to nucleation within the film. Kim (2007) mentioned that spray cooling is not expected to be affected by the heater orientation relative to the gravity vector or by low gravity conditions, due to the large momentum of the spray. Kim (2007) suggested that it is not possible to model the spray cooling process from first principles due to the enormous number of droplets. Kim concluded that further advances in understanding spray cooling will require the development and application of new experimental techniques.

The thickness of liquid films resulting from both a low flow rate single nozzle and a high flow rate four-nozzle array was measured by Pautsch and Shedd (2006) using FC-72 as the working fluid. A non-intrusive optical technique based on total internal reflection was used. The reflected light rings that formed on the test surface were photographed. An automated program measured and recorded the radii, from which the thickness of the film was calculated using the fundamental equations of geometric optics. It was found that for the four-nozzle array, the regions which had previously shown the poorest heat transfer performance were the ones which had the thickest film. While using the single-nozzle spray, it was found that adding a heat load did not affect the film thickness.

Spray cooling is also a well known technique in steel plate manufacturing. It is used to control the steel temperature and hence the steel properties. Arrays of nozzles are placed in multiple stages in the plate direction for spray cooling. Kim et al. (1997) pointed out that it was not clear if the spray cooling heat transfer was enhanced by the liquid film flow on the steel plates. They concluded that in the presence of the liquid film, the heat transfer rate directly below the spray centre decreased and this deficit increases as the film becomes thicker. They also found that spray cooling heat transfer which includes the film flow is significantly enhanced as the spray droplet flux increases.

Lin and Ponnappan (2003) studied the performance of arrays of sprays. Similar trends for the heat transfer performance were observed when compared with the single nozzle spray data from Estes and Mudawar (1995). According to Lin et al. (2004), as the number of spray nozzles increases, the CHF can increase up to 30%. According to

Pautsch and Shedd (2005), the two-phase heat transfer mechanisms contribute the equivalent of 25-30% of the total single-nozzle spray cooling heat rate and only 10-20% of the total four-nozzle spray cooling heat rate. Furthermore, their models indicate that in spray cooling systems where a thin liquid film exists on the heated surface, heat removal is dominated by the single-phase energy transfer rather than the phase-change mechanisms.

A number of attempts have been made to measure the thickness of the film in spray cooling. Kalantari and Tropea (2007) extensively studied the influence of film thickness on spray/wall interaction and developed a new theoretical model for prediction of the average film thickness as a function of mean Reynolds number, flux density of the impacting droplets and the average drop diameter.

The other heat transfer mechanism, according to Rini et al. (2002) and Yang et al. (1996), is secondary nucleation. They postulated that the impacting droplets entrain vapour and/or gas into the liquid film, creating nucleation sites and causing boiling within the film.

Oliphant et al. (1998) experimentally investigated both spray and jet impingement cooling in the non-boiling regime. According to their experiment, the heat transfer is dependent on the spray mass flux and droplet velocity. In their experiment, the impingement surface temperature was maintained below the saturation temperature of the spray liquid. The combination of unsteady thermal boundary layer and evaporative cooling resulted in an increase of the average heat transfer for sprays compared with jets in the non-boiling regime. They concluded that spray cooling can provide the same amount of heat transfer as jet cooling at a significantly lower liquid mass flux. Moreover, spray cooling shows promise because of the large surface area that is formed when a liquid is atomized into droplets by the spray nozzle.

The cooling characteristics of sprays impacting a square heated test surface were investigated by Rybicki and Mudawar (2006). PF-5052 was used as the working fluid, with three upward-oriented full-cone spray nozzles subjected to variations in both flow rate and subcooling. They concluded that the volume flux and Sauter mean diameter are the key hydrodynamic parameters that influence spray cooling performance. They also

found that nozzle orientation has no effect on spray cooling performance, provided the cooling system does not promote liquid build-up on the hot surface.

Karwa et al. (2007) reported that for spray cooling at lower wall superheats, the heat transfer occurs primarily through single-phase convection. The rate of evaporation is higher when the surface temperature is closer to the saturation temperature of the fluid and a thin film is formed. As mentioned by Lin and Ponnappan (2003), at higher mass flux, a thicker liquid film causes reduction in the evaporation from the free surface of the liquid. Karwa et al. (2007) also concluded that the droplet impingement onto the liquid film not only provides enhanced mixing, but also increases the turbulence in the film and thus enhances the heat transfer rate.

The heat transfer distribution for an isothermal surface under a single nozzle spray was experimentally investigated by Zhao et al. (2010). Water was used as the working fluid and the spacing between the nozzle and the heater surface was varied from 3 to 7 mm. In their experiments, the temperature was kept below 100°C. For a given nozzle-to-surface distance, the highest temperature occurred directly under the spray nozzle. They also reported that with the increase of the radius away from the centre of the surface, the temperature decreases at first, and then increases beyond a certain position. Hsieh et al. (2004) suggested that this phenomenon is due to the non-uniform droplet distribution and film parameters.

According to experiments of Zhao et al. (2010), as the spray height increases from a certain point, the average surface temperature increases. This, according to them, might suggest that the spray's heat transfer performance has an optimized value within a certain range of the spray height.

A set of experiments using water and R-134a as working fluids were performed by Hsieh et al. (2004). The effects of the working fluid, degree of subcooling and spray mass fluxes on the cooling characteristics of the hot surface were investigated. They found that the spray mass flux has a strong effect on the spray cooling performance. Also, the effect of the degree of subcooling was insignificant, especially for R-134a because of the low degree of subcooling used. They also reported that water shows a much higher cooling performance than R-134a.

Roisman and Tropea (2004) presented hydrodynamic models for two extreme cases: (a) a very sparse spray impact characterized by small relative crown presence, such that the effect of their interaction can be neglected; and (b) a very dense spray impact. The velocities of the secondary droplets produced by the crown splash in a sparse spray were described theoretically. The fluctuations in the motion of the liquid film created by a dense impacting spray were analyzed statistically. This motion yields the formation of finger-like jets. The characteristic size and velocity of the film fluctuations were estimated. They validated two theoretical models against the experimental data and obtained good agreement. This agreement indicates that the inertial effect associated with drop impacts is the dominant factor in formation of the uprising sheets, whereas the capillary forces influence the velocity of the secondary droplets. They showed that the velocity of secondary droplets produced by very dense diesel spray impact are of the same order as the value of estimated characteristic velocity of film fluctuations and the average diameter of these secondary droplets is of order of the characteristic length of fluctuations.

Most of the relevant numerical studies have focused on impingement of a single droplet on a dry surface or a pre-existing liquid film in order to study the spray cooling behaviour. As described by Moreira et al. (2010), the flow systems involving spray nozzles are usually very complex and the underlying physics requires fundamental studies, which are often performed on simplified flow geometries. Specifically, a lot of effort has been put into trying to represent and predict the outcome of the spray impingement by impinging individual droplets in both experimental and numerical studies. This is often done despite the known fact that a spray does not behave as a summation of individual droplets. In order to be able to include numerous droplets in the computational model, specific models which can provide an acceptable prediction of the fate of each impinging droplet is required.

Bai et al. (2002) developed a modified spray impingement model for the simulation of gasoline spray wall impact. The model was assessed by simulating experiments on oblique spray impingement in a wind tunnel. Both the impingement model and the spray initialization procedure were implemented into the STAR-CD® commercial computational code, which uses a finite volume methodology and the k-ε

model for the gas phase and a stochastic Lagrangian method for the spray. The results of the comparisons between the calculated results and the measurement data show generally reasonable agreement.

In a recent survey done by Selvam et al. (2005) regarding the computational modeling of spray cooling, it was concluded that the best way to model the spray cooling is to have the spray impinge on a pre-existing thin liquid film on a hot surface. They stated that this will help understand and improve the performance of spray cooling. As a result of their survey, they found that theoretical understanding of spray cooling is still in its infancy and a focused effort to develop a comprehensive numerical model is of prime importance to this field. They also reported that the liquid film thickness cannot exceed 2 mm. For spray cooling designed for high heat flux, the liquid film thickness on the hot surface is less than 200 microns. It was reported that numerical modeling of nucleate boiling of thin films has never been attempted before. According to Selvam et al. (2005), the spray cooling heat transfer mechanism is quite complicated and there are a lot of contradictions in the experimental results.

Numerical modeling of multiphase flow in spray cooling using the level set method was studied by Selvam et al. (2005). The model considers the effect of surface tension between liquid and vapour, gravity, phase change and viscosity. The computer model was used to study the spray cooling phenomenon in the micro-environment of about 40 μm thickness liquid layers with vapour bubbles growing due to nucleation and droplet impact. The effect of velocity and density ratio variations on heat transfer was investigated systematically for the case of droplet impact on vapour bubble. A new non-dimensional equation was suggested for the solution of the Navier-Stokes equation which is more stable than the one reported in Selvam et al. (2009). In their model, the fluid properties including density, viscosity and thermal conductivity are constant in each phase and the flow is assumed to be incompressible.

Stanton and Rutland (1996, 1998) developed a wall film model that solves the mass continuity and momentum conservation equations for a two-dimensional film on three-dimensional surfaces. This model includes the effects of spray drop impingement and splashing processes, which are addressed by a set of correlations for the distribution

of mass and momentum as a function of key dimensionless parameters for the incident droplet.

Cole et al. (2005) presented a Lagrangian spray wall impingement model integrated into the Eulerian free surface (Volume of Fluid) module of the multi-physics computational code, CFD-ACE^{+}. The coupling of the two modules enables the modeling of spray impingement and splashing, including the effects of a fluid film on the wall. They demonstrated a functional link between Lagrangian spray transport and Eulerian simulation of fluid dynamics with two distinct fluid phases. The former uses the free surface volume of fluid model to resolve individual droplets with diameters in range of 50-100 microns and evaluate mass, momentum, and energy transfer from the spray droplets to the film as a function of droplet Weber number and dimensionless layer thickness.

Kuhlman et al. (2011) described a Monte-Carlo simulation of spray cooling that is based upon a time scale analysis of the various relevant physical processes. They presented the results from an initial implementation of the model. The model correctly predicts trends of increasing areas where boiling occurs and where dry out occurs as the heater power increases at a constant spray volume flow rate, and trends of dry out of the heater surface being initiated near the outer edge of the circular heater for FC-72 and HFE-7000. Due to the much larger values of surface tension, specific heat, and latent heat of water, none of the droplet impact craters are predicted to dry out for water at the assumed values of the spray flow rate and heater power. However, their model does not accurately predict the relationship between heater surface temperature and the heat transfer rate.

The rewetting of a hot surface by droplet impingement was studied by Youssef (2007), who found from axisymmetric numerical simulations that the cooling is improved by increasing the spray velocity. The reason for this was due to the increase in the momentum of the liquid layer imparted by the spray. It is obvious that the momentum increases by increasing the spray velocity. It was also found from the numerical simulations that the cooling improves by decreasing the distance between the nozzle and the heater surface. This was also due to the increase in the momentum. The third

parameter which was studied was the spray mass flow rate. It was found that increasing the spray mass flow rate improves the heat transfer by increasing the momentum.

Meredith et al. (2011) developed a model for simulating water film transport over solid-fuel surfaces. The model was coupled to a gas-phase solver, solid boundary condition, and spray transport model implemented in OpenFOAM®, a computational toolkit along with essential source terms for inter-phase transport. They showed that the initial validation of the model is in good agreement with the Nusselt solution for continuous film flows over inclined surfaces. They also compared the film model with available experimental measurements for film thickness, velocity and mass flow rate.

Based on the literature survey, it is clear that there are a number of major spray parameters such as spray mass flux, spray height, droplet velocity and liquid film thickness which have the most significant effect on the cooling performance. Spray cooling is a very complex phenomenon involving several parameters and this makes it difficult to draw specific conclusions based on the correlations in the literature if they are obtained for systems of totally different parameters.

In some cases, there is no consensus on the effect of a specific parameter. For example, by increasing the spray height, heat transfer rate might increase or decrease. One could conclude that there is an optimized spray height which could boost the rate of heat transfer. Increasing the mass flux brings more momentum, more agitation to the liquid film and a thinner thermal boundary layer which eventually enhances the heat transfer rate. Depending on thickness, the liquid film could have a negative or positive impact on the heat transfer rate.

In order to gain deeper insight into the physics of spray cooling, more detailed numerical simulations are required. The numerical method should be capable of simulating full spray, including all the droplets as well as the resulting liquid film. In the next chapters of this thesis, such a numerical methodology will be explained in details and its results will be presented.

Chapter 3. Numerical Modeling

In this chapter, details of the numerical method and the computational tool used for the study of spray impingement and film formation are provided. Where necessary, the reasons for making specific assumption(s) in regards to the flow conditions or selecting a certain computational technique will be provided.

3.1 CFD Code Used in this Study

This section provides a brief description of the commercial CFD code selected for this research work and the limitations of the code for simulating two-phase conditions, as well as its limitation on connecting the Lagrangian phase to the Eulerian phase.

3.1.1 STAR-CCM+

STAR-CCM+ is the commercial CFD software employed in this research to perform spray impingement and cooling simulations. It is developed and licensed by CD-adapco to carry out three-dimensional modeling of fluid flow and heat transfer in complex geometries (STAR-CCM+, 2012). Although the code supports multiphase fluid simulations, it is most extensively used for single phase simulations. The code is built on client-server architecture and has parallel processing capabilities to optimize the computational time. The main feature of STAR-CCM+ compared to other solvers such as FLUENT and CFX is its integrated environment that allows one to perform multi-dimensional CAD modeling, state-of-the-art meshing (for example tetrahedral, polyhedral, hexahedral), model solving and post processing, all within the same software.

STAR-CCM+ supports unstructured meshing and incorporates two types of flow and energy modeling approaches, namely i) segregated approach, and ii) coupled approach. Segregated approach uses the SIMPLE (Semi-Implicit Pressure Linked Equation) algorithm to solve the conservation equations, whereas the coupled approach uses a time marching methodology (STAR-CCM+, 2012). A variety of turbulence models are supported including several variants of $k-\varepsilon$ (standard, realizable, RNG), $k-\omega$ (standard, SST) and Reynolds Stress Model (linear, quadratic). The solver permits

control over parameters such as solver iterations, tolerance values and relaxation factors to manage the progress of convergence.

STAR-CCM+ also supports user-defined field functions to implement methods that are not directly supported by the software. Field functions are single-line, C-syntax type statements that allow the manipulation of variables and other field functions to construct complex logical statements.

3.2 Introduction

Studying the spray interaction with the liquid film layer requires solving the flow and heat transfer equations for spray droplets, liquid film and the surrounding gas. Currently there are two approaches for the numerical calculation of multiphase flows: the Euler-Lagrange approach and the Euler-Euler approach. In the Euler-Euler approach, the different phases are treated mathematically as interpenetrating continua by introducing the concept of phase volume fraction. Conservation equations for each phase are derived to obtain a set of equations, which have similar structure for all phases. These equations are closed by providing constitutive relations that are generally obtained from empirical information. The Euler-Euler approach uses the notion of interfacial area concentration which is defined as the area of interfaces between two phases per unit mixture volume. This approach allows for heat and mass transfer between phases but does not seek to determine the properties of each particle present in the flow. Rather, it calculates local properties of the multiphase flow.

In the Euler-Lagrange approach (Discrete Phase Model), the fluid phase is treated as a continuum by solving the time-averaged Navier-Stokes equations, while the dispersed phase is solved by tracking a large number of particles, bubbles, or droplets through the calculated flow field. The dispersed phase can exchange momentum, mass, and energy with the fluid phase. In this approach, the particle or droplet trajectories are computed individually at specified intervals during the fluid phase calculation. The different modeling approaches have been compared by Guéchi et al. (2011). In particular, they showed that results strongly depend on the model of turbulence used and on the size of the droplets forming the spray. The computational model takes into account the gas flow, Lagrangian particle tracking of droplets in the gas, liquid-film formation due to

impingement of droplets on the solid surface, resulting liquid film transportation and heat and possible disintegration of film into drops.

The code enables one to model the spray particles individually or in representative parcels using a Lagrangian reference frame, and account for the fluid layer using an Eulerian framework. In this approach, the mass, momentum, and energy of a spray parcel that enters a liquid region (numerical control volume) may be transferred to the liquid in that control volume. The mass, momentum, and energy are subsequently tracked on a control volume basis in the Eulerian framework. Whether the spray parcel is absorbed in the liquid-filled cell depends on parameters such as the cell Weber number and the droplet velocity. If a spray parcel penetrates all the way to a solid wall, its mass, momentum and energy interaction are modeled based on correlations of Bai et al. (2002). At low Weber numbers, the droplet will stick to the wall and contribute to any liquid film. At the other extreme, i.e. for higher Weber numbers, the droplet will splash and eject secondary droplets that may have significantly more mass than the original droplet. In the current model implementation, only a single secondary parcel is generated in response to an incident parcel hitting a wall under splashing conditions. Results of a sample simulation using the coupled Lagrangian- Eulerian approach are shown in Fig. 3.1, where part (a) shows the droplets of different sizes (coloured by different colors) at the moment of impact with the solid surface. In Fig. 3.1(b), the solid surface is coloured by contours of the liquid film thickness which, is non-zero (wetted) in the non-blue areas as the liquid film starts to trickle down the solid cylinder's side faces.

The main topics covered in this chapter include: the governing equations for Computational Fluid Dynamics (CFD) modeling, description of the CFD code employed in this research to perform spray cooling simulations, and its limitations for tackling the problem at hand.

3.3 Droplet Interaction with the Wall

A key issue in properly assessing the performance of the impingement model in spray calculations is to ensure that pre-impingement conditions of each incoming droplet are estimated with reasonable accuracy. It is thus necessary to determine the appropriate initial conditions in the near-nozzle region of the spray. In general, the impingement

regimes are determined by the parameters describing the pre-impingement droplets, the wall surface conditions and the surrounding gas characteristics in a near-wall region. Of particular interest in identifying impingement regimes is the wall temperature, as stated by Bai and Gosman (1995).

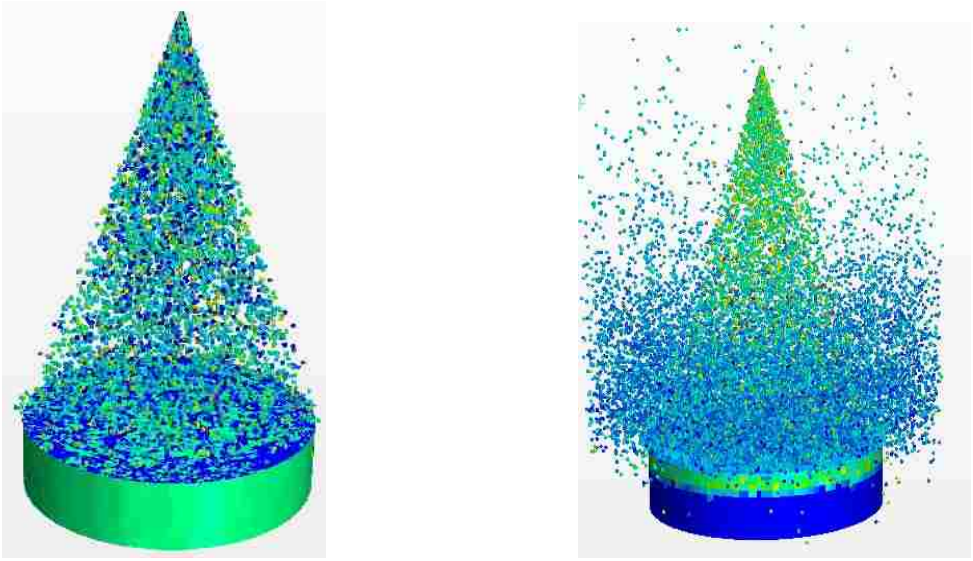

(a) (b)

Figure 3.1 Three-dimensional simulation of spray-liquid film interaction (a) Model domain and Lagrangian spray parcel distribution at the impact with the wall (b) Impacted, splashed, stuck and rebounded Lagrangian spray parcels and the evolving liquid film contours after 10 milliseconds.

The Bai-Gosman wall impingement model is a wall impingement feature formulated within the framework of the Lagrangian approach, based on the experimental results and mass, momentum and energy conservation constraints. To reflect the stochastic nature of the impingement process, a procedure is adopted to determine how and when droplets break up or stick to the wall. This model is used with impermeable boundaries (wall, contact and baffle) as well as with fluid film. This allows secondary droplets resulting from a primary droplet splash to have a distribution of sizes and velocities. For fluid film boundaries, momentum and kinetic energy lost by the droplets are gained by the film.

In this study, the regimes modeled for spray/wall interaction are stick, rebound, spread and splash for wall temperature below the liquid boiling temperature. The outcomes of impingement depend on the incoming droplet conditions, i.e. droplet velocity, size and temperature, incidence angle, wall temperature, surface roughness, wall

film thickness, and fluid properties such as viscosity and surface tension. The following are the possible outcomes of droplets impacting the wall:

Adhesion (or Stick): The impinging droplet adheres to the wall in a nearly spherical form. This regime occurs when the impingement energy is extremely low. A droplet is assumed to coalesce completely with local film. The transition criterion for this regime is We < 20.

Rebound: The impinging droplet bounces back from the wall after impact. In this regime, the rebound droplet velocity magnitude and direction need to be determined.

Spread: The droplet impacts on a wetted wall and spreads out and forms a wall film.

Splash: After the collision of a droplet on a wall, the droplet transforms as a crown shape, then a part of the droplet further breaks up and is ejected as small droplets, while the rest is adhered to the wall. In this regime, many quantities need to be calculated in order to describe the splashing process. These quantities include the proportion of incident droplet mass deposited as part of the liquid film and the sizes, velocities and splashing angles of secondary droplets are based on their experimental. They can be represented by the following two non-dimensional characteristic numbers:

i) Droplet Weber number

The Weber number represents the ratio of droplet kinetic energy to surface tension, defined as:

$$We = \frac{\rho D_d U_d^2}{\sigma} \tag{3.1}$$

where U_d is the droplet normal component of impinging velocity, D_d is the droplet diameter and σ is the surface tension coefficient for the liquid.

ii) Droplet Laplace number

The Laplace number measures the relative importance of surface tension and viscous force acting on the drop. It is defined as:

$$La = \frac{\rho \sigma D_d}{\mu_f^{\,2}} \tag{3.2}$$

where μ_f is the droplet dynamic viscosity.

Due to the limitations of current understanding of the mechanisms involved in the thin liquid sheet breakup mechanism of injectors, no reliable atomization model is yet available for them and it is outside the scope of this study to attempt development of such a model.

Droplet aerodynamic breakup and collision/coalescence are accounted for in the Bai-Gosman wall impingement model which was considered for the impingement spray. It is either assumed that the droplets in the spray have the same size as the Sauter mean diameter, or they have a non-uniform size distribution as suggested by Rosin and Rammler (1933) with the *SMD* as the mean of the distribution. The Rosin-Rammler distribution was developed to describe the volume distribution of particles as a function of their diameter, $F_V(D_p)$. In STAR-CCM+, it is extended to be a generic size distribution, with the cumulative distribution function

$$F(D) = 1 - e^{-(\frac{D}{\chi})^q} \tag{3.3}$$

in which the exponent q is a user-defined parameter, which is set to 1.5 by default and the reference size χ is defined as

$$\chi = \frac{D_d}{(3\ln 10)^{1/q}} \tag{3.4}$$

This form identifies the Rosin-Rammler distribution as a Weibull distribution. As noted above, the Rosin-Rammler distribution may be a cumulative mass, volume or number distribution, depending on the injector's flow rate specification. A good option for determining the droplet diameter is to use the deterministic diameter, namely the average of size distribution, given by

$$D = \chi \Gamma\left(1 + \frac{1}{q}\right) \tag{3.5}$$

where Γ represents the Gamma function.

During the spray penetration, there is a drag force exerted on the droplets from the surrounding gases, which tends to decrease the relative velocity between the drop and the gas flow. From Newton's Second Law, the deceleration of the droplet is calculated using the following equation:

$$\frac{du_f}{dt} = \frac{\frac{1}{2}\rho_g \left| u_g - u_f \right| \left(u_g - u_f \right) * C_d \frac{\pi d^2}{4}}{m_f} \tag{3.6}$$

where ρ_g is density of the gas, u_g is velocity of the gas u_f is velocity of the droplet, C_d is drag coefficient of the droplet, d is the droplet diameter, m_f is droplet mass. In the above equations, subscripts g and f refer to gas and liquid, respectively. The droplet mass is calculated by:

$$m_f = \frac{4}{3}\rho_f \pi d^3 \tag{3.7}$$

The Liu dynamic drag coefficient is intended to account for the dependence of the drag of a liquid droplet on its distortion under the action of aerodynamic forces. As a basis, it uses the following expression for the drag coefficient of an undistorted sphere. The drag coefficient is given by the following equation:

$$C_{d,sphere} = \begin{cases} \frac{24}{\mathrm{Re}_p}(1 + \frac{1}{6}\mathrm{Re}_p^{\frac{2}{3}}) & \mathrm{Re} \le 1000 \\ 0.424 & \mathrm{Re} > 1000 \end{cases} \tag{3.8}$$

If the wall temperature increases to the so-called Leidenfrost temperature, which is higher than the boiling temperature, the existent liquid on the wall evaporates immediately and, under the thermal radiation and conduction across the thin layer, the incoming droplets start evaporating before they reach the wall. As the result, there is a vapor film between the incoming droplets and the hot surface, and the wall surface will be dry. The impingement regimes can be summarized in Fig. 3.2.

3.4 Governing Equations

The governing equations for CFD modeling are nonlinear partial differential equations (PDE), which constitute the equations for conservation of mass, momentum

and energy. In the spray cooling process liquid droplets, known as the dispersed phase, interact with a gaseous or liquid continuous phase. In STAR-CCM+, the Lagrangian multiphase tracking approach is designed for this purpose. This model permits solving an arbitrary number of dispersed phases, each modeled in a Lagrangian framework, in which particle-like elements known as parcels are followed through the continuum. The flow of material particles is governed by the momentum conservation equation. An energy conservation equation may also be solved, including convective heat transfer.

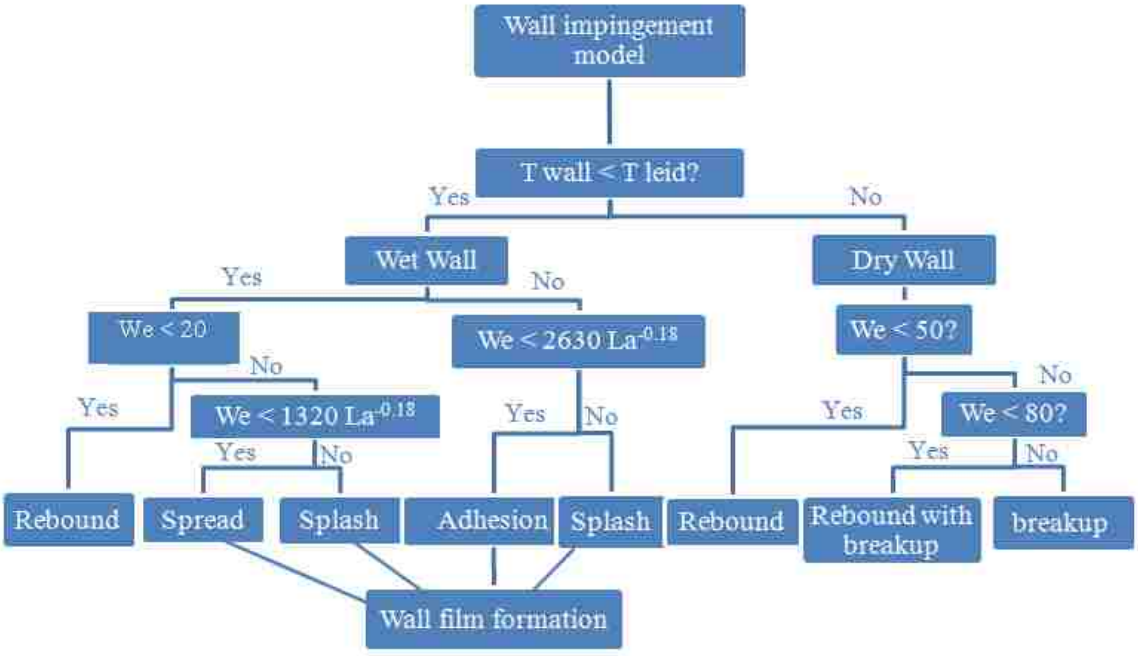

Figure 3.2 Spray-wall impingement regimes based on Bai-Gosman model, Bai et al. (2002)

Specific models for liquid droplets in a gaseous medium include a mass conservation equation to account for the change in droplet mass due to evaporation or condensation and models for secondary breakup. The interaction between particles and boundaries is defined by boundary conditions. Particle behaviour at impermeable boundaries, in particular, requires modeling depending on the active models.

In general, the state of the dispersed phases will be influenced by that of the continuous phase. Two-way coupling may also be applicable, in which the state of the continuous phase depends on the dispersed phases, through inter-phase mass, momentum and energy transfer effects.

Parcels introduced into a turbulent carrier flow will each have their own random path due to interaction with the fluctuating turbulent velocity field. A turbulent dispersion model is provided to account for this phenomenon.

A few other relevant equations are also required to appropriately describe the fluid flow and heat transfer that includes, among others, the turbulence models and near-wall treatment. Brief descriptions of the three-dimensional modeling equations derived by considering a finite control volume element are provided in the following sections. Many of these equations can be found in the STAR-CCM+ User's Manual (STAR-CCM+, 2012).

3.4.1 Conservation of Mass

The time rate of change of mass in a control volume is balanced by the net mass flow into the control volume and the generation of the mass within the control volume. In the limit, as the control volume shrinks to a point, one obtains

$$\frac{\partial \rho}{\partial t} + \frac{\partial (\rho u_j)}{\partial x_j} = 0 \tag{3.9}$$

This is the expression of conservation of mass for a compressible fluid. The first term represents the rate of change of density with time. The second term represents the gradient of mass change along the three spatial coordinate directions. This equation is also the differential form of the continuity equation. In this study, fluid is considered to be incompressible (i.e., fluid density is constant). For incompressible fluids with no source, equation (3.9) simplifies to:

$$\frac{\partial u_j}{\partial x_j} = 0 \tag{3.10}$$

In these equations, ρ is fluid density, t is time, x_j are spatial coordinates i.e., x, y, z coordinates, u_j are the fluid velocity components along the spatial coordinate directions.

3.4.2 Momentum Balance for a Material Particle

There are different forces acting on the particles identified separately as surface forces and body forces. Forces that act on the surface of the particles can be presented as the drag force and pressure force. The only body force in our case is gravity.

The momentum transfer to the particle from the continuous phase is due to forces that act on the surface of the particle. If the two-way coupling model is active, this is accumulated over all the parcels and applied in the continuous phase momentum equation. The pressure force comes from the gradient of the static pressure in the continuous phase. The drag force is a result of the different velocity between the air and the particles.

3.4.2.1 Conservation of Momentum

The three-dimensional conservation of momentum equations in the spatial directions is given in equation (3.11). The equations are derived by setting the rate of change of the momentum in a particular component direction equal to the net force acting on the element in that direction (due to the surface stress) plus the gravitational and external forces.

$$\frac{\partial(\rho u_i)}{\partial t}+\frac{\partial(\rho u_i u_j)}{\partial x_j}=-\frac{\partial p}{\partial x_j}+\frac{\partial \tau_{ij}}{\partial x_j}+\rho g_i+F_i \tag{3.11}$$

where p is pressure, τ_{ij} is shear stress, and g_i is gravitational acceleration and F_i represents the external body force. τ_{ij} is expressed as

$$\tau_{ij}=-\frac{2}{3}\mu\frac{\partial u_i}{\partial x_i}\delta_{ij}+\mu\left(\frac{\partial u_i}{\partial x_j}+\frac{\partial u_j}{\partial x_i}\right) \tag{3.12}$$

where δ_{ij} is Kronecker delta function.

The mass and momentum conservation equations, which form the Navier-Stokes equations, are solved simultaneously to describe fluid flow. The most accurate numerical method to solve for turbulent flows is to directly solve the Navier-Stokes equations using the Direct Numerical Solution (DNS) method without any turbulence model. However, tDNS is extremely difficult to implement and often is too time consuming and not suitable for practical applications. Also, the DNS approach, at its current stage of

development, is applicable only to flows at low Reynolds number with simple flow geometries.

As an alternative, time-averaged equations such as the Reynolds-Averaged Navier-Stokes equations (RANS) are used in practical CFD applications when modeling turbulent flows. The main assumption in this approach is to decompose the transient velocity into a mean and turbulent fluctuating part and solve the resulting simplified equations. As a result of this decomposition, a new set of unknowns, called Reynolds stresses, arise in the model, which are related to turbulent viscosity. The decomposition of velocity is

$$u_i = U_i + u_i' \tag{3.13}$$

where U_i is the mean velocity and u_i' is the turbulent fluctuating velocity.

The resulting simplified RANS equations for an incompressible flow under steady state conditions are

$$\rho U_k \frac{\partial U_i}{\partial x_k} = -\frac{\partial p}{\partial x_i} + \mu \frac{\partial^2 U_i}{\partial x_j \partial x_j} + \frac{\partial R_{ij}}{\partial x_j} \tag{3.14}$$

$$R_{ij} = -\rho u_i' u_j' = -\rho \frac{2}{3} k \delta_{ij} + \mu_t \left(\frac{\partial u_i'}{\partial x_j} + \frac{\partial u_j'}{\partial x_i} \right) \tag{3.15}$$

where μ_t is the turbulent viscosity and R_{ij} is Reynolds shear stress.

Turbulence models are used to evaluate turbulent viscosity. There are several methods available for turbulence modeling, such as (i) linear eddy-viscosity models, including one-equation models (Spalart-Allmaras, Baldwin-Barth) and two equation models ($k-\varepsilon$, $k-\omega$), (ii) nonlinear eddy-viscosity models, (iii) Reynolds Stress Model (RSM), and (iv) Large Eddy Simulation models. The linear eddy-viscosity models, mainly the two-equation models, are mostly used for practical engineering applications. In this research, the CFD model was evaluated with several formulations of $k-\varepsilon$ and $k-\omega$ models. The following section provides a brief description of the two-equation models, particularly $k-\varepsilon$ and $k-\omega$ models.

3.4.3 Turbulence Models

The $k-\varepsilon$ and $k-\omega$ models are the most common types of turbulence models and have become industry standard to solve most types of engineering problems (Wilcox, 2006). For these two-equation models, the turbulent viscosity is correlated with turbulent kinetic energy (k) and dissipation rate (ε or ω). For a $k-\varepsilon$ model, the correlation can be represented as follows:

$$\mu_t = \rho C_\mu \frac{k^2}{\varepsilon} \tag{3.16}$$

$$k = \frac{u_i' u_i'}{2} \tag{3.17}$$

$$\varepsilon = \mu_t \frac{\partial u_i'}{\partial x_j}\left(\frac{\partial u_i'}{\partial x_j} + \frac{\partial u_j'}{\partial x_i}\right) \tag{3.18}$$

where C_μ is a constant.

The transport equations are solved to obtain k and ε for the $k-\varepsilon$ model, so that the turbulent viscosity can be computed for the RANS equations. By definition, two-equation models include two transport equations to represent the turbulent properties of the flow. This allows a two-equation model to account for history effects like convection and diffusion of turbulent energy. One of the transported variables is the turbulent kinetic energy (k) and the second transported variable varies depending on what type of two-equation model is used. The common choices are the turbulent dissipation rate (ε) for the $k-\varepsilon$ model, or the specific dissipation rate (ω) for the $k-\omega$ model. The second variable can be thought of as the variable that determines the scale of the turbulence (length-scale or time-scale), whereas the first variable (k) determines the energy in the turbulence (Wilcox, 2006).

STAR-CCM+ supports several turbulence models including the one-equation Spalart-Allmaras model, the two-equation $k-\varepsilon$ and $k-\omega$ models, and the Reynolds Stress Model (RSM). In the $k-\varepsilon$ suite of turbulence models, there are the Standard $k-\varepsilon$ model, Realisable $k-\varepsilon$ model and RNG $k-\varepsilon$ model. In the $k-\omega$ model suite,

there are the Standard $k-\omega$ model, Wilcox's modified $k-\omega$ model and SST $k-\omega$ model (STAR-CCM+, 2012).

The two transport equations for the standard $k-\varepsilon$ model can be written as

$$\frac{\partial}{\partial t}(\rho k)+\frac{\partial}{\partial x_i}(\rho k U_i)=\left[\left(\mu+\frac{\mu_t}{\sigma_k}\right)\frac{\partial k}{\partial x_j}\right]+P_k+P_b-\rho\varepsilon\delta_{ij}-Y_m+S_k \tag{3.19}$$

$$\frac{\partial}{\partial t}(\rho\varepsilon)+\frac{\partial}{\partial x_i}(\rho\varepsilon U_i)=\frac{\partial}{\partial x_j}\left[\left(\mu+\frac{\mu_t}{\sigma_\varepsilon}\right)\frac{\partial\varepsilon}{\partial x_j}\right]+C_{1\varepsilon}\frac{\varepsilon}{k}(P_k+C_{3\varepsilon}P_b)-C_{2\varepsilon}\rho\frac{\varepsilon^2}{k}+S_\varepsilon \tag{3.20}$$

where

$$P_k=-\rho u_i' u_j'\frac{\partial U_j}{\partial x_j} \tag{3.21}$$

$$P_b=\beta g_i\frac{\mu_t}{\mathrm{Pr}_t}\frac{\partial T}{\partial x_i} \tag{3.23}$$

$$\beta=-\frac{1}{\rho}\left(\frac{\partial\rho}{\partial T}\right)_t \tag{3.24}$$

and $C_{1\varepsilon}$, $C_{2\varepsilon}$, $C_{3\varepsilon}$, , σ_ε, σ_k are model constants.

For the $k-\omega$ model, the transport equations are

$$\frac{\partial k}{\partial t}+U_j\frac{\partial k}{\partial x_i}=\tau_{ij}\frac{\partial U_i}{\partial x_j}-\beta^* k\omega+\frac{\partial}{\partial x_j}\left[(\upsilon+\sigma_k\upsilon_T)\frac{\partial k}{\partial x_j}\right] \tag{3.25}$$

$$\frac{\partial\omega}{\partial t}+U_j\frac{\partial\omega}{\partial x_i}=\alpha\frac{\omega}{k}\tau_{ij}\frac{\partial U_i}{\partial x_j}-\beta\omega^2+\frac{\partial}{\partial x_j}\left[(\upsilon+\sigma_\omega\upsilon_T)\frac{\partial\omega}{\partial x_j}\right] \tag{3.26}$$

where

$$\upsilon_T=-\frac{k}{\omega} \tag{3.27}$$

and β^*, β, σ_k, σ_ω and α are the model constants.

Another important closure relationship for RANS models is the near-wall treatment equations. The near-wall region is important in turbulence flow modeling as it is the main source of turbulence generation during fluid flow. Accurate turbulence

modeling typically requires successful treatment of the near-wall effects. The default near-wall treatment model "All y+ Wall Treatment" available in the STAR-CCM+ code was used in this research for all the simulations conducted in this research.

3.4.4 Conservation of Energy

The energy equation can be written in two different formulations, i.e., in terms of specific enthalpy or temperature. The choice of one rather than the other form depends on the particular type of problem or numerical considerations. The enthalpy form of the conservation equation, which is used in this thesis, is

$$\frac{\partial}{\partial t}(\rho H)+\frac{\partial}{\partial x_j}(\rho U_j H + F_{h,j} - U_i \tau_{ij}) = -\frac{\partial p}{\partial x_j}+\frac{\partial \tau_{ij}}{\partial x_j}+S_i U_i + S_h \tag{3.28}$$

where $H = \frac{u_i' u_i'}{2} + h$ and $h = c_p T - c_p{}^0 T^0 + H^0$.

Here S_h is the energy source, h is the enthalpy, c_p is the specific heat at constant pressure and temperature T, $c_p{}^0$ the specific heat at constant pressure at reference temperature (T^0 = 293 K) and H^0 is the formation enthalpy of the substance. The diffusive energy flux ($F_{h,j}$) is given by

$$F_{j,j} = -k\frac{\partial T}{\partial x_j} + \rho u_j' h' \tag{3.29}$$

where

$$\rho u_j' h' = -\frac{\mu_t}{\sigma_{h,t}}\frac{\partial h}{\partial x_j} \tag{3.30}$$

Also, due to turbulence, a diffusive energy flux appears. This flux is associated with the fluctuations of the enthalpy and velocity average field. In the turbulent viscosity model these average quantities are obtained from equation (3.30). All the equations discussed so far, from equations (3.1) to (3.31), and other relevant equations are solved iteratively to describe the fluid flow and heat transfer behaviour.

3.5 Fluid Film Formulation and Numerical Implementation

Droplets impacting on the target are considered to lose all their momentum perpendicular to the wall. They do not leave the calculation domain, but are further tracked. The approximation of full momentum loss is chosen, as it is closest to the buildup of a liquid film on the target wall and a shear-off at the wall edge.

The fluid film model accounts for transport of conserved quantities within the film and an interaction with surroundings. STAR-CCM+ uses calculations that include mass conservation, momentum conservation and energy conservation. Major assumptions made in the basic model formulation are that the film is thin enough for boundary layer approximation to apply, that the film stays attached to the boundary unless an internal or separate model predicts film separation, and there is a parabolic velocity profile across the film.

These film assumptions were employed to simplify the transport equations to essentially a 2-D surface model. Due to the thin nature of the liquid film, the flow in the direction normal to the surface can be assumed negligible. In addition, the diffusive transport of mass/momentum/energy in the surface-normal direction will dominate the tangential diffusion. In other words, advection can be treated in the wall-tangential direction and diffusion processes in the wall-normal direction.

The film governing equations are integrated over the volume of fluid film in each film cell to obtain a set of algebraic equations. This integration and discretization is not much different from the ordinary finite volume discretization which is applied to ordinary cells.

The discretized equations of mass and momentum are solved in a segregated manner. The energy equation can either be solved segregated or as part of the coupled system of equations.

3.5.1 Film Dynamics

There are three different forces exerted on a wall film. On the gas side, the gas flow tends to drive the film moving along the same direction. On the wall side, the

viscous friction tends to resist the film movement. There is also the force due to the impingement of additional mass.

The force per unit film area on the gas side is:

$$\tau_g = \frac{1}{2} f \rho_g \left| u - u_{film} \right| \left(u - u_{film} \right) \tag{3.31}$$

where f is friction factor, a function of the gas and flow Reynolds number, and u_{film} is film surface velocity.

For the laminar flow region, where Re < 3000, f can be approximated as:

$$f = \frac{16}{\mathrm{Re}} \tag{3.32}$$

For the turbulent flow region, where Re > 4000, f can be approximated as:

$$f = \frac{0.0791}{\mathrm{Re}^{0.25}} \tag{3.33}$$

For the transitional region, the friction factor is calculated using linear interpolation between the laminar and turbulent flow regimes.

The force per unit film area on the wall side due to the viscous friction is

$$\tau_w = 2 \mu_f \frac{u_{film}}{\delta} \tag{3.34}$$

where δ is the film thickness. Lastly, the force per unit film area due to the impingement momentum is

$$\tau_{imp} = \frac{\sum m_p V_t}{A \Delta t} \tag{3.35}$$

where m_p is mass converting into the film within a given sub-volume during the time step, V_t is tangential component of the droplet velocity, A is film area within a given sub-volume and t is timestep size. Thus, the overall force balance on the film gives the equation for the film motion:

$$\rho_f \delta \frac{du_{film}}{dt} = \tau_g + \tau_w + \tau_{imp} \tag{3.36}$$

3.6 Governing Equation for Fluid Film

3.6.1 Mass Continuity

The mass continuity equation is given as

$$\frac{d}{dt}\int_{v}\rho_f\, dV+\int_{A}\rho_f\,(V_f-V_g).\,da=\int_{v}\frac{S_m}{\delta}\,dV \tag{3.37}$$

The volume V and the surface A are functions of the film thickness and its partial distribution. Here ρ_f is the film density, h_f is the film thickness, V_f is the film velocity and V_g is the grid velocity. The quantity S_m is the mass source per unit wall area due to droplet wall impingement (splashing, sticking, spreading), film separation, or user-defined sources,

$$S_m = S_{m,imp} + S_{m,splsh} \tag{3.38}$$

The impingement source $S_{m,imp}$ is defined as the mass accumulation over a surface area for a given amount of time

$$S_{m,imp} = \frac{\sum_i m_{imp,i}}{A\Delta t} \tag{3.39}$$

The amount of mass impinging on any given surface is computed via interfacing with the Lagrangian particle tracking in the gas phase. The source terms for splashing are defined similarly. The model for splashing is taken from Bai et al. (2002).

3.6.2 Conservation of Momentum

The momentum source terms are split into pressure based (tangential gradients in wall-normal forces) and stress based (forces tangential to wall). The momentum equation, integrated over film height, is

$$\frac{d}{dt}\int_{v}\rho_f\, v_f\, dV+\int_{A}\rho_f\, v_f\,(v_f-v_g).\,da=\int_{A}\tau_f.\,da-\int_{A}p_f.\,da+\int_{V}\left(p_f\, f_b+\frac{\bar{S}_m}{h_f}\right)dV \tag{3.40}$$

where $\bar{S}_m$ is the momentum source corresponding to the mass source S_m, p_f is the pressure, f_b is the body force (for example, gravity), and τ_f is the viscous stress tensor within the film. The kinematics and dynamic conditions at the interface between the film and the surrounding fluid (film free surface) have to be satisfied, i.e.,

$$\left(v_f\right)_{\text{int}} = \left(v\right)_{\text{int}}$$

$$\left(\tau_f . da + p_f . da\right)_{\text{int}} = \left(\tau . da + p . da\right)_{\text{int}} \tag{3.41}$$

The quantities without the subscript f are associated with the surrounding fluid.

3.6.3 Pressure Source Terms

The pressure term, *p*, comprises forces in the wall-normal direction and consists of spray impingement, splashing, surface tension, hydrostatic pressure head, and local gas-phase pressure. Pressure can be expressed as

$$p_f(\xi) = p_{\text{int}} - S_m . n - \rho_f f_b . n\left(h_f - \xi\right) + \int_{\xi}^{h_f} \frac{\partial}{\partial t}(\rho_f v_f . n)\, d\xi \tag{3.42}$$

where *n* is the wall surface unit vector pointing towards the film and ξ is the local coordinate normal to the wall. The above expression assumes that the force S_m is applied at the film free surface.

3.6.4 Conservation of Energy

The energy conservation equation is given as

$$\frac{d}{dt}\int_V \rho_f E_f dV + \int_A \left[\rho_f H_f \left(v_f - v_g\right) + v_g p_f\right]. da =$$

$$\int_A q_f'' . da + \int_A \tau_f . v_f\, da + \int_V f_b . v_f dV + \int_V \frac{S_u}{h_f} dV \tag{3.43}$$

where E_f is the film total energy, H_f is the film total enthalpy, q'' is the film heat flux, T_f the fluid viscous stress tensor, f_b is the body force and S_u is the energy source/sink term per unit film area, which could be, for example, due to droplet wall impingement, film separation, or user-defined sources. The energy source term S_u is expanded as:

$$S_u = \dot{q}_g - \dot{q}_w + S_{u,imp} + S_{u,splash} + S_{u,sep} \tag{3.44}$$

3.7 Modeling of the Heat Transfer in Spray Cooling

There are three modes of heat transfer associated with spray cooling. 1) conduction due to the droplets contact with the surface. 2) convection associated with the bulk air flow and droplet cooling of the thermal boundary layer. Heat transfer induced by wall nucleation bubble, secondary nucleation bubbles, environmental heat transfer and radiation has been neglected due to surface temperature being below the saturation temperature of the water droplet.

Contact heat transfer of the impinging droplet can be classified into two types – heat transfer with wetting contact occurring at lower surface temperature and heat transfer with non-wetting contact occurring at higher surface temperature.

3.7.1 Wetting and Non-wetting Droplet Heat Transfer

At wetting heat transfer, the droplets can be in continuous or semi-continuous direct contact with the wall. After an initial period of heat transfer by transient conduction, the droplets enter into nucleate or transition boiling regimes. In this case, the droplet incoming Weber number may have a weak effect on enhancing the droplet breakup. Wet cooling surface results in a significant drop in the surface temperature due to its significant cooling efficiency.

In non-wet cooling, also referred to as film boiling, a significant amount of water vapour is generated between the hot surface and droplet, thus preventing direct contact. Since vapour has a very low thermal conductivity, it acts as insulation between the surface and the incoming spray, therefore, lowering the cooling efficiency. In the cooling regime, the incoming droplet velocity (or Weber number) has a significant influence on the cooling efficiency. For low velocities, droplets cannot penetrate through the film layer. For high velocities, droplet can penetrate through the film layer, and more surface contact can be established. This enhances the cooling efficiency.

3.7.2 Parameters Affecting Droplet Contact Heat Transfer

The droplet diameter affects the Weber number, and has a strong influence on the cooling efficiency. A small diameter would cause an increase in the cooling effectiveness as compared to a larger diameter. This is due to the large surface coverage area achieved

when using fine mist. However, very fine mist may cause an adverse effect if the droplets are not large enough to hit the surface and as a result may be carried away by the air jet stream.

Besides the surface temperature and droplet Weber number (which is a function of diameter and velocity), there are other secondary factors influencing the heat transfer effectiveness but not as influential as the preceding ones. These include: droplet impingement frequency, surface inclination angle, droplet impinging angle, surface material and surface roughness.

The effect of the droplet impingement frequency and surface material is influenced by the surface temperature, while droplet impingement angle and surface roughness influence the impingement frequency increases due to the interference between the liquid film layer and the droplets. This effect weakens at temperatures above the Leidenfrost point because the vapour film layer prevents the droplets from making contact.

Surface high conductivity increases the heat transfer rate if the surface temperature is below the Leidenfrost point. However, if the temperature is above the Leidenfrost the high thermal conductivity promotes vapour film production which eventually reduces the heat transfer rate. Surface roughness performs favourably in promoting the heat transfer rate since the droplet breaks into many parts at a much lower Weber number than the critical Weber number for a smooth surface.

3.8 Energy Balance for a Material Particle

A material particle is assumed to be internally homogeneous which, from a thermal point of view, implies a low Biot number, e.g. less than ~0.1. The generic form of the equation of conservation of energy consistent with this assumption is

$$m_p c_p \frac{dT_p}{dt} = Q_t + Q_s \tag{3.45}$$

In this equation, Q_t represents the rate of convective heat transfer to the particle from the continuous phase and Q_s represents other heat sources.

If the two-way coupling model is active, Q_t is accumulated over all the parcels and applied in the continuous phase energy equation. Figure 3.3 illustrates the interfacial transport processes.

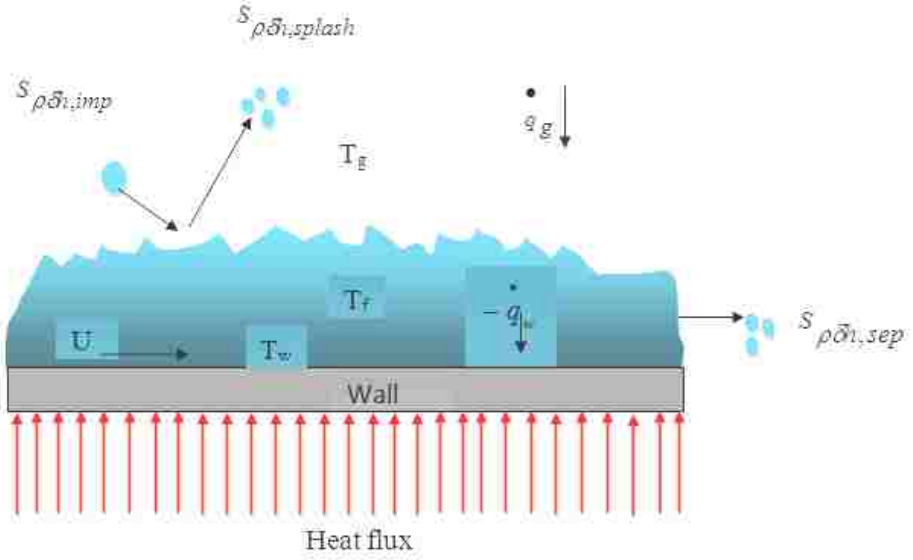

Figure 3.3 Interfacial transport processes of heat

3.8.1 Heat Transfer Coefficient

The heat transfer coefficient (HTC) *h* must be defined using a correlation, but not necessarily empirical. It is often given in terms of the particle Nusselt number

$$Nu_p \equiv \frac{h\, D_p}{\kappa} \tag{3.46}$$

where κ is the thermal conductivity of the continuous phase. STAR-CCM+ provides two methods for defining the heat transfer coefficient, the Ranz-Marshall correlation and a field function specification.

The Ranz-Marshall correlation is suitable for spherical particles up to R_p~5000. It is formulated as:

$$Nu_p = 2(1 + 0.3 R_p^{1/2} \mathrm{Pr}^{1/3}) \tag{3.47}$$

where *Pr* is the Prandtl number of the continuous phase and R_p is the droplet's Reynolds number. This correlation is available only when the continuous phase is viscous. The field function heat transfer coefficient method allows *h* to be specified directly with a scalar field function, *f*, i.e.

$$f = f(h) \tag{3.48}$$

Chapter 4. Validation of the CFD Model

In this Chapter, the specific details of the CFD model and results of its validation are presented. It starts with a brief introduction of the experimental data used for the validation. In the second part, the mesh and model are described and the CFD results are compared with the corresponding experimental data.

4.1 Experimental Data Used for Validation

The experimental data reported by Karwa et al. (2007) has been chosen to evaluate the CFD model and validate the simulation results. The experimental study was focused on non-boiling heat transfer from a horizontal surface by a pressure atomized water spray. A schematic of the heater-target assembly is shown in Fig. 4.1.

The assembly consisted of a cylindrical copper block whose upper part was 20 mm in diameter and 100 mm in length. The lower part of the block was made larger in diameter to accommodate four cartridge type heaters, each of 330 W, 160 mm long, and 16 mm in diameter. The heaters were connected in parallel and capable of supplying more than 1000 W to the top surface of the upper part. All the experimental setup data is summarized in Table 4.1.

Table 4.1 Experimental setup data of Karwa et al. (2007)

Target diameter (mm)	Coolant type	Target surface average temperature (° C)	Coolant temperature (° C)	Number of heaters	Cartridge size (mm)	Thermocouple locations (mm)	Heat generated by each cartridge (W)
20	Water	95	25	4	Height: 165 Width: 16	11.8, 22, 32	300

Knowing the distance between the thermocouples and the distance between the thermocouples and the heater surface makes it possible to predict the heat flux and the surface temperature using the one-dimensional Fourier law of heat conduction. The experiments were performed at steady state and adiabatic conditions. The hot plate surface temperature was maintained below 95ºC. Three cases with the same type of nozzle (cone spray) were chosen from the experiments. Since the spray cone angle varies

with the nozzle type and operating pressure, the nozzle-to-target spacing H_t was adjusted between 18 and 29 mm so that the whole spray falls on the heated target surface. The nozzle axis was kept always normal to the surface.

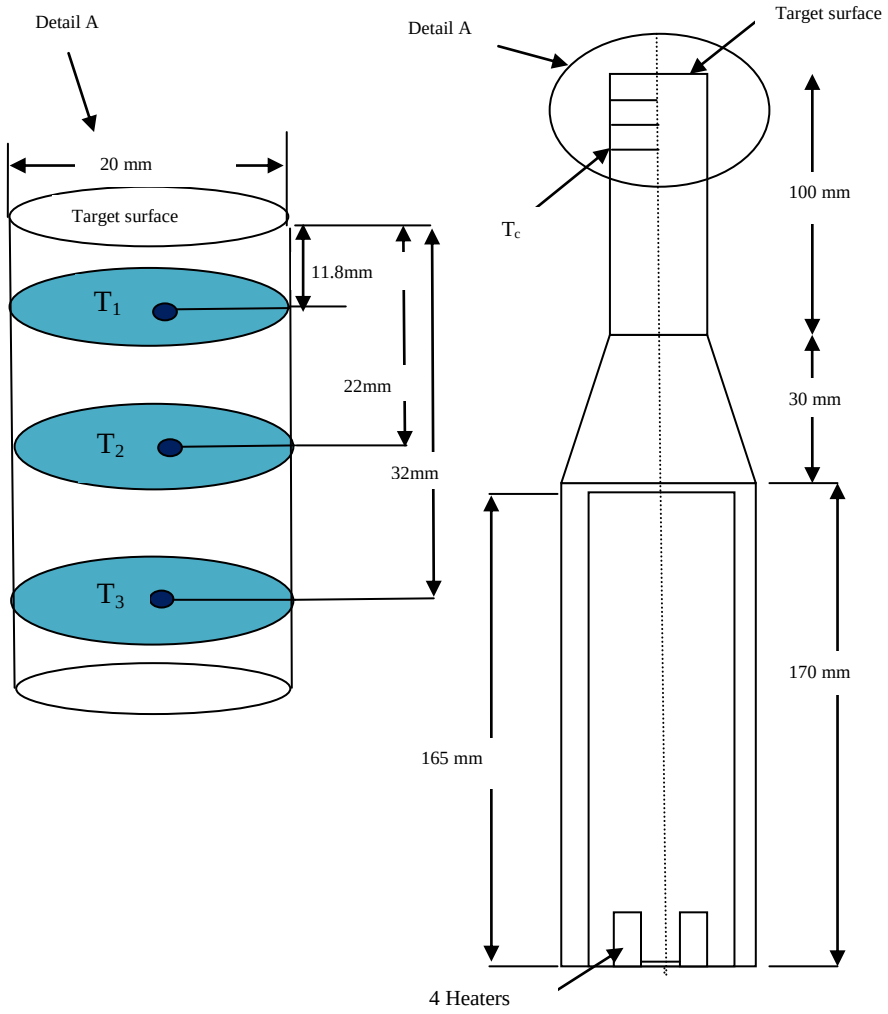

Figure 4.1 Schematics of the heater-target assembly for Karwa et al. (2007) experiment

The spray mass flux varied from 6.21 to 8.78 kg/m^{2}s, which gives a spray Reynolds number of 162 to 230 based on the target surface diameter. Under steady state conditions, the heat transfer coefficient was between 17,800 and 21,000 W/m^2 K. Table 4.2 shows the operating details of the experiments conducted by Karwa et al (2007).

4.2 Spray Parameters

The heat transfer coefficient, *h*, of spray cooling can be defined as

$$h = \frac{q}{T_{surface} - T_{inlet}} \tag{4.1}$$

where q is the heat flux, $T_{surface}$ is the heating surface temperature, which was obtained by extrapolation from the mean temperature of the three layers, and T_{inlet} is the fluid temperature at the entrance of the nozzle.

The Nusselt number can be defined in terms of the heat transfer coefficient as

$$Nu = \frac{h D}{\kappa} \tag{4.2}$$

where D is the diameter of the heated target. The spray Reynolds number is calculated from the following formula

$$\mathrm{Re} = \frac{G D}{\mu_w} \tag{4.3}$$

where G is the mass flux of water based on unit area of the target surface and μ_w is the viscosity of the water. The Weber number is defined as

$$We = \frac{\rho \upsilon^2 d_{32}}{\sigma_w} \tag{4.4}$$

where d_{32}, ρ_w, σ_w, υ are droplet diameter, fluid density, surface tension and mean droplet velocity, respectively.

Table 4.2 Operating parameters, Karwa et al. (2007)

Nozzle number	Operating pressure (kg/cm^2)	Mass flux, G (kg/m^2 s)	Orifice diameter d_0(μm)	Sauter mean diameter d_{32} (μm)	Droplet velocity, υ (m/s)	Nozzle-to-surface spacing H_t (mm)
Unijet # 1 **Case 1**	1.44	6.21	510	149.2	16.8	29
Unijet # 1 **Case 2**	2	7.32	510	137.1	19.9	20
Unijet # 1 **Case 3**	3	8.78	510	123.4	24.3	18

The mean droplet velocity υ impacting the surface is given by the following equation developed by Ghodbane and Holman (1991) from simple energy balance considerations around the nozzle,

$$\upsilon = (\upsilon_1^2 + \frac{2\nabla P}{\rho} - \frac{12\sigma}{d_p \rho})^{1/2} \quad (4.5)$$

where υ_1 is mean velocity of water entering the nozzle, ∇P is the pressure drop across the nozzle and d_p is the mass median droplet diameter. Researchers have estimated that only the second term on the right side of equation (4.5) is significant. Therefore, equation (4.5) is simplified to

$$\upsilon = (\frac{2\nabla P}{\rho})^{1/2} \quad (4.6)$$

Mudawar and Estes (1996) developed a correlation for the Sauter mean diameter,

$$\frac{d_{32}}{d_0} = 3.07[\frac{\rho_g{}^{1/2} \nabla P d_0{}^{3/2}}{\sigma^{1/2} \mu}]^{-0.259} \quad (4.7)$$

where d_o is the diameter of the nozzle orifice, μ is liquid dynamic viscosity and ρ_g is gas density at ambient temperature. The Weber number can be calculated by using the values of Sauter mean diameter and mean droplet velocity from equations (4.7) and (4.6), respectively. The thermophysical properties of water used in the calculations correspond to the pre-impingement temperature of the water.

4.3 CFD Modeling Procedure in STAR-CCM+

Computational Fluid Dynamics (CFD) modeling and analysis in STAR-CCM+ consists of building a three-dimensional thermal model and simulating flow and heat transfer. The steps followed to perform the CFD analysis are:

- Create a geometry
- Mesh the model
- Select physics models
- Define initial and boundary conditions
- Specify convergence criteria
- Run the simulation

- Post-process results

Relevant details of these steps are elaborated in the following sections.

4.3.1 Modeling Geometry in STAR-CCM+

For any simulation in STAR-CCM+, the first step is to prepare the geometry of the case under investigation. The geometry parts manager provides an optional feature that can be used to make the meshing setup for an analysis easier and more efficient. This geometry could come from a model prepared previously in a CAD package, or could be created directly using the 3-D CAD module within STAR-CCM+.

For this research, the geometry was developed in STAR-CCM+ as shown in Fig. 4.2. For this set of simulations the domain size was $30 \times 30 \times 40$ cm^3. The thermal model was developed and the unsteady simulations were performed for various scenarios of inlet pressure and mass flow rate to predict the experimental data.

4.3.2 Meshing

Meshing is an important step of a CFD analysis since an inappropriate mesh configuration could lead to inaccurate result or numerical instabilities. A separate study was undertaken for grid resolution and its effect on the results. Before proceeding further into an investigation, it is necessary to determine whether the solution is grid dependent or not. It is well known from the fundamentals of numerical analysis that a coarse mesh provides less accurate results, whereas a finer mesh should provide better predictions. However, after a certain refinement level, if the changes in the results are negligible, there is no benefit in refining the grid further. Another practical limitation on the degree of grid refinement is that the computational time increases as the grid is refined. Therefore, an optimal mesh configuration is required that provides a balance between computational time and solution accuracy.

Meshing involves choosing appropriately small grid spacing in regions of highest gradients (e.g., near walls and constrictions) and selecting larger spacing for the far field. Since the region of primary concern in this study is the heater surface, the grid was built with prism layers close to the heater surface, followed and ending with a coarse grid at

the top boundary. This reduces the total number of cells in the mesh and hence improves the computational time.

A grid independency test was performed based on Case 1 (see Table 4.2). The number of cells, from coarse to fine grid, was 115000, 228000 and 600000. Figure 4.3 shows the different mesh sizes used to investigate grid independency. The results for the rate of heat transfer versus time, as shown in Fig. 4.4, indicate that there is almost no difference between the 115000, 228000 and 600000 cell sizes in terms of the quasi-steady values of the HTC. As a result of the mesh independency, the rest of the simulations were performed with a mesh of 228000 cells.

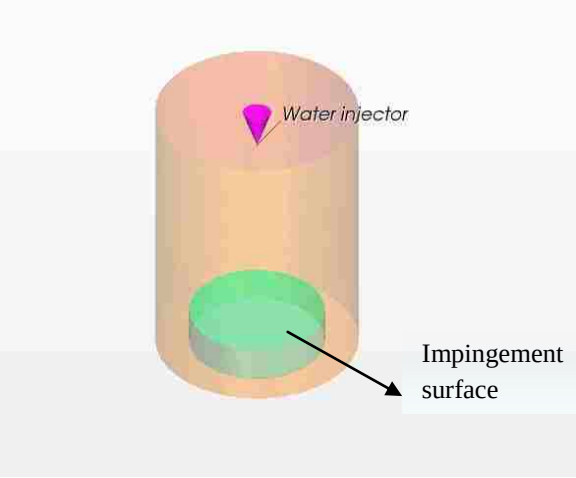

Figure 4.2 Geometry of the CFD model including the domain, water injector and target surface

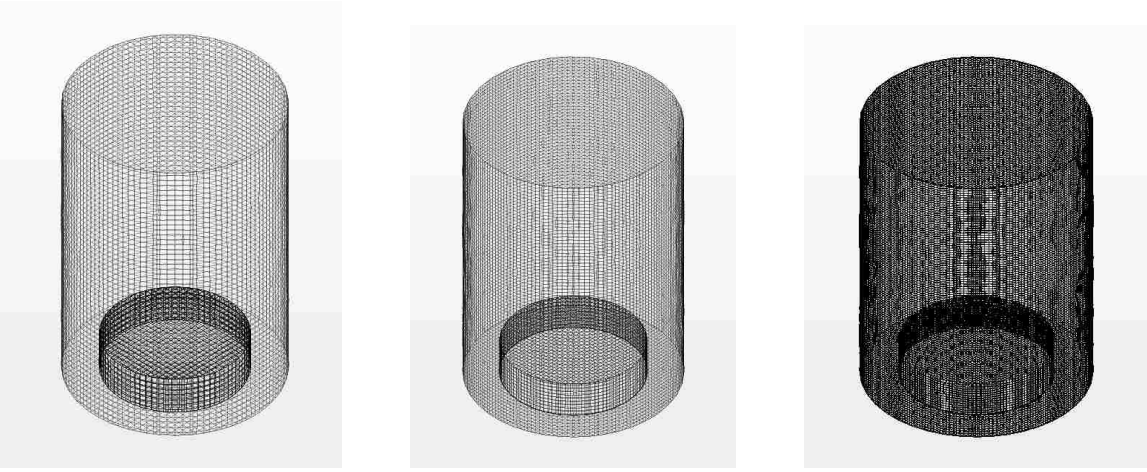

(a) (b) (c)

Figure 4.3 Different mesh sizes: a) 115000 cells, b) 228000 cells and c) 600000 cells

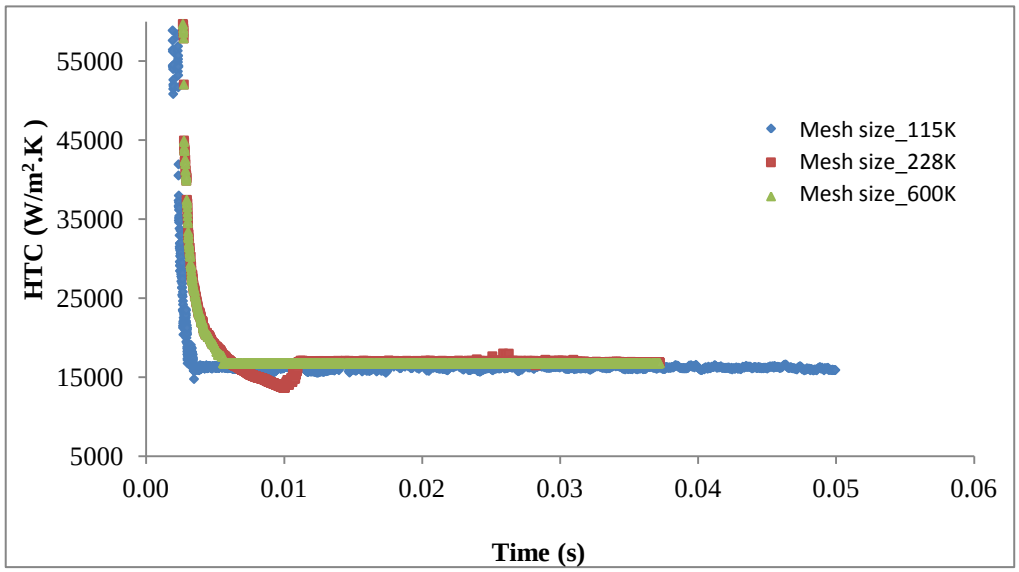

Figure 4.4 Mesh independency for Case 1showing the time history of calculated heat transfer coefficient for three different mesh sizes; 115000, 228000, 600000 cells

4.3.3 Physics Models

The physics models also form an integral part of the CFD simulation. These models are used to define the fluid type, flow modeling, energy modeling, turbulence modeling, thermophysical properties, discretization schemes and simulation conditions. The physics models listed below were used to perform the case studies.

- Reynolds-Averaged Navier-Stokes
- Turbulence model (k-ω and SST k-ω)
- All y+ wall treatment
- No slip boundary condition on the walls
- Unsteady implicit simulation
- Flow loop: Second-order upwind convection scheme
- Energy loop: Second-order scheme
- Gravity
- Coupled energy model
- Coupled flow model
- 2-way coupling between continuous phase (gas phase) and discrete phase (droplet)
- Single phase fluid (H_2O) with no phase change

- Constant properties (density, viscosity, thermal conductivity)
- Laminar film fluid with constant density
- Heat flux at the top surface and adiabatic wall for the skirt surface
- Bai-Gosman wall impingement model
- Taylor Analogy Breakup (TAB) model
- Multi-phase interaction model
- Water injector defined, with solid cone spray
- Mass flow rate from the spray is distributed uniformly throughout the impingement
- No phase change or dry out of liquid
- Spray droplet size distribution function: Rosin-Rammler

For the wall impingement, the Bai-Gosman (Bai et al., 2002) and Satoh models (Satoh et al., 2000) are available. The Satoh wall impingement model provides a method for modeling the behaviour of oil droplets in a “blow-by” flow as they encounter the walls, baffles and porous plates of an oil-mist separator. The Bai-Gosman wall impingement model provides a methodology for modeling the behaviour of droplets impacting on a wall and, in particular, attempts to predict how and when droplets break up or stick to the wall. This model is used with impermeable boundaries (wall, contact and baffle) as well as with the fluid film.

The modified Bai-Gosman model was chosen for the current study as it is the most widely used model for this type of application. Since the Weber number in this case is low, the TAB breakup model is a reasonable choice. The TAB breakup model uses the Taylor Analogy to determine when and how the droplets breakup under the action of aerodynamic forces. The Liu drag coefficient method uses the TAB Distortion to modify the drag coefficient of distorted droplets consistent with their non-spherical form. Activating the TAB Distortion model also activates the Liu drag coefficient method if the drag model is active. It is not entirely clear whether the droplets undergo any further breakup from their point of injection until they reach the solid surface. However, the above models were picked to account for any possible breakup.

4.3.4 Boundary and Initial Conditions

The initial condition for fluid film was zero thickness. Uniform droplet velocity was assumed at the tip of the nozzle and uniform heat flux was applied at the bottom of the hot plate (similar to Karwa's experiments). The operating and boundary conditions of Table 4.2 were used. The boundary types for the CFD model are shown in Fig. 4.5.

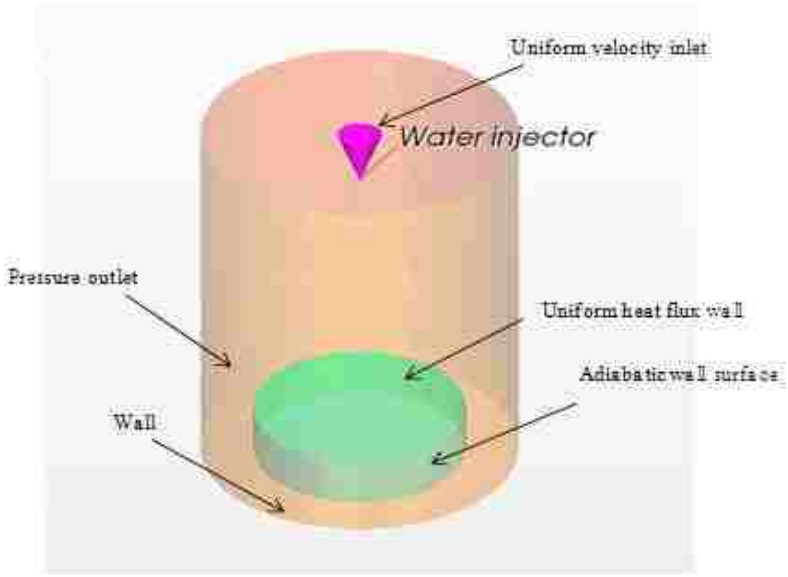

Figure 4.5 Boundary conditions for validation case

4.3.5 Convergence Criteria

CFD algorithms solve the non-linear conservation equations and the solution techniques use an iterative process to improve a solution, until 'convergence' is reached. The criteria for convergence are typically decided based on knowledge of the problem and the CFD code. The parameters that control how many times the procedure is repeated can be specified by the user. In the case of a transient simulation the number of iterations is repeated at each time step until the convergence criterion is satisfied. This number is dictated by the overall residual reduction desired; the program calculates a residual for each variable at each iteration. This residual is the sum of the residuals for that variable at each computational cell. In this study, the iteration is done until the average residue for each node reduced to less than 10^{-4}.

Table 4.3 Parameters used for convergence of the simulation

Time step (sec)	Model	Flow & energy model	Solver	k-ω turbulent viscosity	k-ω turbulence under relaxation factor	Maximum inner iterations
10^{-6}	k-ω SST	Coupled	Implicit unsteady, second order	0.7	0.8	5

4.4 Fine Tuning

Solution stability and convergence are important factors in a CFD simulation and therefore need to be carefully monitored. One advantage of the coupled solver is that CPU time scales linearly with the cell count; in other words, the convergence rate does not deteriorate as the mesh is refined. The Coupled Energy model is an extension of the Coupled Flow model. Together, they solve the conservation equations for mass, momentum and energy simultaneously using a time (or pseudo-time) marching approach. This formulation is particularly robust for solving compressible flows and flows with dominant source terms, such as buoyancy. Coupled Flow and Energy modeling provides the flexibility to fine tune the solver parameters, primarily the relaxation coefficients in the velocity, pressure and energy loops. From computational experience, it was found that fine tuning during the progress of the simulation is essential to guarantee stability and convergence. One of the important tools for fine tuning the CFD model is the under-relaxation factor (URF). Overall, higher URF values make the solver aggressive and possibly unstable, while lower values make it less aggressive and more stable.

4.5 Spray Parameters

The spray typically forms a conical shape where the amount of spreading is represented by an angle θ. The spray mass flux and the angle are related. The spray angle θ was calculated based on the data that was provided by Karwa et al. (2007), as illustrated in Fig. 4.6, given by

$$\theta = \tan^{-1} (BC/AC) \quad (4.8)$$

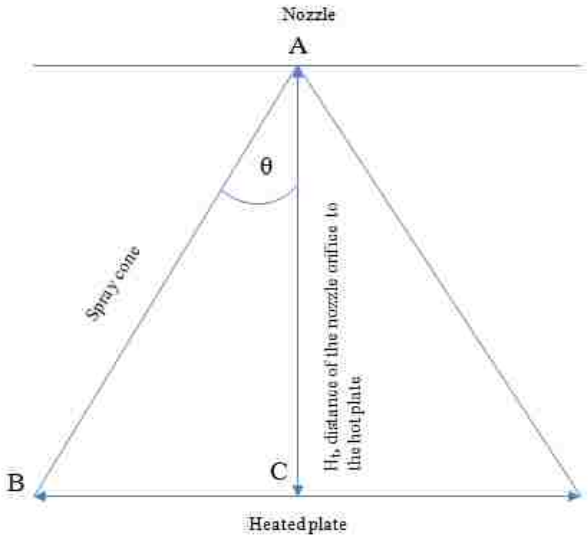

Figure 4.6 Model setup for measuring the spray angle

According to Karwa et al. (2007), a simple heat transfer analysis of his setup indicated that the heat loss from the copper block in the radial direction is less than 1% of the supplied heat flux. Generally, according to the Fourier conduction law, the heat flux q is calculated by the temperature gradient in the axial direction, assuming one-dimensional thermal conductivity, described as

$$q = \kappa \frac{T_1 - T_2}{d_1} \tag{4.9}$$

where T_1 and T_2 are the mean temperature of the two layers in the heater, d_1 is the distance between the two layers, and κ is the thermal conductivity of hot plate.

4.6 Results

This section provides results for the cases outlined in Table 4.2, which are based on the experiments by Karwa et al. (2007). Figure 4.7 shows a typical instantaneous plate temperature and particle size distributions in the metal for Case 1. Different colors on the small spheres represent different droplet sizes. Also, colors on different parts of the solid show the temperature values. The heat starts to be removed from the areas of the solid close to the liquid film. As the time progresses, larger areas within the solid start to cool down due to heat transfer from the liquid film to the hot solid object.

Figure 4.8 shows the velocity vectors of the spray droplets for all three cases. The distance from spray nozzle to the target surface varies between these cases. For case 3, this distance is the smallest which leads to the formation of large vortical structures near the plate.

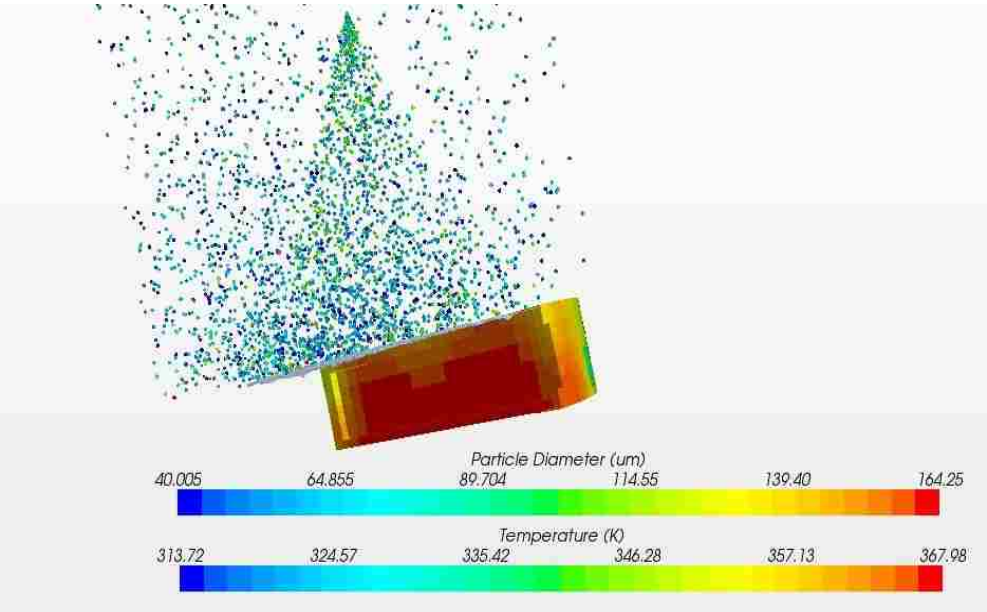

Figure 4.7 Solid temperature and particle diameter distributions for Case 1 at 15 *msec*

Figure 4.9 shows the film thickness for the three cases. In order to maintain the full coverage of the plate by spray droplets, case 3 has the highest spray angles which involves higher droplet velocities and mass flux, while the droplet sizes are the lowest for this case. This leads to higher lateral velocity and ultimately thinner fluid film. Thinner film leads to thinner boundary layer thickness and higher heat removal rate.

In Fig. 4.10, the temporal variation of average HTC at the wall for the three cases is illustrated. The variation of the HTC with mass flux *G* is clear. For obtaining an acceptable value of HTC, the simulation needs to be run for long enough so that the "quasi-steady" condition is achieved. Even though the spray parameters such as the droplet diameter and velocities vary, mass flux has been found to be the dominant factor that influences heat transfer. By increasing the mass flux, the HTC increases. The average mass flux is used in defining the Reynolds number and is directly proportional to this number. When the Reynolds number is increased, the heat flux increases with the increasing of mass flux, as discovered by Wang et al. (2011) and Karwa et al. (2007).

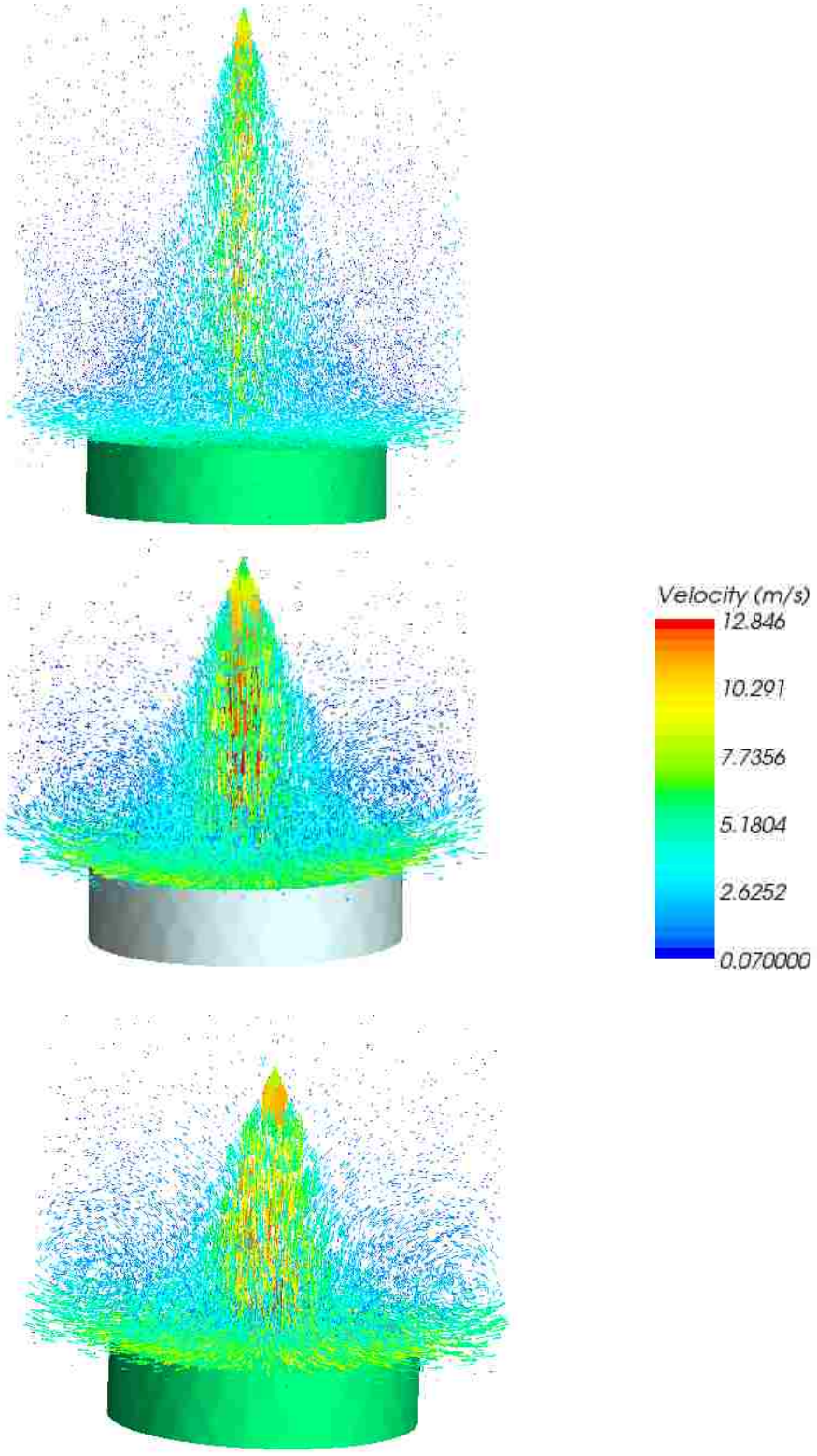

Figure 4.8 Spray droplet velocity vectors visualized for Case 1 (top), Case 2 (middle) and Case 3 (bottom) at 15 *mse*c. Spray to wall distance and spray angle vary for each case

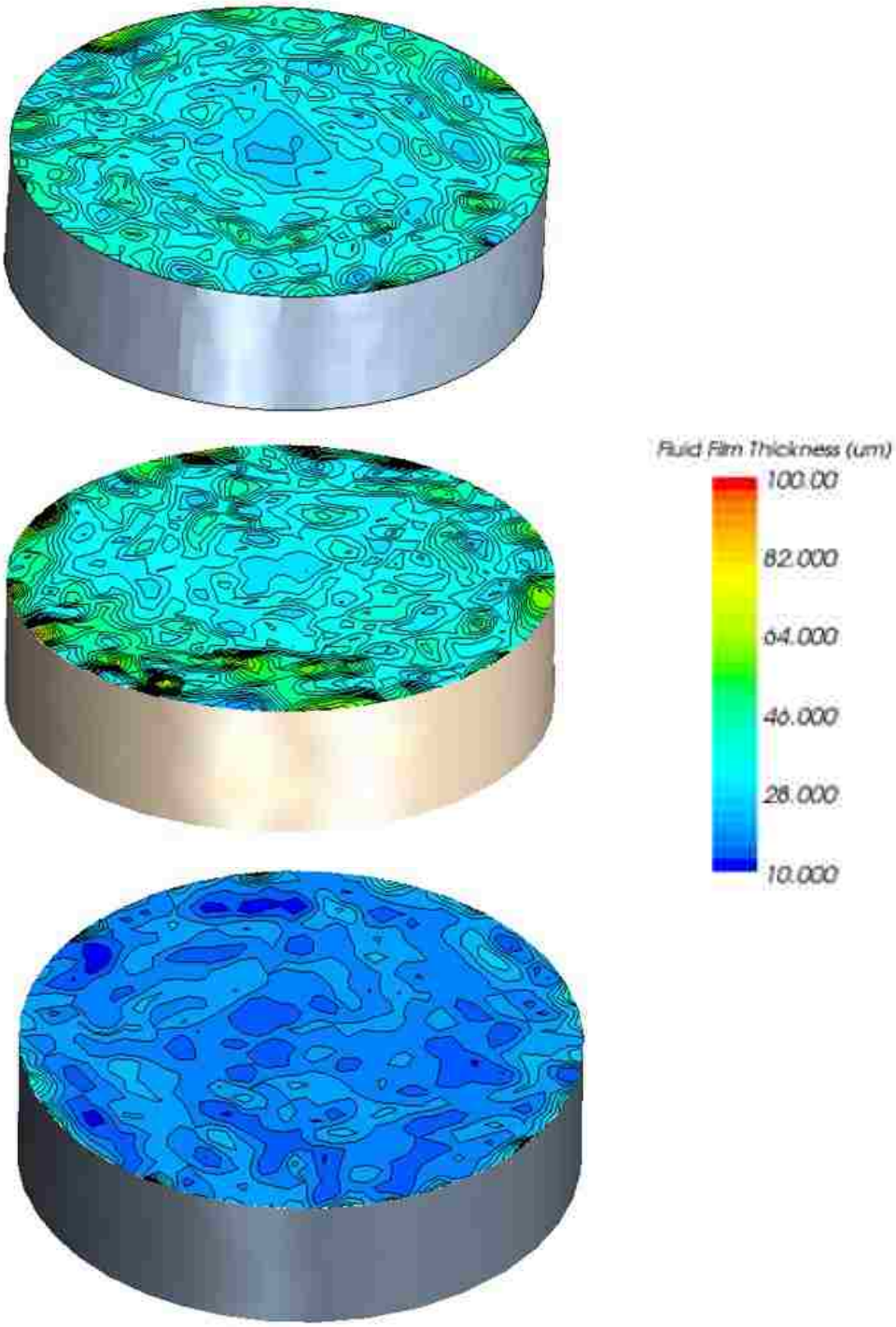

Figure 4.9 Film thickness distribution on the solid surface for Case 1 (top), Case 2 (middle) and Case 3 (bottom), respectively at 15 *msec*

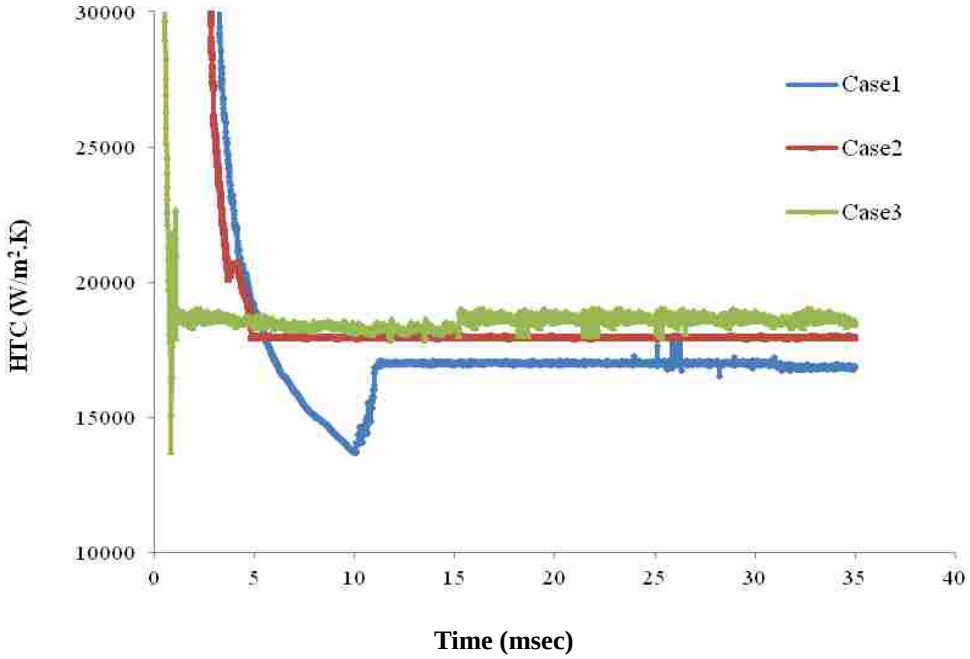

Figure 4.10 Heat transfer coefficient variation as function of time for different mass flux

It is noteworthy that the surface temperature in the present study was maintained below 95 °C. Therefore, it can be concluded that, in the current study, the evaporation does not have a significant impact on the heat transfer and the majority of heat is transferred by single phase convection to the water droplets and film formed on the hot surface.

Figure 4.11 shows that the HTC decreases in the radial direction from the centre to the edge of the metal plate. At higher radii (further from the centre of the circular plate) the film decelerates and both the film and thermal boundary layer become thicker, hence resulting in a drop in HTC. Another factor contributing to the lower HTC could be that the liquid coolant's temperature has already increased as it reaches the edges of the plate. As the droplet density increases, the droplet–film heat transfer increases, further reducing the surface temperature. It is observed that as the mass flux increases the HTC goes up, which is consistent with the findings of Freund et al. (2006).

Freund et al. (2006) reported that the peak values directly above the nozzle increase as the flow rate increases. The heat transfer rate directly above the spray is high, but as the fluid moves out radially along the surface, the fluid loses its momentum and the heat transfer coefficient declines which are similar to observations made in the

current study. This pattern also matches the results obtained by Pautsch (2004), who found the highest performance of heat removal observed at the centre with the lowest performance of the heat removal occurring at the edges. As the spray flow rate increases, droplet momentum introduces more agitation to the liquid which enhances the mixing effect. This will enhance the heat transfer locally, and increases the heat transfer coefficient.

The behaviour of circumferentially averaged temperature of the hot plate as a function of radius is shown in Fig. 4.12. The temperature distribution of the heated surface is non-uniform. By increasing the mass flow rate, higher temperature reduction rate can be achieved at the centre of the plate. Approximately, a reduction of 4°C in the mean surface temperature is observed numerically when the flow rate increases from 6.21 to 8.78 kg/m^{2}s.

The variation of HTC with the flow rate is shown in Fig. 4.13. It shows a reasonable agreement with the results of Karwa et al. (2007). Oliphant et al. (1998), using air-assist spray impingement cooling, showed that the heat transfer coefficient is strongly dependent on mass flux in the non-boiling regime, which it was also reported by Wang et al. (2011) and Lin and Ponnappan (2003).

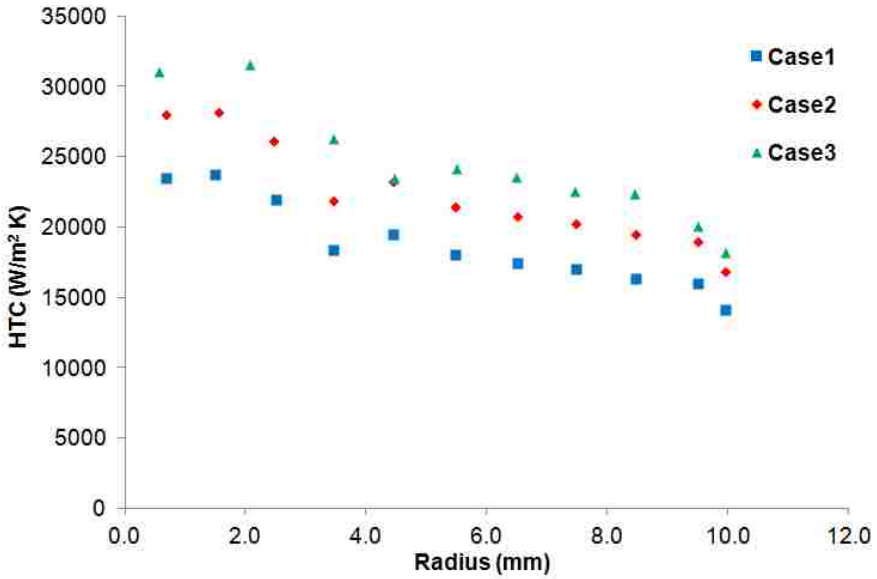

Figure 4.11 Heat transfer coefficient (HTC) distribution versus surface radius

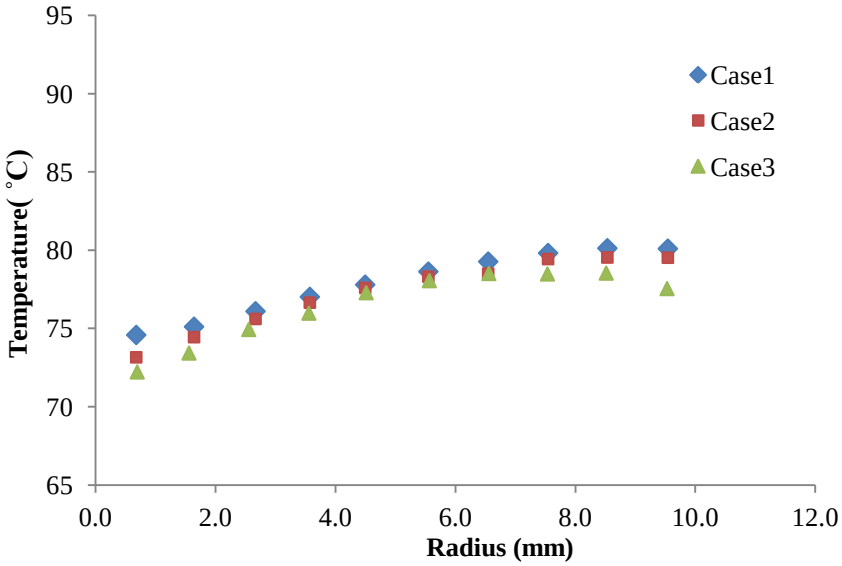

Figure 4.12 Temperature variations versus surface radius

Because of the interaction of the two effects mentioned above and the inability to only control drop velocity or mass flux, it is difficult to study the influence of a single parameter on the heat transfer. Mudawar and Estes (1996) argued that the mass flux, not the droplet velocity, was the dominant factor for heat transfer performance. As a result of increased mass flux, the combined effect of mixing and unsteady boundary layer evolution leads to the enhanced heat transfer rates. The level of the enhancement depends on the boost in mass flux which is characterized by the number of droplets per second, velocity and diameter.

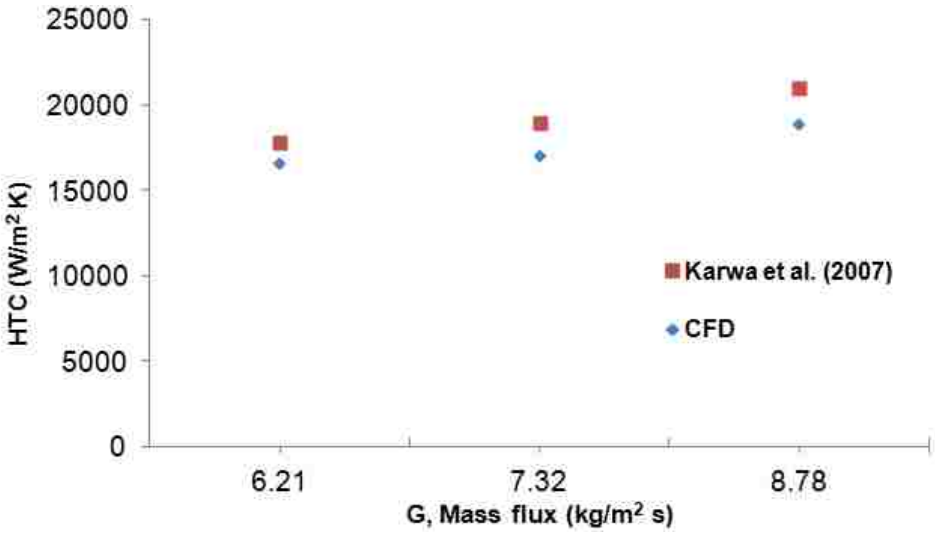

Figure 4.13 Heat transfer coefficient versus mass flux

Figure 4.14 presents the CFD results obtained under various operating conditions of the spray system (different cases), with a spray nozzle distance to the plate ranging between 29 and 18 mm, and Reynolds number varying between 162 and 230. In the three cases considered, the nozzle supply pressure changes between 1.41 (for Case 1) and 2.94 bars (for Case 3).

As mentioned before, the supply pressure conditions, the water flow rate, the droplet size and the characteristics of the spray under the operating conditions tested are summarized in Table 4.1. Karwa et al. (2007) have developed the following correlation for Nusselt number based on the spray Reynolds number:

$$Nu = 20.344\,\mathrm{Re}^{0.6589} \tag{4.10}$$

Wang et al. (2011) have introduced a relevant correlation which reads

$$Nu = 0.12.75\,\mathrm{Re}^{0.9322}\,\xi^{2.2485} \tag{4.11}$$

where $\xi = \dfrac{T_{wall}}{T_{boiling} - T_e}$ and T_{wall} is the wall temperature, $T_{boiling}$ is the boiling temperature of the working fluid and T_e is the environment temperature.

Table 4.4 shows simulation results compared with the experimental data and correlation by Karwa et al (2007), as well as the correlation by Wang et al. (2011). The CFD results are within 10% of the experimental data. The agreement between the numerical and experimental results in Fig. 4.14, which shows the Nusselt number as function of spray Reynolds number for different cases, is satisfactory.

Table 4.4 Comparison of simulation results and experiments

Case number	Calculated HTC (W/m^2K)	Calculated Nusselt	Experimental HTC (W/m^2K)	Experimental Nusselt	Estimated error (%)
Case #1	16591.84	528.7	17800	576.2	8.2
Case #2	17277.83	550.6	19000	605.5	9.1
Case #3	19170.04	610.9	21000	669.2	8.7

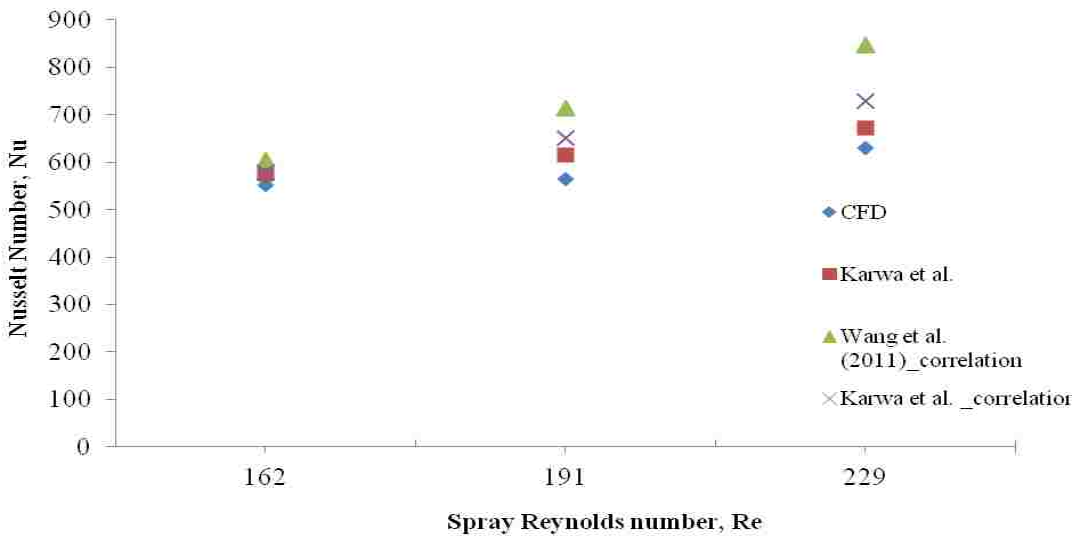

Fig. 4.14 Comparison of CFD results with Karwa et al. (2007) and Wang et al. (2011)

Chapter 5. Experimental Setup and Procedure

5.1 Introduction

This chapter provides details of the measurements performed on the spray cooler system of the Heinz Canada plant in Leamington, Ontario. Heinz Canada has been a manufacturer of ketchup, tomato juice, pasta sauces and other food based products for over a century. Heinz was interested in optimizing the operation of its Spin Cooler systems used to cool canned tomato juice and in extending its use to cooling of other tomato based products.

The Spin Cooler system is mainly used as part of the tomato juice manufacturing process. At the exit, the cans are sent for final packaging. A significant amount of lake water and energy is consumed in the cooling process. Overall, Heinz uses more than 600,000,000 US Gallons (USG) per year of water at the Leamington plant, of which about 40,000,000 USG/year is used for the Spin Coolers. The Spin Cooler system consists of a series of stationary nozzles from which water flows in the form of droplets. These nozzles impinge water droplets onto the hot cans as they pass along the conveyor system. A schematic of the Spin Cooler System was shown in Fig. 5.1.

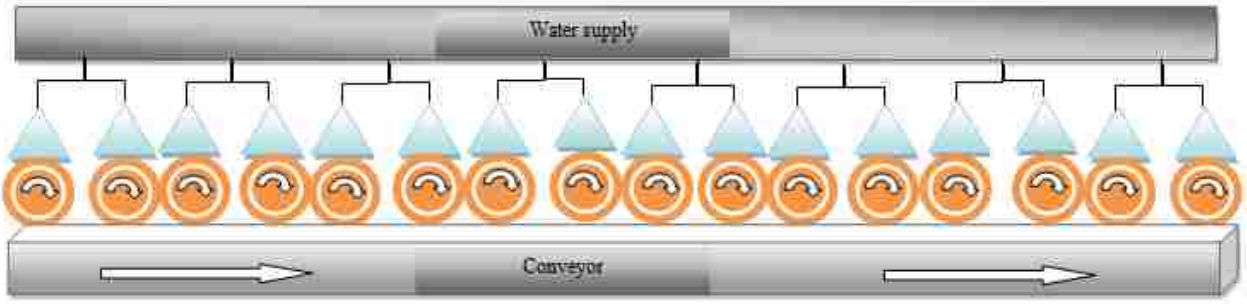

Figure 5.1 Schematic depicting moving tomato juice cans while spinning on a conveyor

5.2 Cooling Process

A nozzle used in one of the lines in Heinz is depicted in Fig. 5.2, and its properties are listed in Table 5.1.

Figure 5.2 A sample nozzle used in Heinz spray cooler

Table 5.1 Parameters of nozzle

Nozzle orifice diameter. (µm)	Nozzle angle	Approximate pressure (psi)	Droplet diameter. (µm)
6756	68º	30	0.452

The full cone spray nozzle was setup in the lab under the same pressure as the operating pressure at Heinz to examine its performance, as shown in Fig. 5.3.

Figure 5.3 The spray nozzle while running at the lab

In Heinz, after the filling and seaming process, the tomato juice cans are carried on the conveyor at the ambient temperature for about 4 to 5 minutes. During this period of time, the can temperature drops between 3 to 4 °C on average due to air convection. Figure 5.4 shows a still photo of tomato juice can movement and the lines of stationary

nozzles spraying water droplets onto the hot cans. Tomato juice cans vary in sizes, such as 0.540 L, 1.36 L and 2.84 L, referred to as small, medium and large as pictured in Fig. 5.5. Other properties of the cans utilized in Heinz are shown in Table 5.2.

Figure 5.4 Spray cooling setup in Heinz

Figure 5.5 Different sizes of cans used for tomato juice production

Table 5.2 Data for the cans used in Heinz

Size (L)	Can dimensions diameter/height (cm)	Material type	Wall thickness (mm)
0.540	8.3 / 11.6	Tin plated steel	0.175
1.36	11.5 / 17.7	Tin plated steel	0.21
2.84	15.3 / 17.7	Tin plated steel	0.26

5.3 Spray Nozzle

Three types of production lines in Heinz carry different size of cans. There are between 57 to 76 nozzles mounted on the water supply pipe line to impinge water droplets onto the hot can surfaces. Depending on the line and can size, different height of nozzle is observed. Specific information is summarized in Table 5.3.

Table 5.3 Conveyor characterization carrying different size of tomato juice cans

Can size (Liter)	Length of conveyor (m)	Total number of nozzles	Conveyor's speed (m/s)	Height of nozzle (m)	Flow rate (L/s)	Distance between the nozzles (m)
0.540	36	57	0.22	0.30	1.5	0.6
1.36	35.35	76	0.118	0.43	1.5	0.79
2.84	76.25	74	0.054	0.34	0.57	0.46

Cans filled with hot tomato juice (around 92 ºC) produced out of fresh tomato are sealed off at the start of the canning process. Next, the cans start their journey on the conveyor (while experiencing convection with air) until they reach to the bath section (bath length is around 2 m). Depending on the size of the cans, a different length of conveyor is used. Hence the duration of spray cooling time and speed of conveyor are different.

It is very important that no post-process contamination occurs through the package seals or seams. Therefore, the seal integrity is vital, and there are strict regimes for container handling to minimize abuse to the seals. There is evidence that cans do not create a hermetic (gas-tight) seal while they are hot, because of the expansion of the metal in the double seams. Good practice in canneries avoids manual handling of hot and wet cans to reduce the risk of post-process introduction of microbial contaminants into the container (Coles et al., 2003).

In Heinz, impinging the water droplets on the hot cans is responsible for the cooling process. The conveyor belt can create rotation in order to induce mixing inside the can by agitation in axial rotation, where the cans rotate in a horizontal plane, and thus increase the rate of heat transfer from the centre (i.e. slowest cooling point) of the can. The volume of the slowest cooling zone (SCZ) can be reduced with the help of rotation.

Typical rotation speeds can vary between 2 and 30 rpm, depending on the strength of the can and the convective nature of the food inside the can, (Coles et al., 2003). For example, a plastic pouch containing rice would be rotated slowly (e.g. 2–5 rpm) so that the delicate pack and its contents are not damaged. However, the rotation suffices to reduce the process times to an extent that economic gains are made and measurable quality benefits are achieved. For sealed tin plated steel cans, the rotational speed can be much higher.

The conveyor uses the ability of the metal can to roll along a constrained pathway. The conveyor forces the cans to rotate about their axis where gravity maintains contact between the cans and the metal can guides. In general, it is claimed in most cases that the quality of agitated products is by far superior to those processed by the static method, (Coles, 2003).

5.4 Preliminary Experimental Data

Different trips were made in 2011 and 2012 to the Heinz plant to gather information including measuring tomato juice temperature at different stages, nozzle flow rates and conveyor speeds. In 2011, the measurements were done manually using thermometers. Below are some of the data obtained from the Heinz system.

The conveyor was divided into four sections, A, B, C and D with different lengths. Measured average time for a can to travel the whole conveyer was done in several attempts. Run #1: 276 sec., Run #2: 193 sec. and Run #3: 218 sec. Gathered information in 2011 are summarized in Tables 5.4 to 5.8.

As can be seen in Table 5.4, there are two columns indicated, T_{bb} and T_{ab}. T_{bb} and T_{ab} represent before bath and after bath, respectively. A can was divided into three

segments including bottom, middle and top. The temperature of the can was measured for these three segments and averaged as shown in the Table 5.4.

Table 5.4 Measured temperature values for bath section (water temperature: 28.9-29.5˚C)

	T_{bb}			T_{ab}		
	1st Attempt (°C)	2nd Attempt (°C)	Averaged value (°C)	1st Attempt (°C)	2nd Attempt (°C)	Averaged value (°C)
Bottom	77-84	75	80	81-82	88-89	85
Middle	91	91	91	89-91.5	92	90
Top	96	96	96	93	90	91

In Tables 5.5-5.8, T_A, T_B, T_C and T_D represent the temperature of the can for section A, B, C and D, respectively. There are four lines of tomato juice cans moving along the conveyor horizontally. Two lines inside are called inner and two lines outside are called outer.

Table 5.5 Measured temperature values for location A (water temperature: 25.4-25.6 ˚C)

	T_{bb}			T_{ab}		
	1st Attempt (°C)	2nd Attempt (°C)	Averaged value (°C)	1st Attempt (°C)	2nd Attempt (°C)	Averaged value (°C)
Bottom	77-84	75	80	81-82	88-89	85
Middle	91	91	91	89-91.5	92	90
Top	96	96	96	93	90	91

Table 5.6 Measured temperature values for location B (water temperature: 28.9-29.5 ˚C)

	T_B	
	Outer row ((°C)	**Inner row** (°C)
Bottom	60.5	56.1
Middle	58.2	59.1
Top	58.2	55.7
Averaged Value	58.96	57

Table 5.7 Measured temperature values for location C

T_C		
	Outer row (°C)	**Inner row** (°C)
Bottom	48.5	51.1
Middle	50.6	46.5
Top	47.1	42.7
Averaged Value	48.7	46.8

Table 5.8 Measured temperature values for location D

T_D			
Outside the spray zone (°C)			
	First Attempt	Second Attempt	Averaged value
Bottom	48.7	44.9	46.8
Middle	45.8	45	45.4
Top	46	46.1	46.05
Averaged Value			44.7

5.5 Analytical Approach

The cooling of objects is often described by a law, attributed to Newton, which states that the temperature difference of a cooling body with respect to the surroundings decreases exponentially with time. Such behaviour has been observed for many laboratory experiments, which led to a wide acceptance of this approach. However, the heat transfer from any object to its surrounding is not only due to conduction and convection but also due to radiation. The latter does not vary linearly with temperature difference, which leads to deviations from Newton's law. It is shown that Newton's cooling law, i.e. simple exponential behaviour, is mostly valid if temperature differences are below a certain threshold which depends on the experimental conditions. For any

larger temperature differences appreciable deviations occur which need a complete non-linear treatment. Newton's cooling law (NCL) is expressed as

$$T(t) = T_w + (T_0 - T_w)\, e^{k_N} \tag{5.1}$$

where T_0 is the initial can temperature, T_w is the water temperature and k_N is the decay rate. Assuming k_N is constant for the whole process, it can be calculated by using the formula

$$e^k = \left(\frac{T_1 - T_w}{T_0 - T_w} \right)^{\frac{1}{t_1}} \tag{5.2}$$

where T_1 is the can temperature at the exit section and t_1 is the total time taken for a can to travel throughout the conveyer length .

After analyzing the data, it was noticed that the declining temperature of the can along the conveyor following the same trend as Newton's cooling law (NCL), as shown in Fig. 5.6.

Errors in the temperature measurements may occur due to the presence of thermocouples and possible mixing before accurate local measurement is done. The placement of thermocouples to record the temperature at various positions in a container during cooling also disturbs the flow patterns. Furthermore, it is difficult to measure the temperature at the SCZ because this is a region of the fluid which keeps rolling and moving during the cooling.

The temperature measuring approach was changed to the use of iButtons in 2012. An iButton, as shown in Fig. 5.7, is a portable computer chip enclosed in a 16 mm thick stainlesssteel casing with 512 Bytes of general memory plus 64 Bytes of calibration memory. iButtons have a sampling rate from 1 second up to 273 hours with the accuracy around ±0.5°C and are highly resistant to environmental hazards such as dirt, moisture and shock.

Planted inside the tomato juice right at the filling stage, the iButtons travel with the can along the conveyor. At the exit, cans carrying iButtons were taken off the conveyor and the recorded temperatures were transferred to a computer.

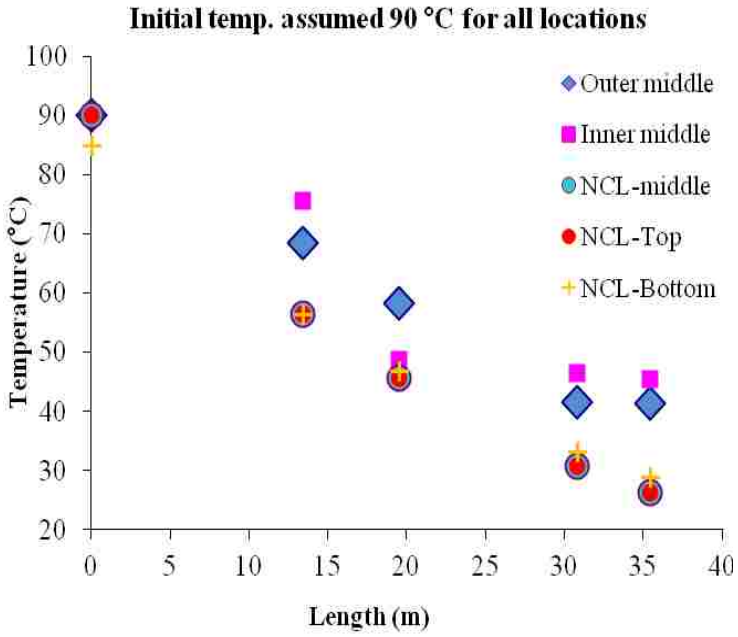

Figure 5.6 Comparison of measured temperature of tomato juice can at different locations with Newton's cooling law

Figure 5.7 Picture of iButton (Maxim Integrated$_{TM}$)

Although iButtons were calibrated by the manufacturer, another calibration was done by using a thermocouple. The calibration graph is shown in Fig. 5.8.

Measured temperature of tomato juice inside a small, medium and large can versus conveyor length travel time is shown in Figs. 5.9 to 5.14. Gathering of field measurement data was done on two different days, day 1 and day 2. All the data for small, medium and large cans was compared with Newton's cooling law (NCL) using equations (5.1) and (5.2). As mentioned earlier, there are four lines of cans moving on the conveyor. In Figs.

5.9 to 5.14, O.L, O.R, I.L and I.R stand for outer left, outer right, inner left and inner right, respectively.

c

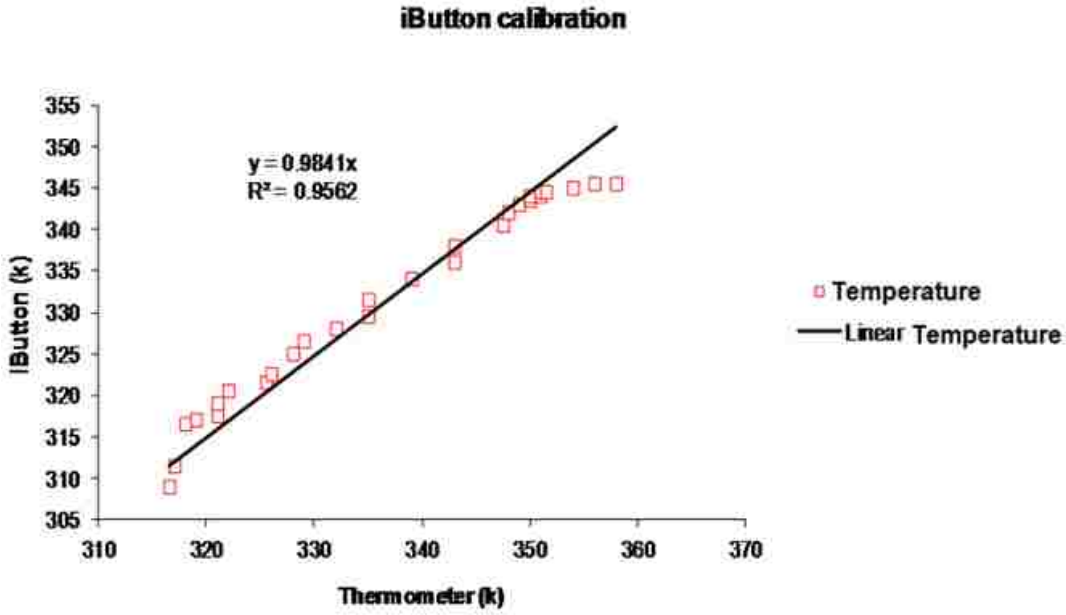

Figure 5.8 Calibration of the iButtons against thermometer

Figures 5.9 and 5.10 show temperature variation versus length of the conveyor and also temperature variation versus total time that can travels, for small cans. Close to the end of the line, it is clear that tomato juice temperature tends to stay constant. The temperature drop appears to be very slow, close to the end of the line, contributed by lower temperature difference between the impingement water temperature and tomato juice temperature inside a can. Therefore, it can be concluded that less number of nozzles or less mass flux is needed close to the exit.

As shown, the graph follows an exponentioal curve. It is clear from Figs. 5.9, 5.11 and 5.13 that the agreement between the NCL and measured information is in a reasonable range.

In Fig. 5.12, it is obvious that temperature of the can on the second day reached to the exit temperature of the can on the first day with almost double the speed of the conveyor. Hence, time can be saved and also the efficiency of the conveyor can be increased to some extent. Large can data is displayed in Figs. 5.13 and 5.14.

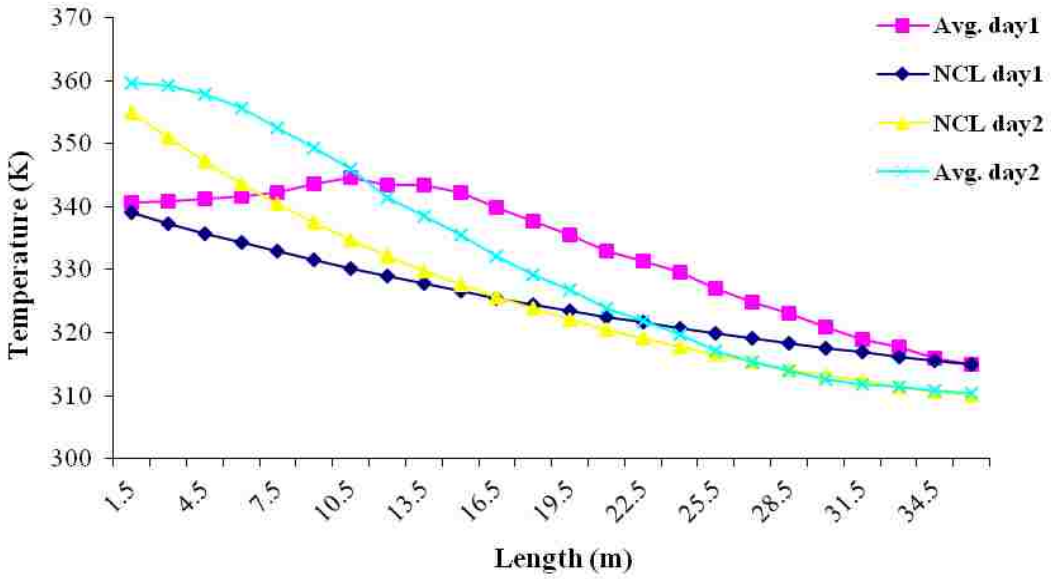

Figure 5.9 Temperature variation of tomato juice inside the small can versus the length of the conveyor from the first nozzle to the exit

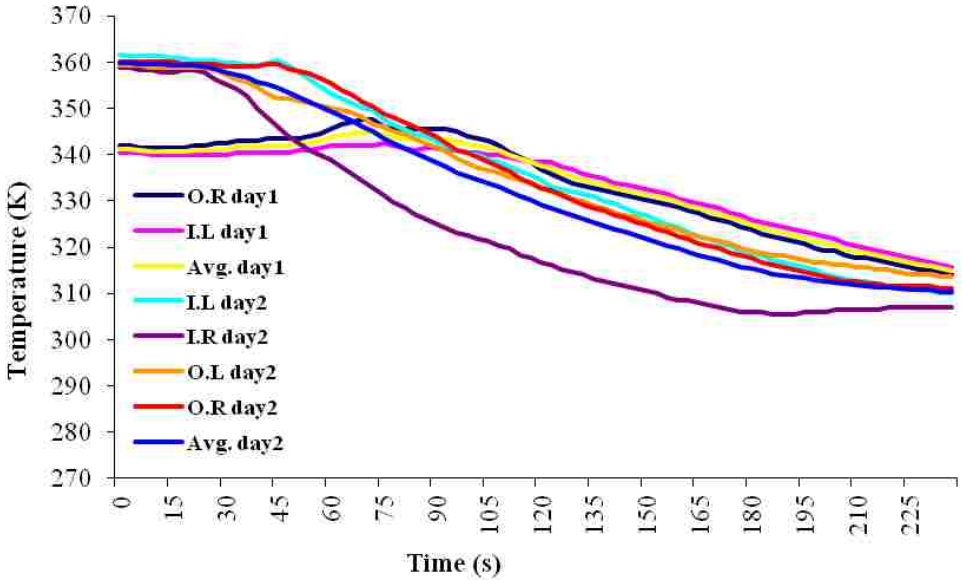

Figure 5.10 Temperature variation of the small can versus traveling time

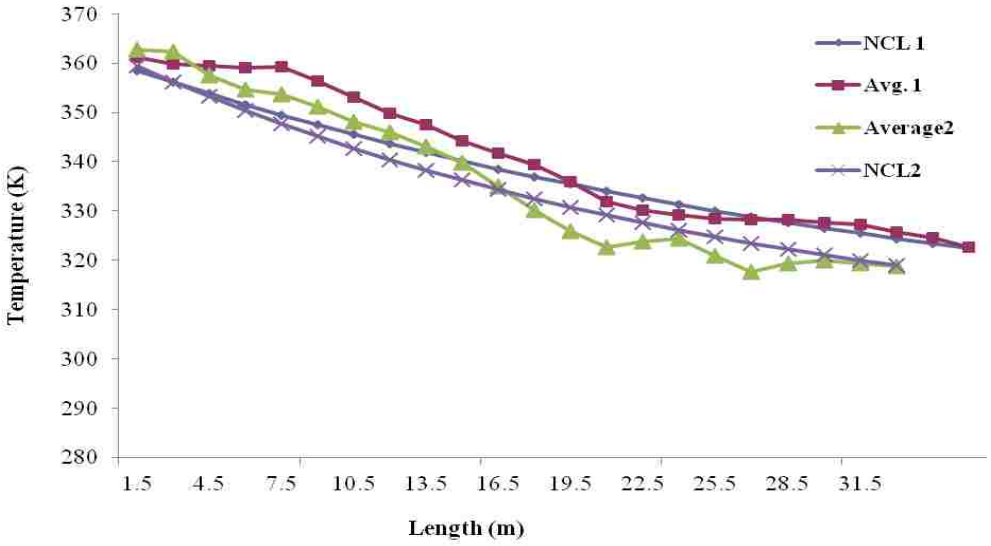

Figure 5.11 Temperature variation of tomato juice inside the medium can versus the length of the conveyor from the first nozzle to the exit

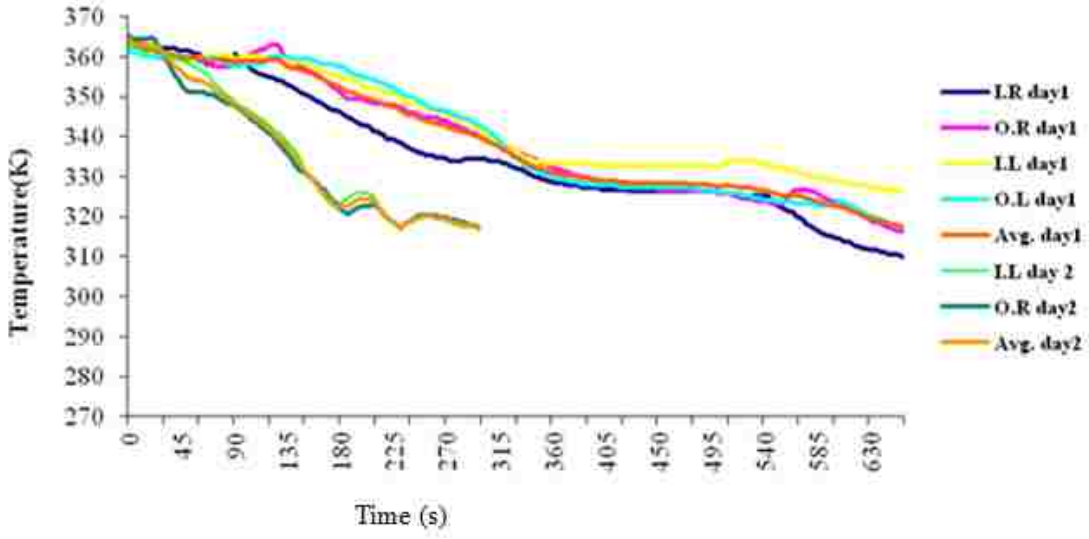

Figure 5.12 Temperature variation of tomato juice inside the medium can versus traveling time

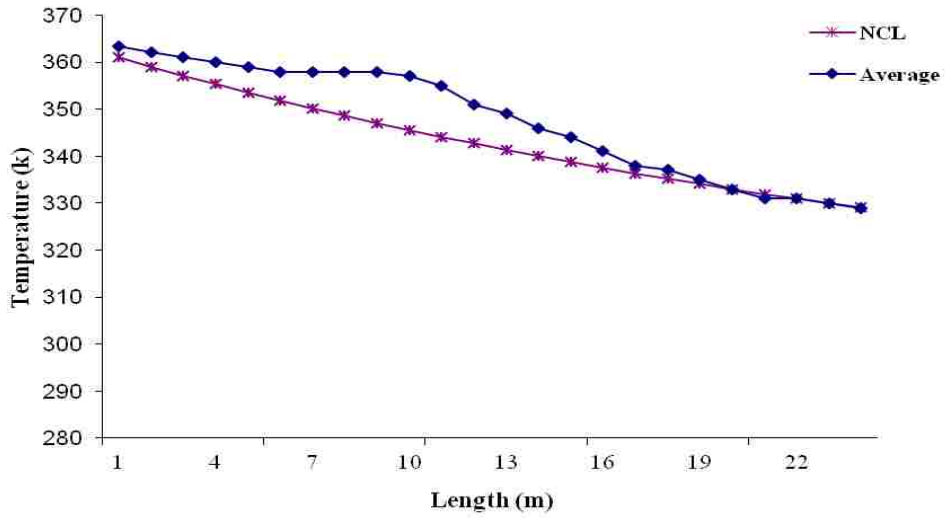

Figure 5.13 Temperature variation of tomato juice inside the large can versus the length of the conveyor from the first nozzle to the exit

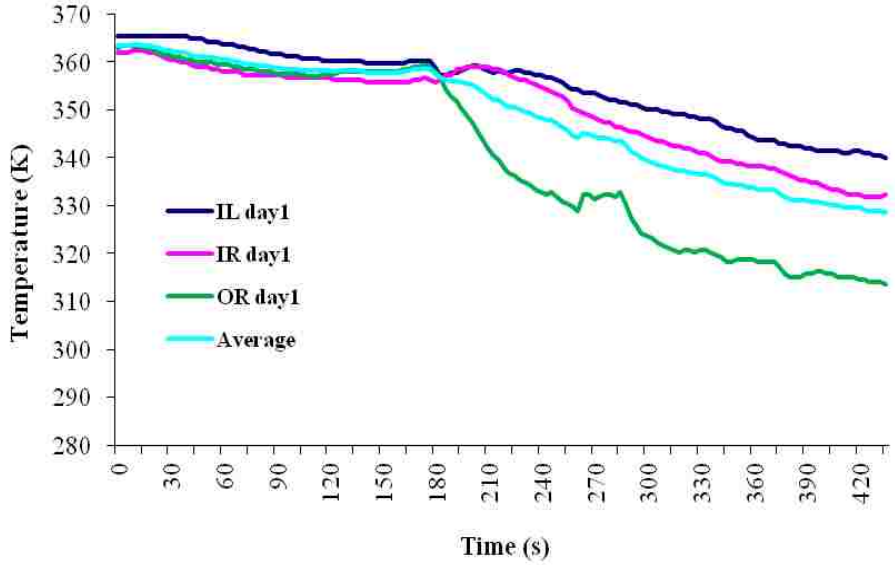

Figure 5.14 Temperature variation of tomato juice inside the large can versus traveling time

The trend of the temperature drop for values recorded by the iButton at the Heinz plant bears resemblance to the theoretical predictions by Newton's Cooling Law (NCL). This shows that NCL could be used to predict the temperature in the intermediate stages of the cooling process for a rough estimate of the cool-down behaviour. Considering the simplicity of the NCL, it does perform reasonably well, especially when other more

refined tools (such as experiments and/or simulation capability) are not available and a fast answer is required.

In order to reduce the volume of the SCZ region, tomato juice cans spin while moving along the conveyor. In addition, by spinning, more uniform tomato juice temperature can be achieved. Due to difficulty in measuring the temperature at the SCZ, prediction of temperature distribution during the cooling process using CFD modeling could be a good step towards understanding the heat transfer. In the next chapter, a simplified model of the tomato juice can is formulated and the simulation is run under the actual conditions at Heinz. The simulation helps gain more insight into the temperature gradient and SCZ size inside the can and their dependence on the rpm.

Chapter 6. CFD Model for Heinz Spray Cooling System

6.1 Introduction

One of the most important processes in the food industry is the heating and cooling of food derivatives and their containers. Canning is still the most effective way to preserve foods and certain heating and cooling procedures are required for each type of food product to ensure it will maintain at least the minimum acceptable quality level. The primary goal of thermal processing is to increase the shelf life and to make food products safe for consumers. This has lead to creation of large food processing plants aiming to supply food products that are sterile, nutritious and economical (Ghani et al., 2003).

Canned products need to be cooled according to a certain thermal map. At the same time, it is vital that the time a can spends on the production line is minimized in order to boost productivity. To this end, rotational processes are applied to liquid and semi-liquid filled cans and containers to enhance the heat transfer rate and reduce processing time and energy consumption. The combined effects of natural and forced convection affect the slowest cooling zone (SCZ) at the centre of the can and cause reduction of SCZ volume due to the rotation influence. Dirita et al. (2006) has found that the SCZ may lie off-centre, depending upon the given thermal boundary conditions.

Rolling and translational motion on a conveyor system is applied to the cans containing liquid foods to increase the heat transfer rates and reduce processing time due to agitation (Tucker et al., 1990). In the case of the Heinz Canada plant which is the focus of this study, the motion that enhances the cooling is the axial rotation. A major challenge to increasing the heat transfer also lies in the viscosity of the food product since the viscosity is a major factor affecting the cooling rate in convectively heated fluids, and the more viscous the food product, the more resistant it would be to the rotation. This also signifies the importance of determining the optimal processing conditions with respect to the physical properties (density and viscosity) of the food product and rotation speed.

Because of the complex nature of the heat transfer in natural convection cooling, determining the size and location of the SCZ is a difficult task. Attempting to record temperature data during cooling at several positions by using thermocouple probes in the

container, even if feasible, would disturb the flow patterns. Since the temperature distribution is very sensitive to the velocity field, the temperature distribution measurement with this approach can cause significant errors.

In this chapter, the rotational speed and its effect on the temperature distribution inside a can of hot fluid as the can rolls, translates and gets exposed to the spray nozzles is investigated. Evolution of temperature with velocity field in the axially rotating can containing hot liquid (tomato juice) is determined at rotational speeds 0 to 50 rpm. Transient temperature and velocity profiles for the cases of forced convection cooling are presented and compared with those for a stationary can where the natural convection effects are the major factor.

6.1.1 Dividing the Problem into 3-D and 2-D parts

Due to the complex nature of a 3-D simulation of cans with moving mesh for creation of rotation inside the can, it was decided to break the problem into two parts. The region outside the can (including liquid film and air) was simulated in 3-D since the liquid film model in STAR-CCM+ can only be used in 3-D. Since the volume inside the can is very large compared with the liquid film region outside, a very large number of grid points would be needed to simulate the flow inside the can. Adding to this large mesh size complication is the very large timeline of cooling which might reach several hundred seconds of physical time. Therefore, it would be impractical to solve the whole flow domain in 3D over such a large period of physical time.

A more practical approach was chosen in which the average heat transfer coefficient (HTC) is calculated on the can in 3-D and time-averaged. The time-averaged 3-D data are once more averaged along the depth of the can to yield proper boundary condition for a 2-D simulation.

There are some assumptions that need to be made in order to simulate this problem in a reasonable computational time:

1) The heat transfer inside the can in the axial direction is negligible and therefore a 2-D model of flow inside the can is sufficient. This assumption is arguably valid since the main motion inside the can is rotation. As a further ad hoc validation of

this assumption, in the actual juice measurements performed at the plant, the centreline temperature from both sides of the can were within 1-3 degrees of that at the middle point.

2) The can is assumed to be 100% filled with liquid juice only. The flow inside the can is solved as a single phase (liquid) only and the possible presence of the air phase and the interface between the juice and air inside the can are not taken into account.

The procedure is explained in more detail. At first, a 3-D domain was created with an injector impinging the droplets on a hot can. The actual operating conditions of the Heinz plant were used to estimate an average heat transfer coefficient. Second, a 2-D domain was introduced and the estimated heat transfer coefficient was applied as a boundary condition to the surface of the 2-D model while the liquid inside was rotating. The objective of this study is to evaluate the combined effect of natural and forced convection on the temperature distribution and location of the SCZ in a 2-D slice of the can filled with liquid. Rotational speeds of 0, 25 and 50 rpm are employed as system (operating) variables. The effect of can rotation has not been previously analyzed for cooling process using computational fluid dynamics (CFD). The 2-D geometry of the horizontal can and the effect of its rotation require efficient CFD analysis. Finally, temperature contours and velocity contours are presented for different rpm and the results are analyzed.

6.2 Geometry

Figure 6.1 shows the geometry for the 3-D and 2-D simulations. The inner part is the fluid region filled with tomato juice initially at 92 ºC. The can thickness is a solid region, measuring about 1 mm. The outer region is a fluid region, which is the continuous phase (air).

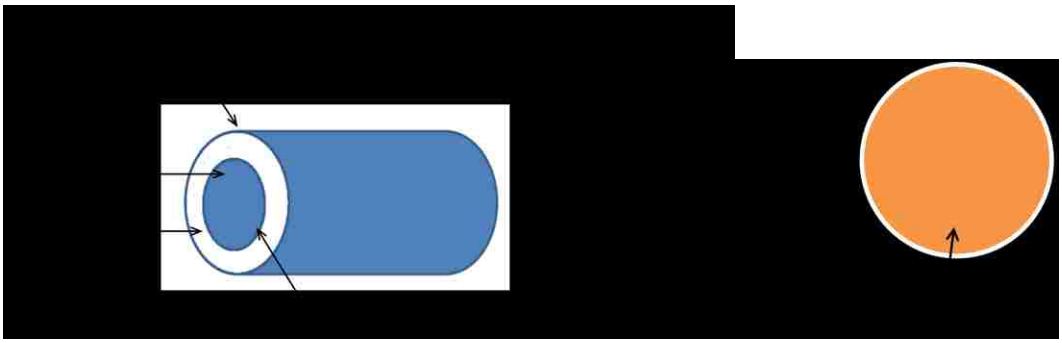

Figure 6.1 3-D and 2- D geometry for the model

6.3 Model Setup

6.3.1 Material Properties

The can and material properties used in the current simulation for model setup are provided in Table 6.1.

Table 6.1 Properties of tomato juice and can used for the simulation

Can size (cm)	Can capacity	Can material and thickness	Thermal resistance of metallic can (W/m K)	Tomato juice conductivity at 100 °C (W/m K)	Tomato juice temperature (°C)	Water spray temperature (°C)	Height of nozzle (cm)
11.5 dia. x17.7 length	1.36L	Tin plated steel/0.21mm	64	0.638	92	32	43.2

In reality, liquid foods are generally non-Newtonian. Based on the information provided by Heinz, 93% of the tomato juice is water and hence the Newtonian assumption is reasonable. In the simulation presented in this work, the viscosity and density are assumed constant.

6.3.2 Solver Settings

For low viscosity liquid food used in the simulation, the viscous force is not high and there is strong evidence that the natural convection flow is not laminar. The liquid velocities due to can rotation and natural convection motion are expected to be high. The thermal resistance of the metallic wall can was considered in the simulation. With the above mentioned assumptions, the partial differential equations governing natural convection motion in a can are the Navier-Stokes equations.

In STAR-CCM+, to create a rotation around the wall in a 2-D model, there is a node called Tangential velocity specification. This node is added when the no-slip method is specified in the shear stress specification. By adding this feature, one has three options including vector, rotation rate and local rotation rate. In this case, tangential velocity is specified as rotation rate about the region's reference frame and a wall rotation node is added to the physical value node.

The coupled unsteady solver is used to solve the governing equations of momentum, mass and energy conservation (eqs. 3.9–3.30) and the turbulence kinetic energy equation sequentially in the 3-D model. The turbulent flow is modeled with the standard k-ω SST model. In the 2-D model, segregated, implicit unsteady and laminar are used for simulation which is provided in Table 6.2. One of the added benefits of using a 2-D model is that due to time-averaged boundary conditions and absence of the liquid film, larger timestep sizes could be chosen compared with the 3-D model.

Table 6.2 Parameters used in 2-D simulation

Mesh size	Model	Flow & energy model	Solver type	Velocity under-relaxation factor	Pressure under-relaxation factor
52,300	**Laminar**	**Segregated**	**Implicit unsteady, second order**	**0.8**	**0.3**

6.3.3 Boundary Conditions

In order to accurately assess and understand drop size data, all of the key variables such as nozzle type, pressure, capacity, liquid properties and spray angle have to be taken into consideration.

The measurement techniques, type of drop size analyzer and data analysis and reporting methods all have a strong influence on the results. The drop size testing method should also be fully understood. To name a few, one could use a direct examination of photographic/video recordings of the spray such as optical imaging analyzers or optical techniques based on laser scattering and laser interferometry such as Phase Doppler Particle Analyzers (PDPA).

The calculated droplet Sauter mean diameter (SMD) and droplet velocity were estimated using the correlation (Eqs. 6.1 and 6.2) of Estes and Mudawar (1996) with a mean absolute error of 12.4% and that of Ghodbane and Holman (1991) developed from simple energy balance considerations around the nozzle, respectively,

$$\frac{d_{32}}{d_0} = 3.07[\frac{\rho_g^{1/2}\nabla P d_0^{3/2}}{\sigma^{1/2}\mu}]^{-0.259} \quad (6.1)$$

$$v = (\frac{2\nabla P}{\rho})^{1/2} \quad (6.2)$$

As in reality, the spray is injected into the liquid layer at an angle θ (theta), so the spray mass will be a function of the injecting angle.

6.3.4 Computational Details

The 3-D mesh should be able to resolve the velocity, temperature and pressure gradients in the boundary layer, induced by the cooling, impingement and fluid film evolution. A finite volume segregated solver with second order unsteady implicit formulation has been employed throughout (STAR-CCM+ User's Manual, 2012). The computational domain and a coarsened grid are shown in Fig. 6.2.

Some of the calculated operating parameters of the nozzle used in the present study, from Spraying System Broacher (2012), are provided in Table 6.3.

Table 6.3 Heinz's nozzle performance data

Nozzle type	Nozzle orifice dia. (inch)	Max. free passage of orifice dia. (inch)	Nozzle angle	Operating pressure (kg/cm^2)	Flow rate (kg/s)	Droplet velocity (m/s)	SMD (μm)
¾m HH50SQFullJet®	0.266	0.172	75º	1.41	0.41	5.3	312

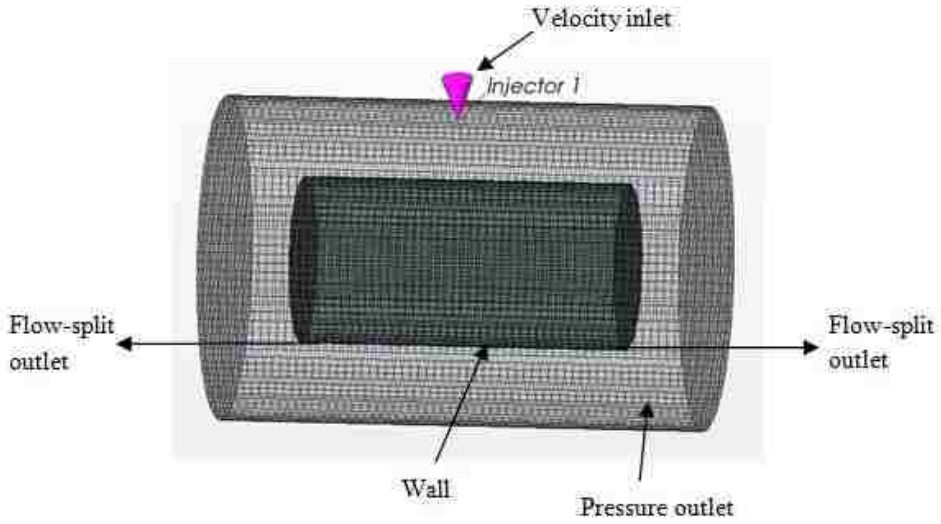

Figure 6.2 Generated (coarsened) mesh and the boundary conditions presented in 3-D model

Based on the information provided by Heinz and field measurement data, conveyor speed and tomato juice can rpm were calculated (Table 6.4). The information was fed into the simulation as boundary conditions. In Fig. 6.3, ω is the rotation rate and *R* is radius of the can and tangential velocity is calculated based on these two parameters.

Table 6.4 Operating parameters for the numerical model

Length of conveyor (m)	Conveyor's Speed (m/s)	Height of nozzle (m)	Tomato juice can rpm
35.35	0.118	0.43	23

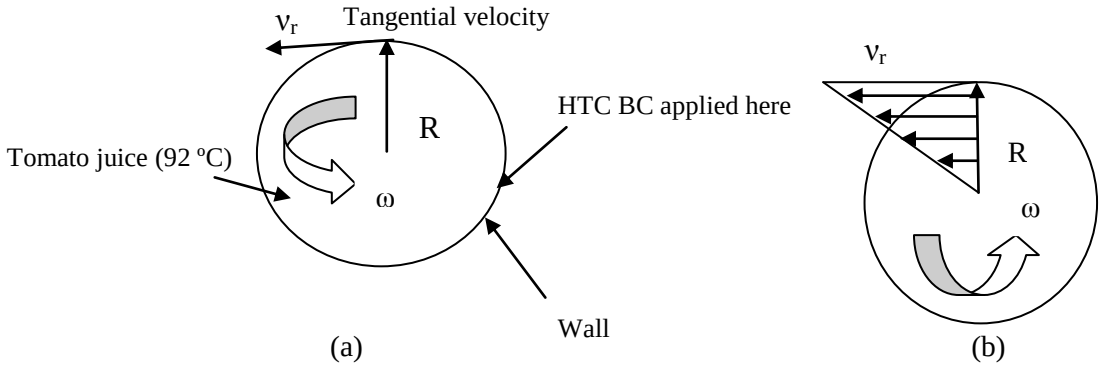

Figure 6.3 A 2-D model boundary conditions used for CFD simulation: (a) parameters and boundaries (b) simplified velocity distribution

6.4 Numerical Approach

STAR-CCM+ is used for the present simulations. In the 3-D simulation, the can is assumed to be stationary and the cone spray nozzle impinges water droplets onto the hot can. In this study, and for the purpose of comparison, the computations are performed for a can similar to that used in Heinz under similar operating conditions.

In the 2-D model, the can's wall plays an important role in the heat transfer rate, hence the wall conductivity and thickness are considered during the simulation. In order to accurately account for the boundary layer, the mesh should be optimized with a fine mesh near boundaries. If the boundary layer is not resolved adequately, the underlying physics of the flow will not be captured correctly and the simulation results will not be reliable. The main objective of 3-D simulation is to estimate the heat transfer coefficient of the liquid film on the hot can surface, which will be subsequently applied to the 2-D model wall.

Figure 6.4 shows the meshes used in the simulations. The fluid domain is divided into around 1,400,000 cells graded with a finer grid near the wall. The computations are performed for a can with a radius of 0.05 m and a length of 0.17 m, with the can assumed to contain hot water at 92º C. Conjugate heat transfer is used to account for the heat transfer from the hot liquid inside the can to the fluid on the outside.

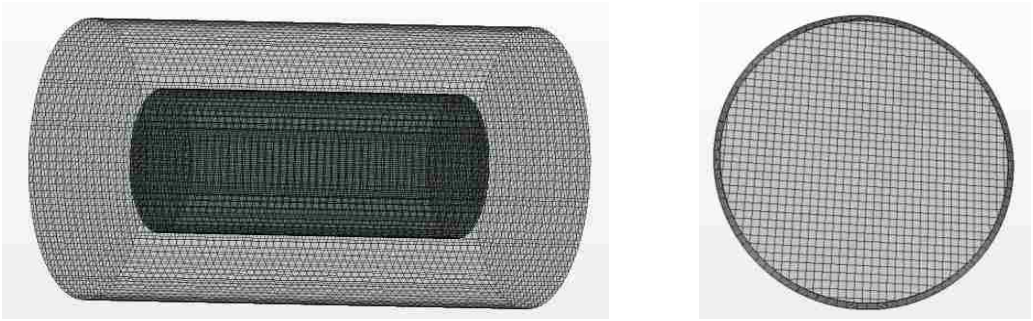

(a) (b)

Figure 6.4 Generated mesh for the 3-D and 2-D models (a) 3-D mesh (b) 2-D mesh (for demonstration purposes, the coarsened meshes are shown here)

6.5 Results and Discussion

In this work, the cooling process of a horizontal can filled with tomato juice, rotating axially at two different rpm's (25 and 50) and cooled by impinging water droplets at temperature of 28ºC is investigated. The results of the simulation are compared with the data collected from the Heinz plant. The simulation for 2-D model was run for the about 300 seconds.

6.5.1 3-D Model Results

In order to reduce the 3-D data of HTC on the outside of the can, we need to spatially average the data to obtain a 2-D distribution. If the can was not rotating, then we could apply the HTC at different circumferential locations on the can outside surface. However, since the can rotates, any point on the can experiences both the maximum and minimum HTC values. Acquiring this range would be impractical and perhaps unnecessary for the present application. Since the temperature distribution in the can at the end of the line (after a significant length of time) it is reasonable to apply a constant HTC to the can surface. This is consistent with the fact that the cooling down period (up to 300 seconds) is very long in comparison with the simulation time scales and therefore it would not be feasible to perform the 3-D HTC calculation for more than a few seconds of physical time. To obtain the long-term HTC to apply as a boundary condition for the 2-D simulation, the time-averaged value for the first four seconds of a 3-D run was calculated. This value was approximately 24,600 W/m^2K and will be used as the HTC boundary condition applied to the outside surface of the can.

6.5.2 Effect of rpm on Tomato Juice Temperature Distribution

The moving can is rotated in order to enhance mixing inside the food container by agitation, which in turn, increases the rate of heat transfer to the thermal centre.

The simulation was run for 300 seconds, which is the same amount of time that the medium size can travels from the first nozzle to the exit. The residual graphs for the initial stages of the 2-D simulation are shown in Fig. 6.5. The stationary can and rotating can are both included in the figures.

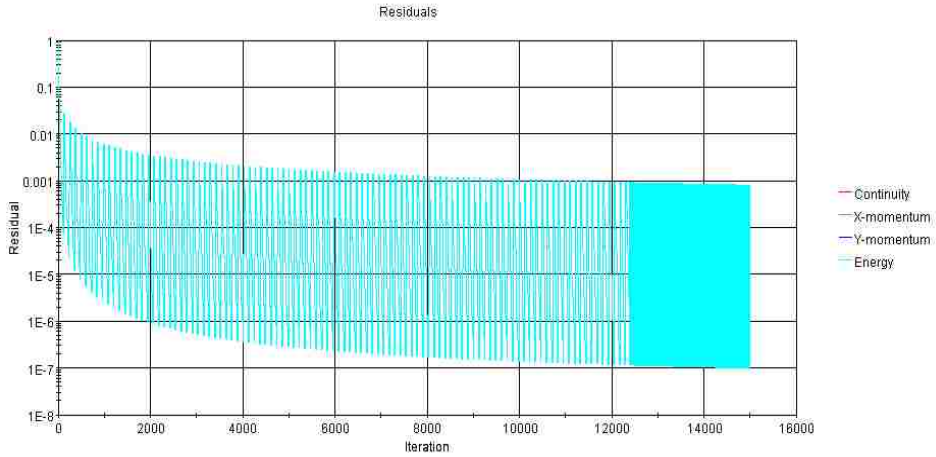

(a)

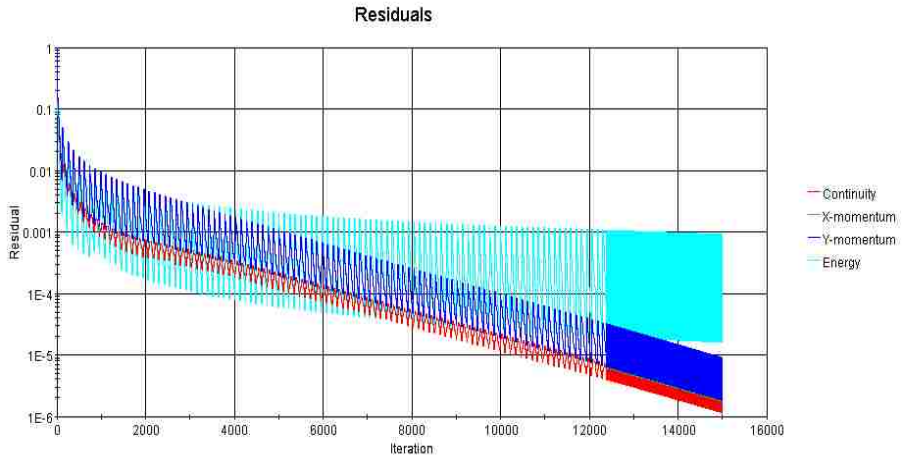

(b)

Figure 6.5 Typical residual levels at the initial stages of the 2-D simulation for (a) stationary can (b) rotating can at 25 rpm

The results of the simulation show that the rotation of a can has a significant effect on the size and location of the SCZ. Figure 6.6 shows the velocity for two different rpm, 25 rpm and 50 rpm. The velocity in the centre of the can is the slowest which is due to less agitation and mixing in this region. Gravitational force is much stronger than centrifugal force in this area. As a result, natural convection is more dominant than forced convection. Also, the formation of a high velocity region located near the wall of the can due to centrifugal force has a significant impact on increasing forced convection. The thermal boundary layer is being agitated and mixed due to rotation, resulting in higher heat transfer.

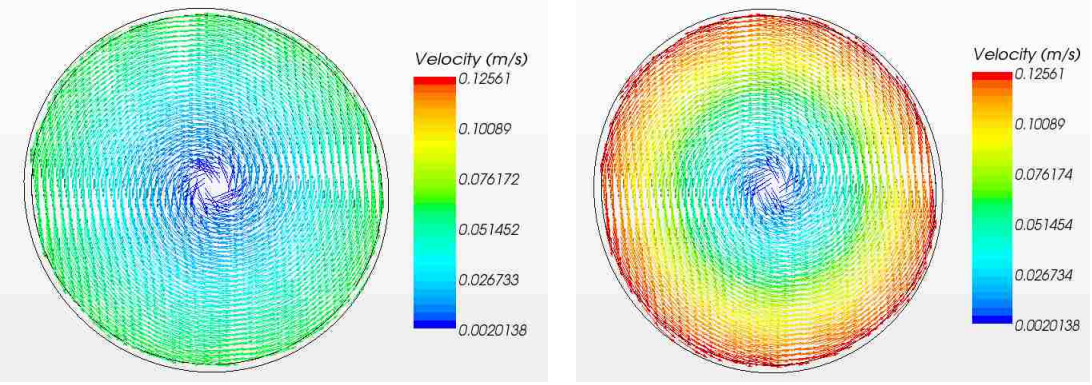

(a) (b)

Figure 6.6 Variation of velocity vectors with time presented at (a) 25 rpm (b) 50 rpm

Fig. 6.7 indicates that the SCZ volume is reduced significantly due to the dominating effect of rotation when compared to the effect of natural convection in a stationary can. By comparison between the 0, 25 and 50 rpm and their thermal profile, it is clear the that SCZ volume drops significantly between 0 and 25, but the impact of the rotation rate between 25 and 50 rpm is not as profound. Fig. 6.7 also illustrates the combined effect of natural convection and forced convection due to can rotation. The evolution of the temperature with time for both rotated and stationary cans are shown in Fig. 6.8.

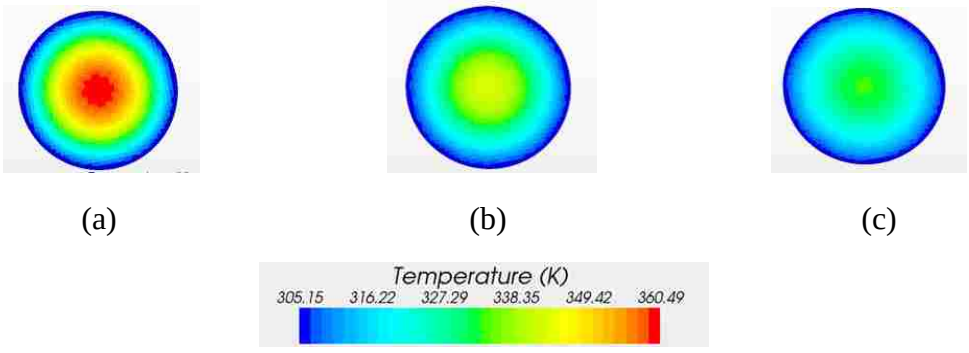

(a) (b) (c)

Figure 6.7 Temperature contour for (a) stationary can or 0 rpm (b) 25 rpm (c) 50 rpm after 300 seconds of actual cooling time

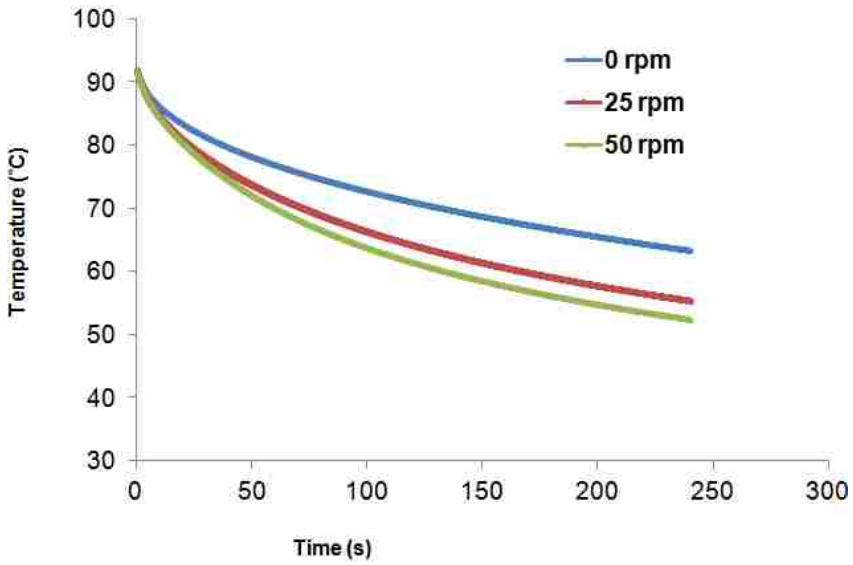

Figure 6.8 Variation of temperature versus time for different rpm

Figure 6.9 shows the variation of temperature versus radial distance for both rotating and stationary cans at 300 seconds. As shown, the temperature decreases along the radial direction outward from the centre to edge. Based on the results provided above, the mean temperature of the tomato juice in the radial direction confirms that the heat transfer rate is higher close to the wall. As it gets closer to the centre, the temperature tends to increase. The temperature difference between 0 and 25 rpm is very noticeable. Again, the gap between the 25 and 50 rpm is not as wide as that of 0 to 25 rpm but is still significant.

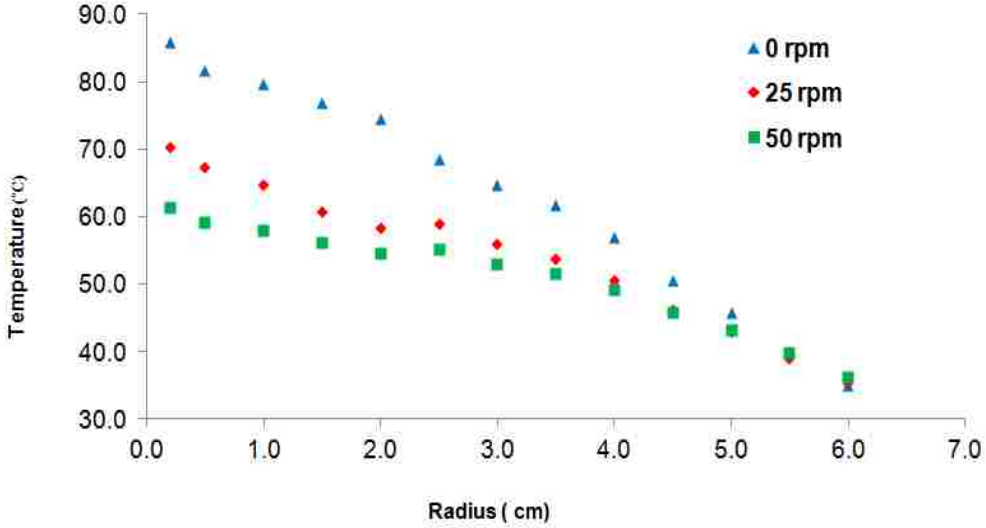

Figure 6.9 Temperature variations versus the can radius for different rpm after 300 seconds

At Heinz, the average rpm for the medium size can is about 23. Figure 6.11 shows the volume-averaged temperature data for the medium size can obtained from the simulation. In the iButton measurements, the iButton moves as the can spins and it is quite possible that the iButton sensor mostly sits on the inner surface of the can, considering the rpm value. The recorded data basically shows the temperature of the tomato juice close to the wall of the can.

The temperature values calculated using Newton's Cooling Law (NCL) (based on the data that was gathered by the thermometer) are also included in Fig. 6.10. The temperature values measured at two different locations of the conveyor (inner and outer) are presented in Fig. 6.10 as well. Overall, the data is in a reasonable agreement with experimental results considering the assumptions in the flow simulations as well as the industrial nature of the environment where controlled tests are impossible to perform. As a result, complete and detailed comparison of the CFD results with the actual data of the plant, beyond the current level, is not reasonable.

To examine the local cooling features inside the can, the local temperature values are plotted in Fig. 6.11, showing the significance of the temperature probe location. Due to the fact the iButton is possibly close to or on the walls of the can, it would probably be more reasonable to assume that the calculated temperature values close to the wall provide a better representation of the iButton condition. In depth and very detailed simulation of the local effect of temperature in a full 3-D can, and with rolling and translation, are beyond the scope of the current work.

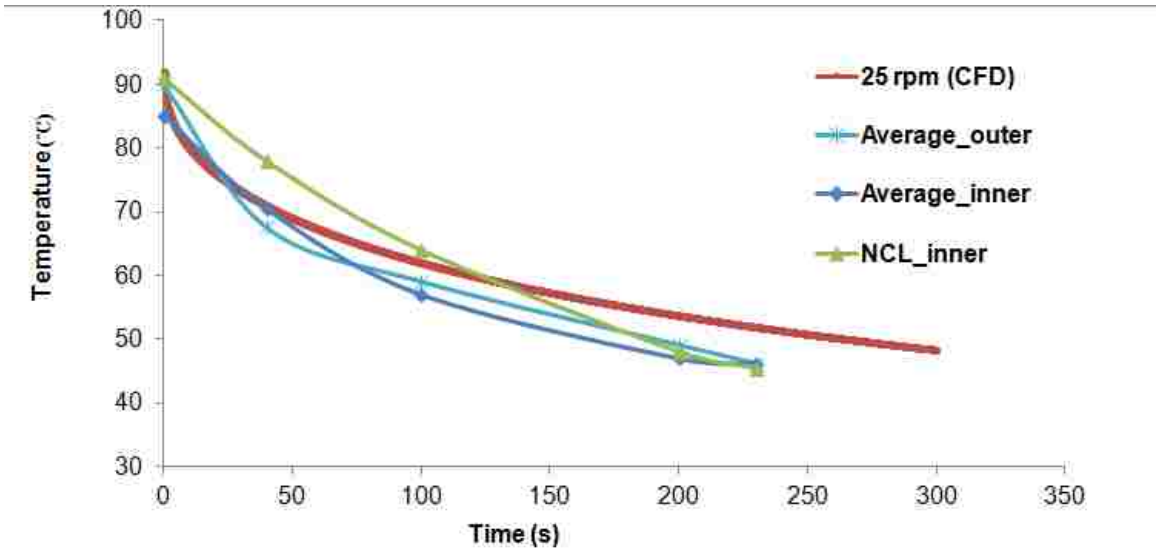

Figure 6.10 Simulated volume-averaged temperature variation at 25 rpm compared with the NCL model and measurements at the plant with different conveyor locations

6.6 Closure

In this chapter, the CFD approach to simulate film formation outside the container and cooling inside it were presented. It uses a combination of 2-D and 3-D models, where the 3-D heat transfer coefficient values are averaged and applied to a 2-D slice of the can which contains the hot fluid inside. Long-term cooling simulation results for the 2-D model show the significant impact of the rotation rate on the heat transfer rate in the inner fluid. Density and viscosity were considered constant during the cooling process. The size of the Slowest Cooling Zone (SCZ) of a can was reduced noticeably by increasing velocity and enhancement of the mixing due to increase in rotational speed of the cans. However, there is an optimum rpm value to achieve maximum temperature drop and the most efficient heat transfer. Furthermore, achieving very high values of rpm on the spray cooling line might not be easy to implement.

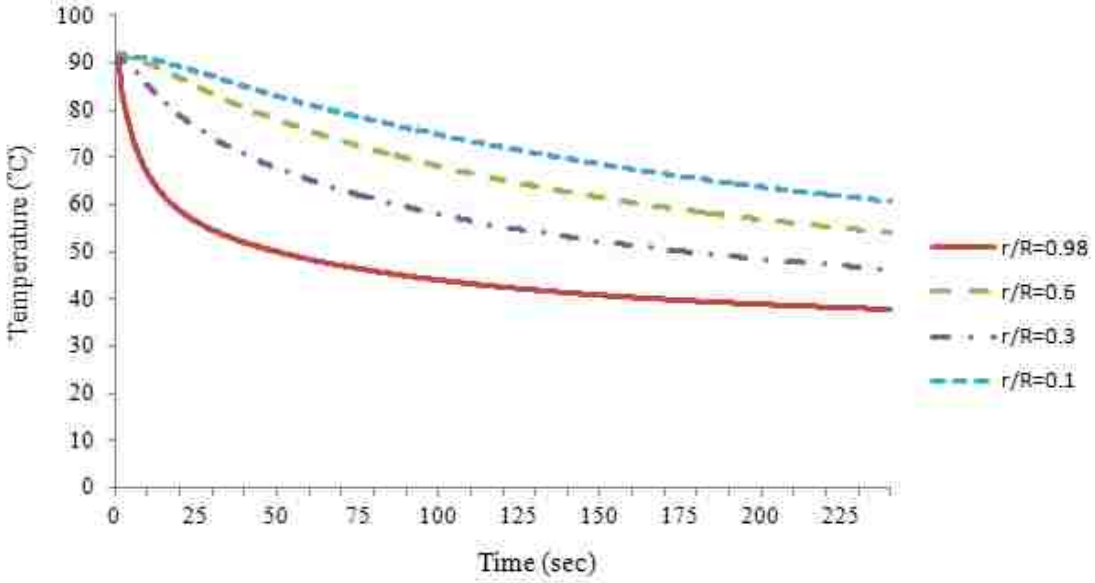

Figure 6.12 Variation of temperature with time for different locations inside the rotating can (25 rpm)

Chapter 7. Conclusions and Recommendations

7.1 Conclusions

In this work, computational fluid dynamics (CFD) simulations were carried out to develop a better understanding of the fluid flow and heat transfer associated with the spray impact onto a hot solid surface. Numerous small droplets of cold liquid, which are present in the spray, discharge into a large volume of air and in most cases, upon hitting the hot surface, form a very thin liquid layer on the solid surface. An Eulerian-Lagrangian approach was implemented in commercial code in STAR-CCM+ to tackle this multiphase and multi-scale problem.

Another complexity is added to this problem in the case where the solid surface encloses a volume containing another (hot) liquid inside which acts as the heat source for the whole system. In this case, the solid container is heated due to the hot liquid inside it and a cold liquid is sprayed on the outside surfaces of the hot container to cool both the container and the hot fluid inside. The goal of this research was to create a computational model which can predict the time-averaged heat transfer coefficient on the hot surface covered with fluid film and to predict the time variation of bulk temperature for the liquid inside the container. The Conjugate Heat Transfer approach was used to achieve this goal. The task of combining the individual complex phenomena mentioned above together to successfully model the spray cooling is a great challenge. However, it is believed that the methodology developed in this study has managed to strike an acceptable balance between prediction accuracy and computational efficiency.

To gain confidence in the numerical methodology, it is important to validate the results with relevant experimental results. To test the model validity for the non-boiling spray cooling regime, some case studies were selected from Karwa et al. (2007) and the simulations results were compared with the experimental data. A wide range of parameters such as droplet sizes, velocities and mass fluxes are simulated and compared with the experiments. The CFD results are found to be in good agreement with the experiments and tend to follow the trends observed in the experiments when operating conditions and parameters are changed. This model has the ability to maximize heat

transfer rate by optimizing a nozzle-hot plate distance, mass flow rate and specific nozzle parameters such as average droplet velocity and spray angle. It was found from the numerical simulations that the heat transfer rate is improved by increasing the spray droplet velocity due to an increase in momentum which in turn produces more agitation to the fluid film on the hot surface and affects the thermal boundary layer. Also, increasing the mass flux (by increasing the number of droplets) produces more momentum, more agitation to the liquid film and a thinner thermal boundary layer which eventually enhances the heat transfer rate.

The next step was to introduce a model that could mimic the actual industrial setting, i.e., the spray cooling system at Heinz Canada. Cold water spray cooling is used to cool down cans containing hot tomato juice. The cans roll on a moving conveyor system, which enhances heat transfer inside them. Several spray nozzles are installed along the cans' path where every can gets exposed to each spray nozzle as it moves on the conveyor.

The biggest challenge encountered in this research was to reasonably predict the effect of rate of rotation, measured in revolutions per minutes (rpm), on the temperature distribution inside the tomato juice can while it moves along a conveyor. In the actual industrial spray cooler, it might takes up to several minutes to cool down the cans. With the mesh size and numerical time-steps required for capturing this thermal-fluidic phenomenon, it is nearly impossible to solve over the full duration of cooling in a 3-D simulation. In addition, generating and manipulating a 3-D translating and rotating mesh and introducing new nozzles into the computational domain as the can rolls and moves proved to be very complex and computationally expensive. Thus, the problem was broken into two simpler stages, resolving some of the issues in 3-D, the results of which are fed into a 2-D model. The 3-D modeling was employed for prediction of an averaged heat transfer coefficient (HTC) distribution on the can surface taking into account the spray impact and film formation. Using the averaged HTC values and by mapping them into a 2-D domain, it was then possible to predict the cool-down trend inside the can for a representative circular slice of the can and the juice inside it. The 2-D flow of juice inside the can was modeled based on the assumption of rotating boundary conditions to mimic

the rolling motion of cans. It was also assumed that there was no air inside the can and there was only one phase (liquid juice) inside.

The results show that by increasing the rpm for a tomato juice can up to a certain critical value, the can cools down faster and the Slowest Cooling Zone (SCZ) volume is reduced. The temperature near the inner walls of the can is cooler due to their higher velocity close to the rotating wall, as well as the fact that the wall acts as a heat sink because it is touched by the cold liquid film on the outside.

7.2 Recommendations for Future Work

A combination of three- and two-dimensional models were used in this study for calculating the heat transfer coefficient and temperature distribution inside a hot tomato juice can while it rotates and moves between the spray nozzles. In the 2-D simulation, the flow inside the can was studied under the assumption that no air existed inside the can. In reality, this is a rotating two-phase fluid system inside a horizontal can mostly consisting of liquid content (tomato juice) and some small headspace (occupied by air). During the current simulations, the headspace was not taken into account.

In order to gain more information on the parameters that affect spray cooling performance and its heat transfer rate, the following recommendations for future work are suggested:

i) Headspace might play an important role in agitation in conjunction with the effect of rotation speed. To tackle this problem, a computational method capable of tackling liquid-gas interfacial flows such Volume of Fluid (VOF) method needs to be considered. The VOF method is known for its very small time step size requirements. Therefore, introducing the VOF method will probably increase the computation time significantly.

ii) The physical properties of the liquid (viscosity and density) were assumed to be constant (based on an average fluid temperature). The effect of temperature-dependent physical properties on the heat transfer is worth considering. Along the same line, it might be more accurate to model the juice as a non-Newtonian liquid.

iii) In regards to improving the modeling accuracy, the most obvious way would be to represent all the flow effects and operating conditions as close as possible. This requires developing a 3-D moving and rotating mesh model. However, this will require access to significant High Performance Computing facilities.

iv) In order to perform meaningful comparison between the CFD and experimental results, a detailed experimental investigation geared towards this application is required. Almost all the experimental studies available in the literature describe the spray cooling for a flat or curved surface with no fluid inside. It would be valuable to measure the temperature distribution at different locations inside the cans. Considering that the industrial setting for the current study lacked the controllability of an experimental lab, it would be insightful to investigate the spray cooling performance for a single can under stationary conditions to provide a more comprehensive set of data for the effect of spray parameters on the cooling behaviour.

References

Bai, C., Gosman, A., "Development of methodology for spray impingement simulation", SAE Technical Paper Series 950283, 1995.

Bai, C., Rusche, H., Gosman, A., "Modeling of gasoline spray impingement", Atomization and Sprays, Vol. 12, pp. 1-27, 2002.

Bonacina, C., Del Giudice, S., Comini, G., "Dropwise evaporation", ASME Journal of Heat Transfer, Vol. 101, pp. 441-446, 1979.

Bostanci, H., "High heat flux spray cooling with ammonia on enhanced surfaces", PhD Thesis, Dept. of Mechanical Engineering, University of Central Florida, 2010.

Bonacina, C., Comini, G., Del Giudice, S., "Evaporation of atomized liquids on hot surfaces", Letters in Heat and Mass Transfer, Vol. 2(5), pp. 401-406, 1975.

Chen, R-H., Chow, L.C., Navedo, J.E., "Effects of spray characteristics on critical heat flux in subcooled water spray cooling", Int. J. Heat and Mass Transfer, Vol. 45, pp. 4033–4043, 2002.

Cheng, W., Liu, Q., Zhao, R., Fan, H., "Experimental investigation of parameters effect on heat transfer of spray cooling", Journal of Heat Mass Transfer, Vol. 46, pp. 911–921, 2010.

Chow, L.C., Sehmbey, M.S., Paris, M.R., "High heat flux spray cooling", Annu. Rev. Heat Transfer, Vol. 8, pp. 291–318, 1997.

Churchill, S.W., Chu, H.H.S., "Correlating equations for laminar and turbulent free convection from a vertical plate", Int. J. Heat Mass Transfer, Vol. 18, pp. 1323-1329, 1975.

Cole, V., Mehra, D., Lowry, S., Gray, D., "A numerical spray impingement model coupled with a free surface film model", Proceedings of the 16th Annual Thermal and Fluids Analysis Workshop, Orlando, FL, 2005.

Coles, R., McDowell, D., Kirwan, M.J., "Food Packaging Technology", CRC Press, 2003.

Coursey, J.S., "Enhancement of spray cooling heat transfer using extended surfaces and nanofluids", Ph.D. Thesis, Department of Mechanical Engineering, University of Maryland, 2007.

Deb, S., Yao, S.C., "Analysis on film boiling heat transfer of impacting sprays", Int. J. Heat and Mass Transfer, Vol. 32, pp. 2099–2112, 1989.

Dirita, C., De Bonis, M., Ruocco, G., "Analysis of food cooling by jet impingement, including inherent conduction", J. Food Engineering, Vol. 81, pp. 12-20, 2007.

Estes, K. A., Mudawar, I., "Correlation of Sauter mean diameter and critical heat flux for spray cooling", Int. J. Heat Mass Transfer, Vol. 38, pp. 2985–2996, 1995.

Estes, K. A., Mudawar, I., "Comparison of two-phase electronic cooling using free jets and sprays", Transactions of the ASME, J. Electronic Packaging, Vol. 117, pp. 323-332, 1995.

Freund, S., Pautsch, A.G., Shedd, T.A., Kabelac, S. "Local heat transfer coefficients in spray cooling systems measured with temperature oscillation IR thermography", Int. J. Heat Mass Transfer, Vol. 50, pp. 1953–1962, 2007.

Ghani, A.G.A., Farid, M.M., Zarrouk, S.J., "The effect of can rotation on sterilization of liquid food using computational fluid dynamics", J. Food Engineering, Vol. 57(1), pp. 9-16, 2003.

Ghodbane, M., Holman, J.P., "Experimental study of spray cooling with Freon-113", Int. J. Heat Mass Transfer, Vol. 34, pp. 1163–1174, 1991.

Gray, D., Kreitzer, P., Kuhlman, J., "Progress in modeling of spray cooling", 24th European Conference on Liquid Atomization and Spray Systems (ILASS–Europe), 2011.

Guéchi, M., Desevaux, P., Baucour, P., "Etude numérique du refroidissement d'une surface métallique par pulverization", (spray cooling), 20ème Congrès Français de Mécanique, Besançon, 2011.

Guéchi, M., Desevaux, P. Baucour, P. "Numerical and experimental study of spray cooling of a heated metal surface", 12th Triennial International Conference on Liquid Atomization and Spray Systems (ICLASS), Heidelberg, Germany, September 2-6, 2012.

Hsieh, S-S., Fan, T-C., Tsai, H-H., "Spray cooling characteristics of water and R-134a., Part I, nucleate boiling", Int. J. Heat Mass Transfer, Vol. 47, pp. 5703-5712, 2004.

Kalantari, D., "Characterization of liquid spray impact onto walls and films", PhD Thesis, Technischen Universitat Darmstadt, Darmstadt, Germany, 2006.

Karwa, N., Kale, S.R., Subbarao, P.M.V., "Experimental study of non-boiling heat transfer from a horizontal surface by water sprays", Experimental Thermal and Fluid Science, Vol. 32, pp. 571–579, 2007.

Kim, J., “Spray cooling heat transfer: the state of the art”, Int. J. Heat and Fluid Flow, Volume 28(4), pp. 753-767, 2007.

Kim, Y.C., Nishio, S., Ohkubo, H., “Heat transfer in a high temperature region of spray cooling interacting with liquid film flow”, Heat Transfer, Japanese Research, Vol. 26 (4), 1997.

Kyriopoulos, O.N.,“Gravity effect on liquid film hydrodynamics and spray cooling”, PhD Dissertation, Technischen Universitat Darmstadt, Darmstadt, Germany, 2010.

Lin, L., Ponnappan, R., “Heat transfer characteristics of spray cooling in a closed loop”, Int. J. Heat Mass Transfer, Vol. 46, pp. 3737–3746, 2003.

Lin, L., Ponnappan, R., Yerkes, K., Hager, B., “Large area spray cooling”, Proceedings of 42nd AIAA Aerospace Sciences Meeting and Exhibit, Reno, NV, 2004.

Meredith, K., Xin, Y., de Vries, J., “A numerical model for simulation of thin-film water transport over solid fuel surfaces”, Fire Safety Science, Vol. 10, pp. 415-428, 2011.

Monde, M., “Critical heat flux in saturated forced convection boiling with an impinging droplet”, Trans. JSME, Vol. 46, pp. 1146–1155, 1980.

Moreira, A.L.N., Moita, A.S., Panao, M.R., “Advances and challenges in explaining fuel spray impingement, How much of single droplet impact research is useful?”, Prog. Energy Comb. Sci., Vol. 36, pp. 554–580, 2010.

Mudawar, I., Valentine, W.S., “Determination of the local quench curve for spray cooled metallic surfaces”, J. Heat Treating, Vol. 7, pp. 107–121, 1989.

Mudawar, I. and Estes, K.A., “Optimizing and predicting CHF in spray Cooling of a square Surface”, J. Heat Transfer, Vol. 118, no. 3, pp. 672–679, 1996.

Mudawar, I.,“Assessment of high-heat-flux thermal management schemes”, International Conference on Thermal Phenomena (Itherm), Las Vegas, NV, 2000.

Mudawar, I., “Assessment of high heat-flux thermal management schemes”, IEEE Trans. Compon. Packag. Technol., Vol. 24, pp. 122–141, 2001.

Oliphant, K., Webb, B.W., McQuay, M.Q., “An experimental comparison of liquid jet array and spray impingement cooling in the non-boiling regime”, Experimental Thermal and Fluid Science, Vol. 18, pp. 1-10, 1998.

Pais, M.R., Chow, L.C., Mahefkey, E.T., “Surface roughness and its effect on the heat transfer mechanism in spray cooling”, J. Heat Transfer, Vol. 114, pp. 211–219, 1992.

Pautsch, A.G., “Heat transfer and film thickness characteristics of spray cooling with phase change”, Master’s Thesis, Dept. of Mechanical Engineering, University of Wisconsin-Madison, 2004.

Pautsch, G., “Thermal challenges in next generation of supercomputers”, CoolCon, 2005.

Pautsch, A.G., Shedd, T.A., “Spray impingement cooling with single- and multiple-nozzle arrays, Part I: Heat transfer data using FC-72”, Int. J. Heat Mass Transfer, Vol. 48, 3167-3175, 2005.

Pautsch, A.G., Shedd, T.A., “Adiabatic and diabatic measurements of the liquid film thickness during spray cooling with FC-72”, Int. J. Heat Mass Transfer, Vol. 49, pp. 2610–2618, 2006.

Peterson, C.O., “An experimental study of the dynamic behaviour and heat transfer characteristic of water impinging upon a heated surface”, Int. J. Heat Mass Transfer, Vol. 13, pp. 369-381, 1970.

Rini, D.P., Chen, R.H., Chow, L.C., “Bubble behaviour and nucleate boiling heat transfer in saturated FC-72 spray cooling”, J. Heat Transfer, Vol. 124, pp. 63–72, 2002.

Roisman, I.V., Tropea, C., “Fluctuating flow in a liquid layer and secondary spray created by an impacting spray”, Int. J. Multiphase Flow, Vol. 31(2), pp. 179-200, 2005.

Rosin, P., Rammler, E., "The laws governing the fineness of powdered coal", Journal of the Institute of Fuel, Vol. 7, pp. 29–36, 1933.

Rybicki, J. R., Mudawar, I., “Single-phase and two-phase cooling characteristics of upward-facing and downward-facing sprays”, Int. J. Heat Mass Transfer, Vol. 49, pp. 5–16, 2006.

Satoh, K., Kawai, T., Ishikawa, M., and Matsuoka, T., “Development of Method for Predicting Efficiency of Oil Mist Separators”, SAE Technical Paper 2000-01-1234, 2000.

Sehmbey, M. S., Chow, L. C., Hahn, O. J., M. R. Pais, “Spray cooling of power electronics at cryogenic temperatures”, AIAA Journal of Thermophysics Heat Transfer, Vol. 9, pp. 123-128, 1995.

Selvam, R. P., Lin, L. Ponnappan, R., “Computational modeling of spray cooling: current status and future challenge”, CP746, Space Technology and Applications International Forum (STAIF), Albuquerque, NM, 2005.

Selvam, R.P., Sarkar, M., Ponnappan, R., "Modeling of spray cooling, effect of droplet velocity and liquid to vapour density ratio on heat transfer", J. Heat Transfer, Vol. 131, 2009.

Stanton, D.W., Rutland, C.J., "Multi-dimensional modeling of heat and mass transfer of fuel films resulting from impinging sprays", SAE Paper No. 980132, 1998.

Stanton, D.W., Rutland, C.J., "Multidimensional modeling of thin liquid films and spray-wall interactions resulting from impinging sprays", Int. J. Heat and Mass Transfer, Vol. 41, pp. 3037-3054, 1998.

Stanton, D.W., Rutland, C.J., "Modeling fuel film formation and wall interaction in diesel engine", SAE Paper No. 960628, 1996.

STAR-CCM+ User's Manual, Version 7.06, CD-adapco, 2012.

Toda, S., "A study of mist cooling, 1st report: investigation of mist cooling", Heat Transfer, Japanese Research, Vol. 1, pp. 39–50, 1972.

Tucker, G. S. and Cfdra, P. C., "Modelling the cooling phase of heat sterilization processes, using heat transfer coefficients", Int. J. Food Science and Technology, 1990, 25, 668-681.

Tropea, C., Roisman, I., "Wasserströmung bei Hochdruckreinigern von der Düse bis zum Objekt", Kärcher Technologie- und Innovationsforum, Winnenden, Germany, 2007.

Wang, Y., Liu, M., Liu, D., Xu, K., "Heat flux correlation for spray cooling in the nonboiling regime", Heat Transfer Engineering, Vol. 32(11), pp.1075–1081, 2011.

Website, www.lps.umd.edu, Laboratory for Physical Sciences, University of Maryland.

Website, www.meecc.com

Website, www.pitek.us

Website, www.valcompanies.com, VAL-CO USA & Canada

Wilcox, D.C., *Turbulence Modeling for CFD*, 3rd Edition, DCW Industries, 2006.

Yang, J., Chow, L.C., Pais, M.R., "Nucleate boiling heat transfer in spray cooling", J. Heat Transfer, Vol. 118 , pp. 668– 671, 1996.

Yang, J., Chow, L.C., Pais, M.R., and Ito, A., "Liquid film thickness and topography determination using Fresnel diffraction and holography", Experimental Heat Transfer, Vol. 5-4, pp. 239–252, 1992.

Youssef, M.R., “Modeling the effect of a spray on a liquid film on a heated surface”, PhD Thesis, Dept. of Civile and Environmental Engineer, West Virginia University, 2007.

Zhao, R., Cheng, W., Liu, Q., Fan, H., “Study on heat transfer performance of spray cooling, model and analysis”, Heat Mass Transfer, Vol. 46, pp. 821–829, 2010.

Vita Auctoris

NAME	Masoumeh Jafari
PLACE OF BIRTH	Ramsar,Iran
EDUCATION	Ferdowsi University, Iran
	1996-2001 B.A.Sc